MULTI-LEVEL SIMULATION AND MODELING OF VERTICAL BRIDGMAN GROWTH OF SINGLE CRYSTALS AND SOLIDIFICATION OF BINARY ALLOYS

By

HONG OUYANG

A DISSERTATION PRESENTED TO THE GRADUATE SCHOOL
OF THE UNIVERSITY OF FLORIDA IN PARTIAL FULFILLMENT
OF THE REQUIREMENTS FOR THE DEGREE OF
DOCTOR OF PHILOSOPHY

UNIVERSITY OF FLORIDA

1996

ACKNOWLEDGEMENTS

I can barely express my heartfelt gratitude towards my advisor, Professor Wei Shyy, for the help that he has provided in more ways than he will ever know. His intelligent guidance and enthusiastic encouragement have always been inspirational to me both professionally and personally. His pure concern to students in general and deep understanding to international students in particular have been sources of solutions to me during times of frustration. I sincerely thank him for introducing me to the research field which I have found most enjoyable today, and thank him for the financial support that he has provided during my graduate studies.

I owe a special debt of gratitude to Dr. Chen–Chi Hsu which can never be repaid. I will never forget his providing me the opportunity to study in the U.S. and giving me freedom to pursue my own research interest. I would also like to thank the members of my committee, Dr. Ulrich Kurzweg, Dr. Renwei Mei, Dr. John Abbitt for their guidance and help during the course of my graduate study, especially Dr. Kurzweg for allowing me to knock frequently on his office door. I have also been fortunate to be "spoiled" in a warm and friendly research group. For their gracious tolerance of my ignorance and patient help, I thank my colleagues Dr. Jeff Wright, Dr. H. S. "Uday" Udaykumar, Dr. Rick Smith, Dr. Siddarth "ST" Thakur, Dr. Madhukar "Maddy" Rao, Dr. Jian "James" Liu, Andrew Martin, Venkat "Venky" Krishnamurthy, Lihong Li, Keith Clutter, Vivek Jayaraman and Ann Guthrie for the many memorable times they have shared with me. In particular, I express my sincere thanks to Maddy, Andrew and Uday for their critical and valuable opinions in my thesis work and willingness to share their knowledge and experience.

Special thanks to Professor Michael Kaufman and Dr. Vlady Levit from the Department of Materials Science and Engineering for the many pleasant discussions and collaborative work. Partial financial support from AFOSR, BDM International and the Department of Aerospace Engineering, Mechanics and Engineering Science at the University of Florida is gratefully acknowledged. Some of the computations carried out in this work were supported by a grant of

computer time from the research computing initiative, NERDC, University of Florida and were done on their IBM SP2 cluster.

I reserve my final gratitude to my husband, Feng, and my lovely son, Tom, who has grown up with my thesis work and is now fifteen months old. Without their love and support, I would never have amounted to anything. To them, I dedicate this thesis.

TABLE OF CONTENTS

page

ACKNOWLEDGEMENTS ii

TABLE OF CONTENTS iv

ABSTRACT vii

CHAPTERS

1. INTRODUCTION 1
   - 1.1 Solidification Phenomena 2
     - 1.1.1 Basic Concept 2
     - 1.1.2 Characteristics of Single Crystals and Alloys 3
   - 1.2 Modeling of Solidification Phenomena 4
     - 1.2.1 Modeling of Single Crystal Growth 4
     - 1.2.2 Modeling of Alloy Solidification 5
   - 1.3 The Current Contributions 6

2. GOVERNING EQUATIONS AND NUMERICAL METHODS FOR THE BRIDGMAN GROWTH PROCESS 9
   - 2.1 Physical Illustration 9
     - 2.1.1 Physical Complexities 9
     - 2.1.2 Geometrical Complexities 14
   - 2.2 Mathematical Formulations and Numerical Strategies 14
     - 2.2.1 The Formulation of Governing Equations 15
     - 2.2.2 Comments on the Special Treatment 16
     - 2.2.3 Numerical Method with Multi–Level Strategy 18
   - 2.3 Closure 19

3. MULTI–LEVEL SIMULATION OF VERTICAL BRIDGMAN GROWTH OF NiAl CRYSTAL 21
   - 3.1 Background 21
   - 3.2 Simulation and Measurement of NiAl System 25
     - 3.2.1 Two–Level Modeling Result 25
     - 3.2.2 Experimental Procedure 33

3.2.3 Comparison with Numerical Result 39
3.2.4 Detailed Analysis of Processing Conditions 46
3.3 Closure 51

4. MULTI–LEVEL SIMULATION OF VERTICAL BRIDGMAN GROWTH OF CdTe CRYSTAL 53

4.1 Background 53
4.2 Numerical Solutions of CdTe System 58
4.2.1 The Flat Base System 59
4.2.2 The Semi–Spherical Base System 63
4.3 Closure 65

5. FORMULATION OF MACROSCOPIC TRANSPORT EQUATIONS FOR ALLOY SOLIDIFICATION 69

5.1 Microscopic Transport Equations 69
5.2 Background of Macroscopic Transport Equations 71
5.2.1 Morphological Complexities and Disparate Scales 71
5.2.2 Definition of Averaging Volume 73
5.3 Volume Averaging Approach 75
5.3.1 Definitions and Theorems 77
5.3.2 The Derivation Procedure 79
5.3.3 The Treatment of Microscopic Deviation and Interfacial Terms . 81
5.4 Macroscopic Transport Equations via Volume Averaging Approach .. 86
5.4.1 Macroscopic Equation of Mass Conservation 86
5.4.2 Macroscopic Equation of Energy Conservation 87
5.4.3 Macroscopic Equation of Species Conservation 90
5.4.4 Macroscopic Equation of Momentum Conservation 92
5.4.5 Special Comment on the Formulation of Effective Coefficients . 93
5.4.6 Special Comment on Momentum Equation 95
5.4 Mixture Approach 97
5.5 Closure 98

6. NUMERICAL SIMULATION OF COLUMNAR SOLIDIFICATION OF BINARY ALLOYS 99

6.1 The Simplification of Transport Equations 99
6.2 Implementation of the Numerical Procedure 104
6.2.1 Solution Procedure 104
6.2.2 Implementation of Diffusion Model 105
6.3 Numerical Simulation of Solidification Process of NH_4Cl–H_2O Mixture 108
6.3.1 System Set–Up 108
6.3.2 Numerical Result and Comparison with Experimental Observations 111
6.4 Closure 114

7. CONCLUSIONS 116
6.1 Summary of the Current Work 116
6.2 Future Work 118
REFERENCES 120
BIOGRAPHICAL SKETCH 125

Abstract of Dissertation Presented to the Graduate School
of the University of Florida in Partial Fulfillment of the
Requirements for the Degree of Doctor of Philosophy

MULTI–LEVEL SIMULATION AND MODELING OF VERTICAL BRIDGMAN GROWTH OF SINGLE CRYSTALS AND SOLIDIFICATION OF BINARY ALLOYS

By

Hong Ouyang

May 1996

Chairperson : Dr. Wei Shyy
Major Department : Aerospace Engineering, Mechanics and Engineering Science

Modeling and computations of single crystal growth and alloy solidification have been studied. For single crystal growth, emphasis has been on the development of a comprehensive computational model that can deal with the many physical complexities presented in a vertical Bridgman growth system. These complexities include the coupled effects of conduction, convection, and radiation heat transfer, phase change dynamics, variable material properties, and geometry. To achieve computational accuracy and economy, a multi–level approach has been devised. At the global level, combined convection/conduction/radiation calculations with realistic geometrical and thermal boundary conditions are made inside the whole system. Refined calculations are then made to handle phase change dynamics within the ampoule region, with the boundary conditions supplied by the global simulations. Experimental measurements of the temperature distributions inside a vertical Bridgman system for growing the NiAl crystal have been conducted to validate the current model, with favorable agreement obtained. It has also been

found that the melt/solid interface temperature of NiAl is about 70 C higher than the melting temperature reported in the literature. Detailed analyses are then made to produce the possibilities of improving the thermal environment inside the furnace. To gain insight into the Bridgman growth process, numerical simulation of the CdTe crystal has also been conducted with different ampoule configurations. The effects of the ampoule geometry, variations in thermal conductivities between the melt and the crystal, and the thermal profile along the ampoule wall, on the interface characteristics have been addressed.

For alloy solidification, emphasis has been on the mathematical derivation of macroscopic transport equations of mass, momentum, heat and species from the microscopic continuum equations via a volume averaging approach. These unified equations can be applied to all regions of solid, liquid and mushy zones and can be coupled with the constructions of microscopic constitutive equations. In particular, a gradient transport model to represent microscopic deviation terms, arising during the volume averaging procedure, has been suggested. Numerical simulation of the solidification process of binary NH_4Cl–H_2O mixtures has been conducted to investigate phenomena such as sequential generation of convection cells and compositional stratification.

CHAPTER 1
INTRODUCTION

Solidification is a broad field encompassing a range of engineering and scientific disciplines including material science, thermal science, mechanics, mathematics, and transport phenomena. Despite the nature of the problem, transport phenomena in solidification process have not been adequately studied by researchers in the thermal sciences area due to the fact that most real solidification and material processes are extremely complex, not well defined and difficult to formulate mathematically. Because of the important role played by the fluid flow and heat and mass transfer phenomena during solidification, there is a definite need for thermo–fluid scientists to become more involved.

The present dissertation addresses issues arising from the modeling and simulation of fluid flow and heat/mass transfer process during solidification. The goal of this study is not only aimed at improving our understanding of the solidification process and developing new techniques, in both numerical methods and physical modeling, but to also help explore better ways of materials processing.

The difficulties of numerical modeling of the solidification process mainly arise from the multi–phase and multi–scale phenomena intrinsic to the problem, which are often coupled with other complexities such as variable material properties and multi–components. To account for these mechanisms, both numerical techniques and mathematical formulations have to be addressed in a systematic manner. Substantial progress has been made recently toward the mathematical–numerical modeling of the solidification processes (Shyy et al. 1996a, Brown 1988, Beckermann and Viskanta 1993, Rappaz 1989). While modeling of certain solidification process and phenomena on a single scale has advanced substantially,

a major challenge in the solidification modeling is to handle the disparate scales present in the physical system. Our current study will attempt to address this general issue of the solidification processes of single crystals and alloys.

In the following, we will first start with a brief discussion of the physical mechanisms that are involved in the solidification process, followed by a review of numerical–mathematical modeling of this process and a summary of current contributions.

1.1 Solidification Phenomena

1.1.1 Basic Concept

The multi–scale phenomena in the solidification process transcends the physical mechanisms from heat transfer at the system scale, the phase change dynamics at the melt/solid interface level, to the morphological evolution resulting in the formation of microstructure at the microscale (Shyy et al. 1996b, Brown 1988, Beckermann and Viskanta 1993). At the system scale, the various solidification processes are primarily concerned with the extraction of heat from the melt in a more or less controlled manner. The control of this heat transfer process can be achieved by the optimal design of materials processing devices such as furnace structure, crucible materials, heating and cooling devices, etc. In scales smaller than those of the physical components, convection and diffusive process of heat, mass and momentum take place. Still smaller, at the morphological level, not only the thermal conditions but also the material composition controls the solidification rate and the microstructure. There is a close relationship between the mechanical behavior of materials and the physical mechanisms at these disparate scales. Solidification theory plays a vital role to establish connections between processing conditions and materials properties. Details can be found in Kurz and Fisher (1989) regarding conduction effects, and in Shyy (1994) and Shyy et al. (1996a) regarding convection effects.

1.1.2 Characteristics of Single Crystals and Alloys

Depending on their solidification behavior on the phase diagram, materials can be divided into two main categories, i.e. single crystals and alloys. Figure 1.1 shows a phase diagram for a typical binary alloy system A–B. It can be seen that single crystals of pure substances or eutectic mixtures solidify at a discrete temperature. The growth of single crystals is therefore heat flow controlled.

Alloys, on the other hand, solidify over a range of temperatures as shown by the dotted line in Fig. 1.1. During this process, a mushy zone forms, where solid and liquid coexist at different equilibrium temperatures depending on different local alloy compositions. Hence, the growth of an alloy is not only heat diffusion but mainly solute–diffusion controlled. Solute redistribution in the liquid ahead of the solid/liquid interface leads to the appearance of the various growth morphologies of dendrites or eutectics of alloys which arise from undercooling.

In the following, we will review some of the recent research efforts that have been attempted in this area.

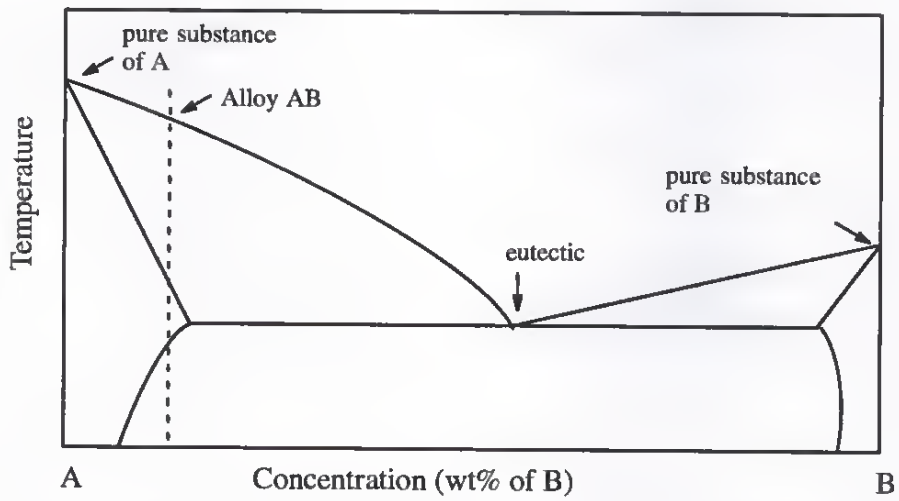

Figure 1.1. A typical phase diagram for a fictitious binary alloy system A–B.

1.2 Modeling of Solidification Phenomena

1.2.1 Modeling of Single Crystal Growth

A single crystal solidifies at a distinct temperature and hence has a sharp melt/solid interface. Therefore, the growth aspect of a single crystal depends more on the issue of heat transfer at the system scale. The heat transfer environment in a crystal growth device must yield a well controlled temperature field in the crystal and melt near the melt/crystal interface so that the crystallization rate, the shape of the solidification interface, and thermoelastic stress in the crystal can be controlled (Brown 1988).

Heat transfer in melt crystal growth systems is in general by conduction, convection and radiation. The goal of the design of heat transfer systems for any crystal growth configuration is to establish optimal processing conditions, such as a nearly constant temperature gradient laterally, along the melt/crystal interface in order to control the cooling rate of the crystal (Brown 1988).

Because of the strong nonlinearity and coupling among different mechanisms during the growth of single crystals, analytical treatments are of limited use and numerical simulation and computations have received much interest recently. In the so–called multi–domain, or front tracking method, the overall domain within which the heat flow equation is to be solved is sub–divided into two regions (liquid and solid for the Bridgman process) with a solid/liquid interface. Accordingly, one has two sets of transport equations to solve, each for a given phase. At the solid/liquid interface, boundary conditions such as heat flux have to be satisfied explicitly (Shyy et al. 1996a).

Alternatively, in the one–domain method, the solid and liquid phases are considered to be a single domain, cast in a unified mathematical expression (Shyy et al. 1996a, Crank 1984, Voller and Peng 1994). The interface is then determined implicitly as part of the solution, rather than being explicitly tracked. Also known as the enthalpy method, in the one–domain method, the energy equation can be cast into the weak form based on the

definition of enthalpy. This method has the advantage of being applicable not only to the modeling of single crystal growth but also in the simulation of alloy solidification where solidification range is exhibited for problems of mushy zone formation. This approach works well for scales beyond morphological range, and will be adopted in the present study.

1.2.2 Modeling of Alloy Solidification

The solidification process of an alloy is more complicated than that of a single crystal, as an alloy (except at the eutectic point) solidifies over a range of temperature which depends on its composition. The nonlinear coupling between the solute transport and the heat diffusion process makes the direct theoretical analysis of this process more challenging.

In the one–phase model, which is very similar to the one–domain method for the modeling of single crystal growth, macroscopic conservation equations are simultaneously valid in the mushy, solid and liquid regions and hence can be solved using a single–domain numerical solution procedure and a fixed grid. These unified macroscopic equations are derived based on the assumption that the mixture in the mushy zone has certain macroscopic properties as a function of either phase mixture (Bennon and Incropera 1987a, Voller and Prakash 1987), or a volume average (Gray 1975, Drew 1983). The main difference between these two approaches is that in volume averaging, the macroscopic equations are rigorously derived from the microscopic equations, while phase mixture theory assumes the validity of certain continuum relations on a macroscopic scale. A difficulty of the one–phase model is that relationships between the macroscopic variables of solid and liquid phase have to be specified, these are normally ~~normally~~ unknown and depend on solidification characteristics.

In the so–called two–phase model, the volume averaged macroscopic equations are utilized separately for the solid and liquid phase, respectively (Ni and Beckermann 1991). This model is claimed to have the advantage that no assumptions about the relationship between the liquid and solid velocities needs to be made, and phenomena such as floating

or settling of free solid grains can be studied. However, since the numerical solution of such a model requires explicit treatment of the boundary between the real regions over all of the mushy zone and the discretization of the governing equations must be performed on highly irregular domains, this model is much more complicated to implement numerically. In addition, detailed and accurate formulations of the interfacial conditions need to be developed.

With either a one–phase or a two–phase model, the ultimate goal of the modeling of solidification phenomena is to relate the processing conditions at the macroscopic scale directly to microstructure formation. An emerging direction in solidification modeling is concerned with the coupling of microscopic and macroscopic models (Rappaz 1989, Brown 1988, Beckermann and Viskanta 1993).

1.3 The Current Contributions

In this effort, we will address some key issues that are related to the modeling of the solidification process of single crystals and binary alloys. We have also developed numerical strategies and mathematical formulations to handle complexities arising from these issues. The focus of the present effort is on the macroscopic and component scales.

In the aspect of single crystal growth, we have developed a comprehensive computational methodology, using vertical Bridgman systems for growing NiAl and CdTe crystals as examples. NiAl is an intermetallic compound currently being investigated as a promising high temperature structural material, while CdTe is a popular choice of semiconductor substrates for infrared detector materials. The Bridgman growth system is a directional solidification method that is useful for producing large size single crystals. In this system, multi–phase processes are associated with coupled fluid flow and heat conduction, convection and radiation, variable materials properties, moving boundaries, species transport, and geometrical complexity. These complexities have traditionally resulted in simplified analyses carried out under quite restrictive assumptions of simplified

geometry, assumed boundary conditions, constant thermal physical properties and neglecting important heat transfer modes such as buoyancy driven convection.

In the present effort, to handle the physical complexity of the crystal growth process and the geometrical complexity, a pragmatic multi–level approach is devised. At the global level, the entire system consisting of the multi–components of materials and multi–modes of heat transfer has been considered. However, it is desirable to improve the grid resolution within the ampoule to capture the dynamics of the melt/crystal interface. Thus, a refined ampoule simulation was performed using the solution from the global level simulation as the boundary condition for the refined level simulation. This approach enables an accurate treatment of the solidification dynamics within the ampoule and the heat transfer through the crystal. It is evident that this kind of multi–level approach, with appropriate matching of boundary conditions, is efficient to achieve required accuracy at reasonable computing costs.

For the modeling and simulation of the vertical Bridgman growth process of NiAl system, solution characteristics for different ampoule positions are obtained via the current modeling technique. Experimental measurements of the temperature distributions inside a vertical Bridgman system for growing β–NiAl crystal have also been taken to validate the present model. Comparisons between numerical predictions and experimental results show satisfactory agreement. Based on the coordinated theoretical and experimental effort, the melting temperature of stoichiometric NiAl is reassessed. Processing conditions important for growing high quality NiAl crystals are discussed. Furthermore, with the aid of this computational tool, suggestions for design improvement are also provided.

For alloy solidification, we have derived the macroscopic transport equations of mass, momentum, heat and species based on the exact microscopic equations. These equations can be applied to all regions of solid, liquid and mushy zones. In particular, by adopting the analogous concept of subgrid scale model in the turbulent large eddy simulation, we have proposed a gradient transport model to represent the microscopic deviation terms that arise

during the derivation procedure of macroscopic equations, which has been neglected in the literature despite their importance in characterizing dendritic or eutectic evolution.

Furthermore, we have applied the mathematical model developed in this study to simulate the solidification phenomena of binary NH_4Cl–H_2O mixtures, and developed an unique numerical method allowing for the easy implementation of any types of solute diffusion model in the solid or in the liquid at the microscopic scale.

CHAPTER 2
GOVERNING EQUATIONS AND NUMERICAL METHODS FOR THE BRIDGMAN GROWTH PROCESS

In this chapter, the approach we have taken for the numerical simulation of material processing devices for single crystal growth is discussed. The vertical Bridgman growth system will be used as the illustrative example. In what follows, background about the approach we have taken for the simulation of the crystal growth process is first introduced, followed by discussions on the mathematical formulation of governing equations and development of numerical strategies.

2.1 Physical Illustration

Figure 2.1 shows a practical design of crystal growth device of vertical Bridgman growth system for NiAl crystal. This is an axisymmetric system. A water cooled ram (e.g. copper) is located at the bottom of the system. The alumina ampoule that contains the NiAl melt and seed sits on top of the ram. The resistance heater (*T4*) is applied uniformly around the ampoule wall and between them, it is filled with argon gas. During the crystal growth process, the ampoule is slowly pulled out of the heater, which is kept stationary and maintained at a stable heating temperature, and the NiAl crystal then grows gradually from the melt. According to these design characteristics, the following physical and geometrical complexities can be identified and need to be resolved carefully for the current system.

2.1.1 Physical Complexities

First, the heat transfer modes of conduction, convection and radiation are all present in the current vertical Bridgman growth system. It can be seen from Fig. 2.1 that, there are

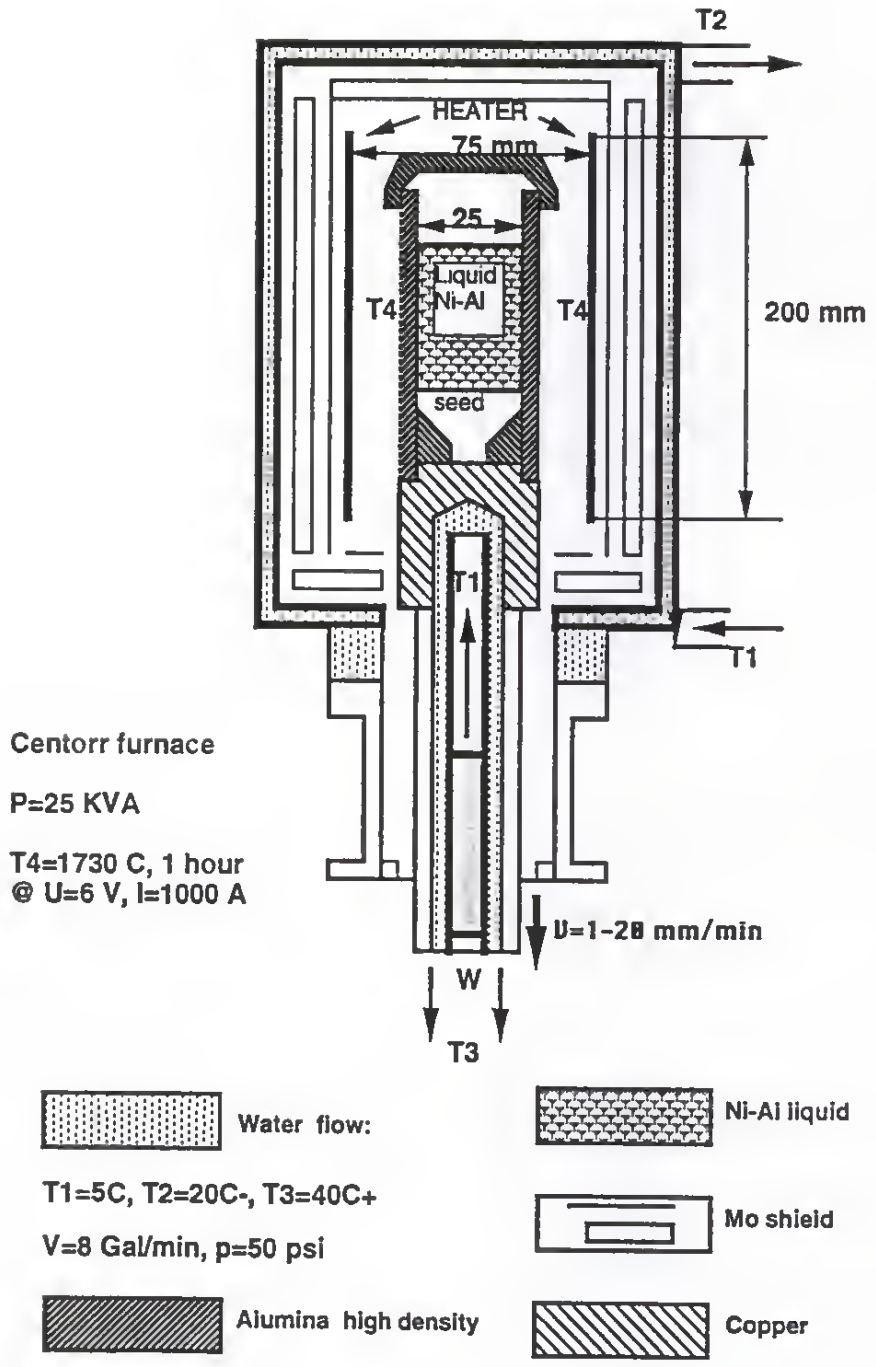

Figure 2.1. A practical design of vertical Bridgman growth system for NiAl crystal.

conduction effects among various components of the system such as the alumina wall and the copper ram, there are convection effects in the melt and in the encapsulated argon gas and there are radiation effects between the heater *T4* and the ampoule wall.

The effect of conduction heat transfer in the crystal growth device has been well documented in most of the solidification theory and text books (Kurz and Fisher 1989, Chalmers 1964). For example, by assuming no convection in the melt, an exponential profile of solute distribution in the melt can be obtained analytically for one–dimensional alloy solidification. However, the convection effect, although widely accepted as important in materials processing, has not been studied extensively until recently. Convection influences growth kinetics, impurity incorporation, compositional homogeneity, morphological stability, and nucleation of materials. The growth rate of crystals can be increased by convection up to the point where interface kinetics becomes rate controlling. Sometimes, persistent oscillatory convection patterns in the melt cause such a strong fluctuation of heat flux that the control of crystal quality becomes very difficult (Hung et al. 1995).

Sources that cause convection in a crystal growth device are many. For example, there are the buoyancy–driven convection caused by solute and temperature dependence of the density, convection induced by surface–tension gradients along melt/fluid menisci, forced convection introduced by the motion of solid surfaces, crucible and crystal rotation, etc. The need for full numerical solutions that account for all these effects is clear. However, scaling analysis for understanding roles of each of the driving forces for convection helps to compute order–of–magnitude estimates of flow intensity, identify the dominant mechanisms for transport in each conservation law, and hence simplify the problem. For example, in the vertical Bridgman system shown in Fig. 2.1, the dominating convection effect is the thermal gradient induced natural convection. The convection effect induced by the surface tension gradient is small compared to this and can then be neglected.

In addition, radiation has always been an important heat transfer mode in any crystal growth device. Sometimes it even causes strong radiation–melt interactions and hence,

should never be neglected. In the system shown in Fig. 2.1, however, radiation comes into effect only through the heat flux transfer between the vertical heater and the ampoule outer wall because the alumina ampoule is not transparent.

Second, in the ampoule region, there is the melt/crystal phase change mechanism, where the latent heat comes into effect. Latent heat released during the solidification process from the melt to solid consists of the energy needed to adjust the intermolecular spacing. Figure 2.2 shows the variation of enthalpy with temperature for a typical liquid/solid phase change process.

Third, the dependence of materials properties on temperature and composition substantially affects the processing conditions and the transport behavior in a crystal growth device. Petrushevskiiv et al. (1971) have shown that changes in temperature and material composition of molten NiAl can cause as much as a four times difference of its kinematic viscosity, and thus will affect substantially the convection characteristics and thermal diffusivity. As a result, different selections of these parameters yield different solution characteristics. In the current vertical Bridgman growth system, it has also been shown clearly by Fig. 2.3 that the thermal conductivities of copper and alumina change dramatically with temperature.

Fourth, the intrinsic complexity of multiple scales of transport process in a crystal

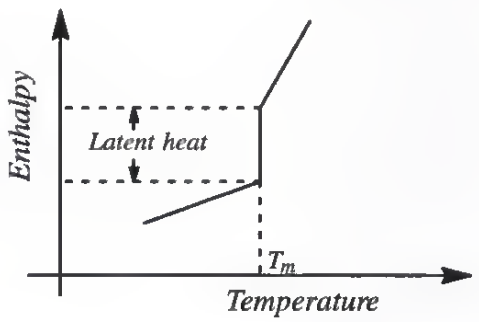

Figure 2.2. Variation of enthalpy with temperature, in which T_m is the melting temperature.

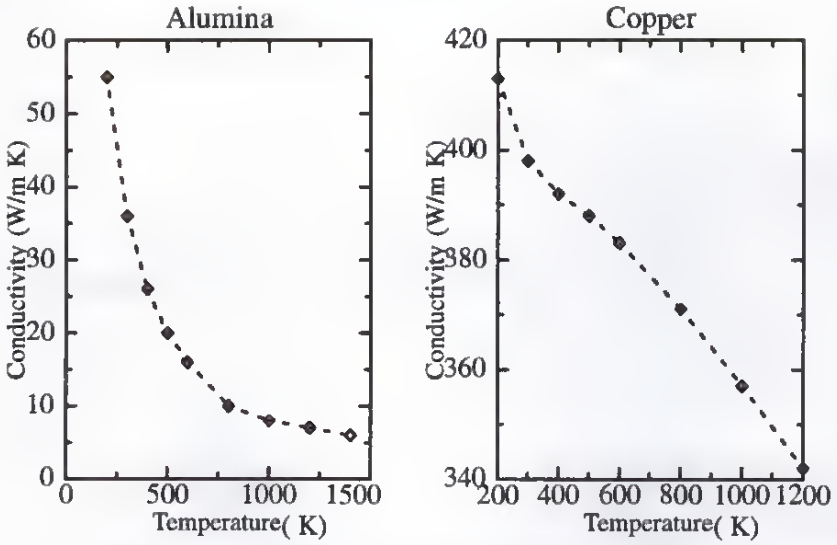

Figure 2.3. Dependency of thermal conductivities of Alumina and Copper on temperature. (Perry et al. 1984).

growth device has to be considered. For the current vertical Bridgman growth system, at the system scale there are heat transfer processes of conduction among various components, convection in the melt and in the gas and radiation between the heater and the ampoule wall. In the ampoule region, phase change dynamics and the detailed processing conditions around the interface need to be resolved accurately as they are essential to decide the interface characteristics and control the crystal quality. The morphological aspect in a single crystal growth system is not as critical as the distribution of thermal conditions such as the temperature gradient across the interface, which is an important parameter for maintaining a stable and planar interface.

There are also many other factors, such as the pulling rate of the ampoule, surface tension at the molten free surface, etc., that are involved in crystal growth devices. For the current vertical Bridgman system, these effects are not of primary influence. For example, the pulling rate of the current system is about 1mm/min, which is very slow. So the entire withdrawing process can be considered as a quasi–steady state process. Surface tension effects can also be neglected because the convection caused by this effect is rather small compared with the thermal driven buoyancy convection effect. However, these effects might

be important in other crystal growth devices such as float zone method or Czochralski method (Brown 1988).

2.1.2 Geometrical Complexities

The geometrical complexity of the current vertical Bridgman growth system as shown in Fig. 2.1 is two–fold. First, the system is composed of different types and states of materials including copper, alumina, argon gas and NiAl melt and solid. Therefore, jumps of materials properties and conjugate heat transfer between the boundaries such as gas/solid, liquid/solid and solid/ solid, have to be treated. Second, the boundary conditions for the current vertical Bridgman system are not obvious. The heating and cooling conditions can be obtained from actual temperature measurements of heater and water. However, other boundary conditions such as the Mo shield region and other places are difficult to measure and need to be specified with additional estimation.

2.2 Mathematical Formulations and Numerical Strategies

We have identified and discussed the physical and geometrical complexities that are usually present in a crystal growth device such as a vertical Bridgman growth system in the last section. We are now going to take the step of developing corresponding strategies to deal with these complexities. In order to do this, we will start with the formulation of governing equations that can characterize these physical complexities, followed by some special treatment for such effects as phase change, radiation and variable material properties. Finally, we will apply the control volume method to numerically solve these equations. A multi–level strategy will be presented to handle the geometrical complexity of the current system.

2.2.1 The Formulation of Governing Equations

For the vertical Bridgman system shown in Fig. 2.1 with combined heat transfer and phase change in a geometrically complex domain, we have derived a set of unified governing equations that describe conduction, convection and phase change phenomena over the entire geometry of the system. The dimensionless, axisymmetric, Navier–Stokes and energy equations, incorporating variable material properties and the Boussinesq approximation are as follows:

(i) Continuity equation $$\frac{\partial}{\partial r}\left(\frac{\varrho}{\varrho_0}ru\right) + \frac{\partial}{\partial z}\left(\frac{\varrho}{\varrho_0}rw\right) = 0 \tag{2.1}$$

where u and w are, respectively, the velocity components along the radial and axial direction.

(ii) Momentum equation

r–momentum: $$\frac{\partial}{\partial t}\left(\frac{\varrho}{\varrho_0}ru\right) + \frac{\partial}{\partial r}\left(\frac{\varrho}{\varrho_0}ruu\right) + \frac{\partial}{\partial z}\left(\frac{\varrho}{\varrho_0}rwu\right) = -r\frac{\partial P}{\partial r} + Pr_0\left\{\frac{\partial}{\partial r}\left(\frac{\mu}{\mu_0}r\frac{\partial u}{\partial r}\right) + \frac{\partial}{\partial z}\left(\frac{\mu}{\mu_0}r\frac{\partial u}{\partial z}\right)\right\} - Pr_0\left(\frac{\mu}{\mu_0}\right)\frac{u}{r} + Su \tag{2.2}$$

z–momentum: $$\frac{\partial}{\partial t}\left(\frac{\varrho}{\varrho_0}rw\right) + \frac{\partial}{\partial r}\left(\frac{\varrho}{\varrho_0}ruw\right) + \frac{\partial}{\partial z}\left(\frac{\varrho}{\varrho_0}rww\right) = -r\frac{\partial P}{\partial z} + Pr_0\left\{\frac{\partial}{\partial r}\left(\frac{\mu}{\mu_0}r\frac{\partial w}{\partial r}\right) + \frac{\partial}{\partial z}\left(\frac{\mu}{\mu_0}r\frac{\partial w}{\partial z}\right)\right\} + Ra_0Pr_0\left(\frac{\varrho}{\varrho_0}\right)\left(\frac{\beta}{\beta_0}\right)rT + Sw \tag{2.3}$$

(iii) Energy equation

$$\left\{\frac{\partial}{\partial t}\left(\frac{\varrho}{\varrho_0}\frac{Cp}{Cp_0}rT\right) + \frac{\partial}{\partial r}\left(\frac{\varrho}{\varrho_0}\frac{Cp}{Cp_0}ruT\right) + \frac{\partial}{\partial z}\left(\frac{\varrho}{\varrho_0}\frac{Cp}{Cp_0}rwT\right)\right\} = \left\{\frac{\partial}{\partial r}\left(\frac{k}{k_0}r\frac{\partial T}{\partial r}\right) + \frac{\partial}{\partial z}\left(\frac{k}{k_0}r\frac{\partial T}{\partial z}\right)\right\} - \frac{1}{St_0}\left\{\frac{\partial}{\partial t}\left(\frac{\varrho}{\varrho_0}rf\right) + \frac{\partial}{\partial r}\left(\frac{\varrho}{\varrho_0}ruf\right) + \frac{\partial}{\partial z}\left(\frac{\varrho}{\varrho_0}rwf\right)\right\} \tag{2.4}$$

where the term with Ra_0 in Eq. (2.3) comes from the Boussinesq approximation for treating the buoyancy effect, Su, Sw in Eqs. (2.2) and (2.3) and the term with fluid fraction f in equation Eq. (2.4) are appropriate source terms to account for the phase change, ϱ, μ, Cp, k and β are the density, viscosity, specific heat, conductivity and coefficient of thermal

expansion respectively. Ra_0, Pr_0, and St_0 are the Rayleigh number, Prandtl number and Stefan number respectively. Their definitions are

$$Ra_0 = \frac{\text{Buoyancy Force}}{\text{Viscous Force}} = \frac{\varrho_0 g \beta_0 \Delta T R_0^3}{\alpha_0 \mu_0} \tag{2.5}$$

$$Pr_0 = \frac{\text{Kinematic Viscosity}}{\text{Heat Diffusivity}} = \frac{\mu_0/\varrho_0}{\alpha_0} \tag{2.6}$$

$$St_0 = \frac{\text{Sensible Heat}}{\text{Latent Heat}} = \frac{Cp_0 \Delta T}{\Delta H_0} \tag{2.7}$$

where α_0, ϱ_0, μ_0, Cp_0, k_0, and β_0 are chosen reference material properties for nondimensionalization, g is gravitational acceleration, ΔH_0 is the reference latent heat, R_0 is the reference length, and ΔT is the reference temperature.

2.2.2 Comments on the Special Treatment

2.2.2.1 The treatment of phase change

In modeling the solidification process, due treatment needs to be taken to account for the release of latent heat during phase change. As is shown in Eq. (2.4), an enthalpy-based method (Shyy 1994, Voller 1985, Shyy et al. 1996a) has been adopted in the energy equation through the implementation of the fluid fraction f in the source term. Here f is defined to be 1 in liquid phase, 0 in solid phase, and varies continuously between the two phases. Although the melting temperature of a single crystal is uniquely defined, in the present model, phase change is considered to take place between $T_{melt}-\delta T$ and $T_{melt}+\delta T$ in order to incorporate the notion of "mushy zone". δT is a specified small range of dimensionless temperature for numerical stability, usually taken as 10^{-3}. In practice the mushy zone thickness is very thin compared to the typical dimension of a computational cell, ensuring faithful representation of the interface characteristics.

To handle both solid and liquid regions simultaneously, the source terms, Su and Sw, are included in the momentum equations (2.2) and (2.3), to ensure that the velocity in solid matches the pull rate of the crystal. The approach taken here is the inclusion of Darcy–type

source terms in the momentum equations (Shyy 1994, Shyy et al. 1996a). Thus the source terms have the form: $Su = -Au$ and $Sw = -Aw$ where A varies as a function of the fluid fraction f from zero in the liquid phase to infinity in the solid phase (Voller 1985, Shyy and Chen 1990), i.e. $A=K_0(1-f)^2/f^3$, where K_0 is a permeability constant.

2.2.2.2 The interpolation of material properties

The calculations conducted in this study take into account the variation of material properties with temperature, such as thermal conductivity, at the ampoule walls and at the melt/crystal interface. Abrupt changes in material properties may be expected at the interfaces between two media and the interpolation for the material properties must be handled carefully in order to obtain numerical solutions. The usual approach taken is linear interpolation,

$$k_e = f_e k_P + (1 - f_e)k_E \tag{2.8}$$

where f_e designates the ratio of distances between points E–e and between points e–P as shown in Fig. 2.4 with E, P, and e representing, respectively, the east–side unknown node, the present unknown node, and the east–side control surface of the present unknown cell P. Here, a standard arithmetic averaging with $f_e = 0.5$ is chosen for interpolation within the same

$$f_e = \frac{\delta_e}{\Delta_e}$$

$$f_w = \frac{\delta_w}{\Delta_w}$$

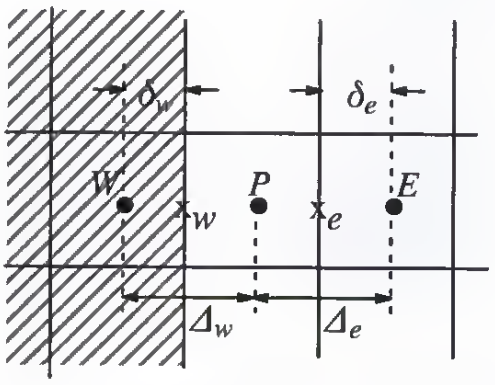

Figure 2.4. Interpolation of material properties for an interior point and a boundary point at.

material media. However, this does not handle abrupt changes at the interface between two media. Hence, following Patankar (1980), a harmonic interpolation based on a one–dimensional flux conservation is used as follows,

$$k_w = \frac{1}{(1 - f_w)/k_P + f_w/k_W} \tag{2.9}$$

This treatment has been compared with the flux balance approach (Shyy and Burke 1994) and is found to be equally robust and accurate; but simpler to implement.

2.2.2.3 Radiation effect

The radiation heat flux between the heater (*T4*) and the outer wall of the ampoule is handled by the following simplified treatment (Siegel and Howell 1981).

$$q = \frac{\sigma\,(T_a^4 - T_h^4)}{(1/\varepsilon_a) + \left(\frac{1-\varepsilon_h}{\varepsilon_h}\right)(r_a/r_h)} \tag{2.10}$$

where σ = 5.67 x 10^{-8} W/(m^2–K^4) is the Stefan–Boltzmann constant, T_a, r_a, and ε_a are temperature, radial position and emissivity for the ampoule outer wall and T_h, r_h and ε_h are corresponding variables for the heater. For the current vertical Bridgman growth system for NiAl crystal, the heater is considered to be a black body, so ε_h = 1.0. For the alumina wall of the ampoule, ε_a = 0.8 and for the copper wall, ε_a= 0.6. The expression for the boundary condition at the outer ampoule wall is given by,

$$-k\frac{\partial T}{\partial r}\Big|_{ampoule} = -k\frac{\partial T}{\partial r}\Big|_{Argon} + q \tag{2.11}$$

where the left hand side represents the heat flux into the ampoule wall and the right hand side represent the heat flux due to convection and conduction from the encapsulating gas and the radiation from the heater.

2.2.3 Numerical Method with Multi–Level Strategy

To solve the governing equations, the control volume technique employing a non–orthogonal body–fitted coordinate system has been adopted (Shyy 1994, Shyy et al.

1985, Braaten and Shyy 1986). A proven and robust pressure–based algorithm is then used to iterate the discretized form of the governing equations to the steady state (Shyy 1994, Patankar 1980).

In addition, it may be observed from Fig. 2.1 that the combination of the furnace enclosure and the ampoule presents a very complicated geometry. To render the computations tractable and simultaneously obtain adequate resolution in the ampoule region, a two–level strategy is employed. Level 1 simulates the entire domain and is referred to as the global furnace model. Level 2 concentrates on the ampoule region and obtains its boundary conditions from the level 1 or the global simulation. With this two–level strategy, we can obtain useful information at the global level and yet obtain adequate resolution at the melt/crystal interface. Figure 2.5 demonstrates the application of the two–level strategy to the present simulation.

2.3 Closure

In this chapter, we have discussed the physical and geometrical complexities that are typically present in a crystal growth device. The special case of a vertical Bridgman growth system of NiAl is chosen to help illustrate the physical issues involved. Based on this illustration, we have also formulated the corresponding governing equations that can account for the effects such as conduction, convection heat transfer and phase change dynamics. Furthermore, we have also developed special treatment to deal with variable material properties, radiation effects, etc. Especially, we have proposed a multi–level approach to handle the geometrical complexity in the system for a purpose of obtaining accurate processing conditions near the interface while maintaining a reasonable computer cost. In the following two chapters, we are going to apply the method developed in this chapter to the modeling and simulation of two types of crystals of NiAl and CdTe.

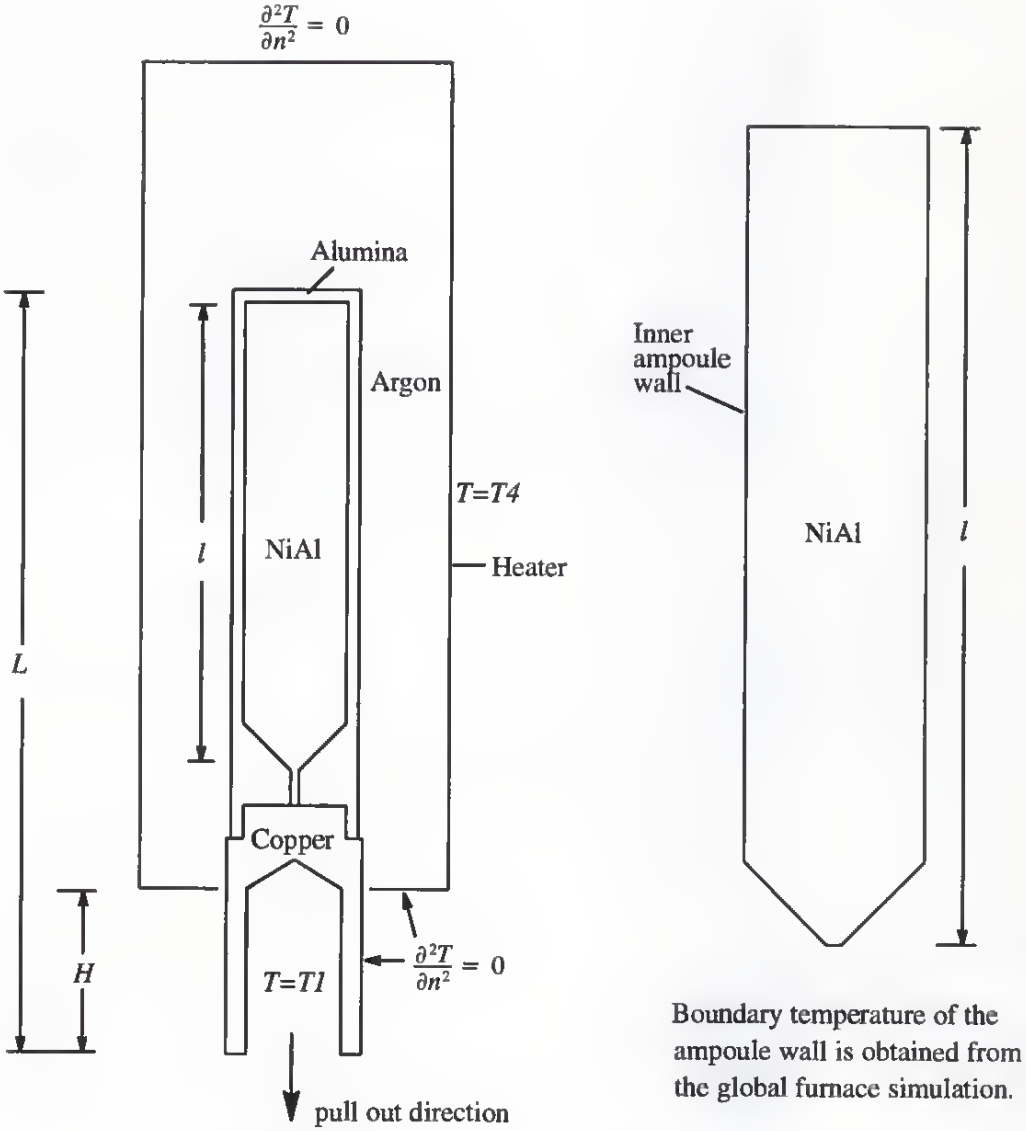

Figure 2.5. Layout and boundary conditions for (a) the global furnace model, and (b) the refined ampoule model used in the present numerical simulation, where H measures the ampoule position as it is pulled out. The total length of the ampoule part, between the top of Alumina and the bottom of Copper, is $L = 185$ mm, while the length of the ampoule is $l = 113.5$ mm.

CHAPTER 3
MULTI–LEVEL SIMULATION OF VERTICAL BRIDGMAN GROWTH OF NiAl CRYSTAL

In this chapter, we are going to simulate in detail the vertical Bridgman system for the single crystal growth of NiAl. A two–level simulation will be performed to simultaneously achieve accuracy as well as computational economy. To validate the current numerical model, experimental measurements of temperature profiles at designated locations in a vertical Bridgman growth system will be conducted and compared with the modeling predictions. To help optimize the thermal conditions for growing single crystal NiAl with desired quality, parametric variations will also be considered in numerical simulations. Furthermore, the exact melting temperature of NiAl does not seem to have been ascertained; combining the computational and experimental information, the correct value of the melting temperature will be assessed.

3.1 Background

β–NiAl, having a composition of 50 at. % Ni, 50 at. % Al, with a CsCl, B2 crystal structure, is an intermetallic that is currently being investigated as a promising high temperature structural material for application in the next generation of aircraft engines and structural components. NiAl is especially attractive because of its low density, high thermal conductivity, high melting temperature, superior isothermal and cyclic oxidation resistance (Sen and Stefanescu 1991, Darolia 1991). Its high melting temperature above 1640 C allows it to sustain high operating temperature and increase gas efficiency; its low density of $5.95 g/cm^3$ of approximately two–thirds the density of state–of–the art nickel–based superalloys helps to reduce the turbine rotor weight (blades and disk) by as much as 40%;

its high thermal conductivity of 4 to 8 times that of nickel–based superalloys allows the temperature distribution in a NiAl turbine blade to be much more uniform, and the life limiting "hot spot" temperature is reduced by as much as 50 C; finally, its excellent oxidation resistance makes it widely useful for coating on virtually all high–pressure turbine blades and vanes of aircraft engines.

The physical and mechanical properties of NiAl depend strongly on both its composition and temperature (Levit et al. 1996, Noebe et al. 1993, Vedula et al. 1985, Takasugi 1992, Sen and Stefanescu 1991, Darolia 1991). Figure 3.1shows the NiAl binary phase diagram (Noebe et al. 1993). At the stoichiometric composition (50 at. % Ni, 50 at. % Al), NiAl has its lowest yield strength and highest ductility, and the transition temperature from brittle to ductile behavior (BDTT) is at a minimum (Noebe et al. 1993). Impurity content and deviations from stoichiometry can significantly change these properties. For example, it has been found that single crystal NiAl with improved purity (Levit et al. 1996) or with small (<1%) additions of iron, gallium or molybdenum (Darolia 1991) yields

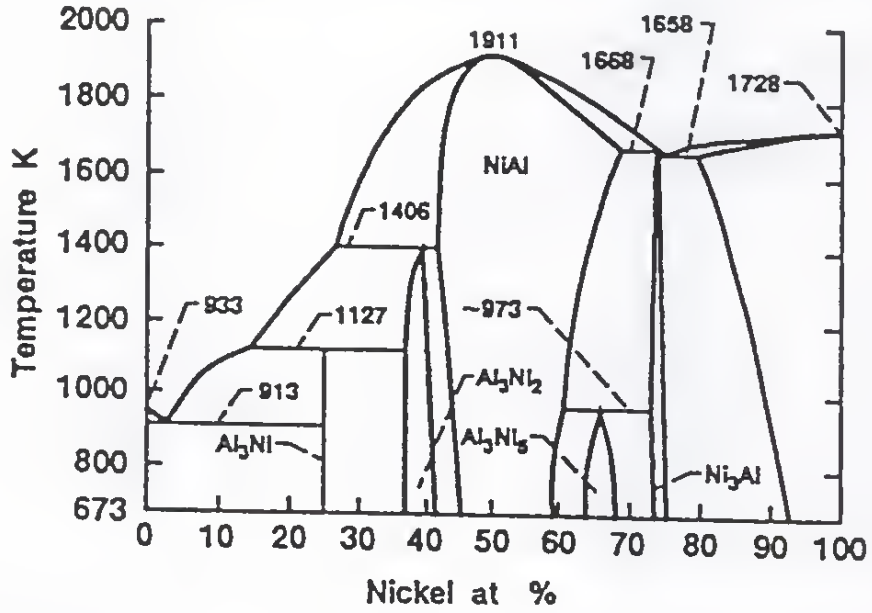

Figure 3.1. NiAl phase diagram.

substantial increases in ductility at room temperature. As far as the temperature effect is concerned, it has been widely recognized that NiAl, like most other intermetallics, has the drawbacks of poor ductility at room temperature and low strength at elevated temperature, inspite of its many other superior advantages (Noebe et al. 1993, Sen and Stefanescu 1991, Darolia 1991). These problems need to be resolved before NiAl will be useful in structural applications as a high temperature material.

The present work represents part of a systematic effort conducted with the goal of understanding the behavior of NiAl from two aspects, i.e. the influence of alloying and processing on the structure and properties of NiAl. Alloying mostly deals with the procedure of additions of certain elements or other precipitates to the single crystal for the purpose of property enhancement. Processing, on the other hand, is mainly concerned with the change of thermal conditions by factors such as selection of ampoule materials, set–up of heating and cooling temperatures, and variation of growth speed. The current study is focused on the processing conditions in a vertical Bridgman system for growing single crystal β–NiAl. The information obtained facilitates a better understanding of the various processing parameters, which, in turn, offer guidance to adjust the processing environment for enhancing crystal quality and composition control.

The Bridgman growth system is one of the directional solidification configurations that are useful for producing large size single crystals from the melt. The advantage of the Bridgman system is that the temperature gradients can be controlled, making it possible to achieve unidirectional solidification. A practical design of the vertical Bridgman system for growing NiAl crystals has been shown in Fig. 2.1. The material properties of each of the components in the system is listed in Table 3.1.

In the present study, initially, the raw material of NiAl is vacuum induction melted and chill cast into a rod with a desired size. The rod is then removed from the chill mold, placed in a high density refractory (e.g. alumina) ampoule, which is situated on top of a water cooled ram (e.g. copper), remelted and then directionally solidified by slowly withdrawing the

ampoule/ram assembly from the hot zone. In most cases, a single crystal seed is placed between the chill and the feedstock in order to preselect the orientation of the single crystal NiAl.

As discussed in detail in the last chapter, the temperature distribution in crystal growth systems, such as the Bridgman system, is highly complex and is influenced by several factors such as varying thermo–physical properties and multiple heat transfer modes, namely, conduction, convection and radiation, and phase change dynamics. These complications have traditionally resulted in simplified analyses carried out under quite restrictive assumptions of simplified geometry, assumed boundary conditions, constant thermo–physical properties and neglecting important convection modes such as buoyancy driven convection. In what follows, however, we are going to apply the solution strategies we developed in the last chapter to simulate fully the thermal and solidification characteristics of the entire vertical Bridgman growth system, accounting for all effects of the coupled heat transfer processes, phase change dynamics, complex geometry, as well as variable material properties.

Table1 3.1 Material Properties in the Vertical Bridgman Growth System

Material	ϱ (kg/m^3)	μ (kg/m-s)	k (W/m-K)	C_p (J/kg-K)	β (K^{-1})
NiAl	5950	0.005	75	660	1.52×10^{-5}
Argon	0.487	5.42×10^{-5}	4.27×10^{-2}	520	8.33×10^{-4}
Alumina	3975	†	‡	765	–
Copper	8930	†	‡	386	–

ΔH_0=688 kJ/kg
† Assigned big values
‡ Varied with temperature (see Fig. 2.3)

In this study, we chose the properties of β–NiAl at room temperature as the reference properties, the radius of ampoule inner wall, R_0, as the reference length and the difference between the highest and the lowest temperature in the furnace, $\Delta T=T4-T1$, as the reference temperature scale. The estimated dimensionless parameters for our current calculation are:

Ra_0=3.2 x 10^4 Pr_0=4.4 x 10^{-2} St_0=1.7

Furthermore, the original parameters of material properties for different material regions, which have been listed in Table 3.1, are converted also correspondingly into dimensionless form as listed in Table 3.2. The computational results and the experimental validation are discussed and shown next.

Table 3.2 Dimensionless thermodynamic and transport properties

Material	ϱ/ϱ_0	$Pr_0(\mu/\mu_0)$	k/k_0	C_p/C_{p0}	$Ra_0Pr_0(\beta/\beta_0)$ (ϱ/ϱ_0)
NiAl	1.0	4.4 x 10^{-2}	1.0	1.0	1.4 x 10^3
Argon	8.2 x 10^{-5}	4.77 x 10^{-5}	5.7 x 10^{-4}	0.79	6.32
Alumina	0.67	†	‡	1.16	–
Copper	1.5	†	‡	0.58	–

3.2 Simulation and Measurement of NiAl System

3.2.1 Two–Level Modeling Result

In this section, we present the results of steady state calculations for the Bridgman growth of NiAl. The geometry of the calculation domain has been shown in Fig. 2.5a and b. In order to optimize computational costs without sacrificing accuracy and resolution in the melt/crystal region, the simulation was conducted at two levels. Level 1 is the global furnace simulation involving the entire domain. Level 2 is a refined ampoule simulation and takes its boundary conditions based on the global simulation. It will be shown later that the global simulation is relatively insensitive to the details of the interface morphology. We also try to take into account the relative displacement of the ampoule as the growing crystal is pulled out of the furnace. Therefore, three simulations have been performed at the global level involving three different locations of the ampoule. A multi–zone patched grid method has been employed to generate the grid system needed for global (furnace) level simulations. Sample grid distributions have been shown in Fig. 3.2 (a) and (b) for H = 40 mm and 80 mm, where H indicates the position of the ampoule within the furnace. The global furnace (Level

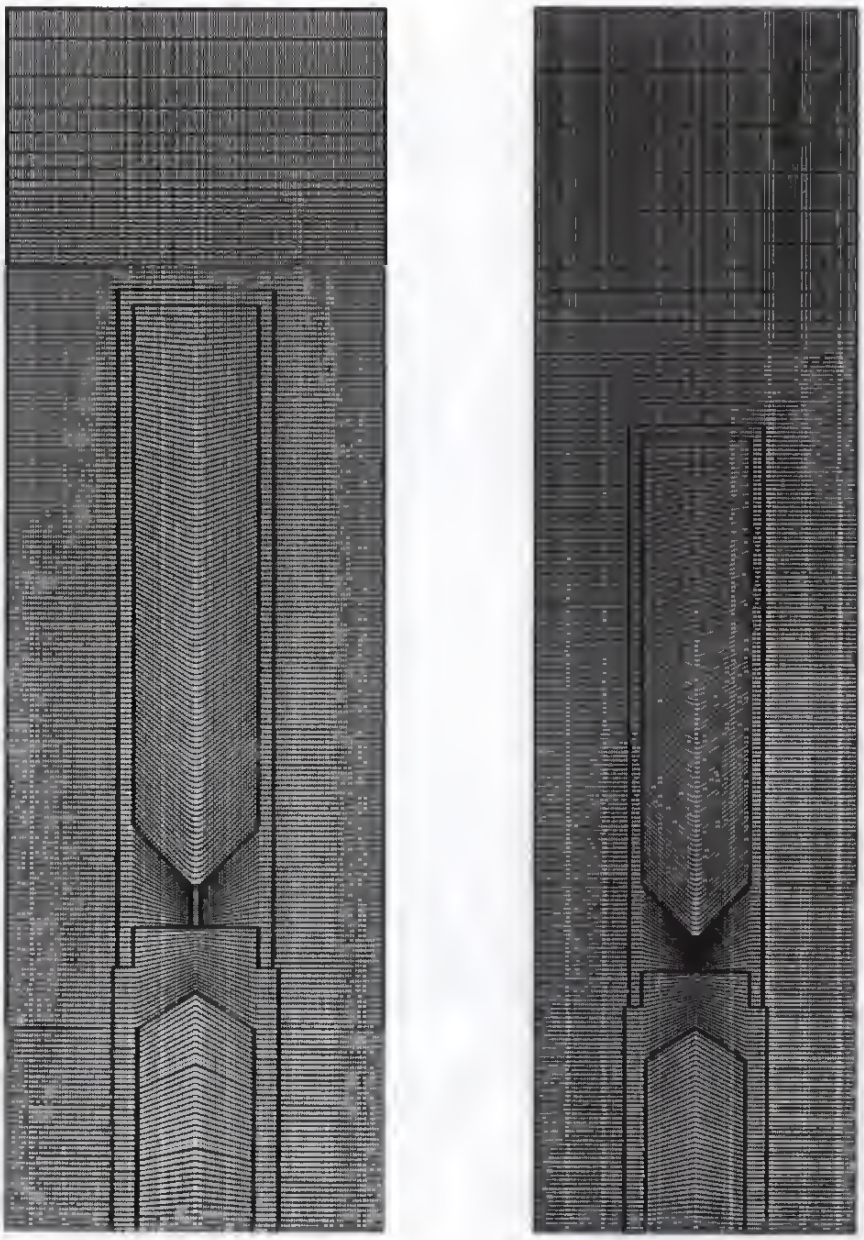

(a) Grid of H=40mm *(b) Grid of H=80mm*

Figure 3.2. Grid distributions for the global furnace model of (a) H=40mm (Grid size = 151x213), and (b) H=80mm (Grid size = 151x216).

1) simulations were conducted for three different ampoule positions in order to estimate the effects of geometric variations as the crystal is pulled out of the furnace. Calculations were conducted for H = 40 mm (151x213 grid), 80 mm (151x216 grid) and 120 mm (151x219 grid). In all cases, there were 51x103 points in the ampoule region. Based on this resolution, the ampoule region is then computed again with a better resolution; the boundary conditions needed for this Level 2 simulation are extracted from the results obtained from the Level 1 solutions.

In the following, we will first show that consideration of realistic material property variation, as, e.g., functions of temperature, is essential to obtain a faithful simulation; we will then discuss the solutions obtained for different ampoule locations on both Level 1 and Level 2.

3.2.1.1 The global furnace simulation

Figures 3.3 show the streamfunction and the isotherm distribution, respectively, for each of the three ampoule locations. The streamline pattern arises as a result of buoyancy driven convection. It may be observed that the convection pattern in the encapsulating gas is quite weak and the convective heat transfer into the ampoule is negligible compared to the radiative effect from the heater. As the ampoule translates downward, the convection within the ampoule gets slightly weaker and the melt/crystal interface becomes convex towards the melt. It is difficult to predict the strength and detailed characteristics of the convective field within the argon gas because the geometry is complicated and the boundary conditions vary with the ampoule movement. Nevertheless, it is clear that the isotherm pattern changes quite significantly as the crystal is drawn down and the temperature gradients at the base of the crystal decrease in magnitude.

To shed some light on the role played by the variations of the transport properties, with respect to temperature, calculations have also been conducted with the material properties held fixed to the reference values at room temperature, a practice employed in some

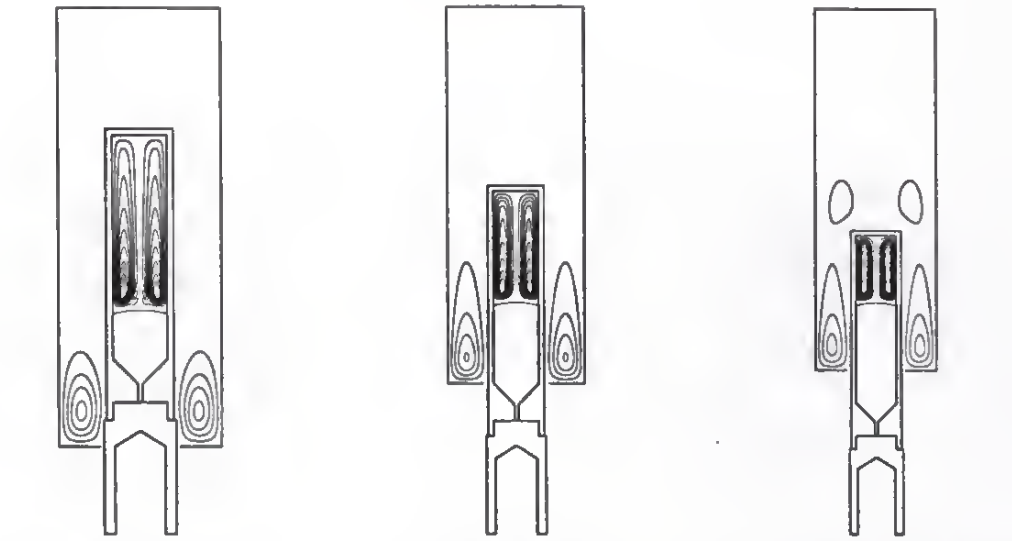

(a) Streamfunction

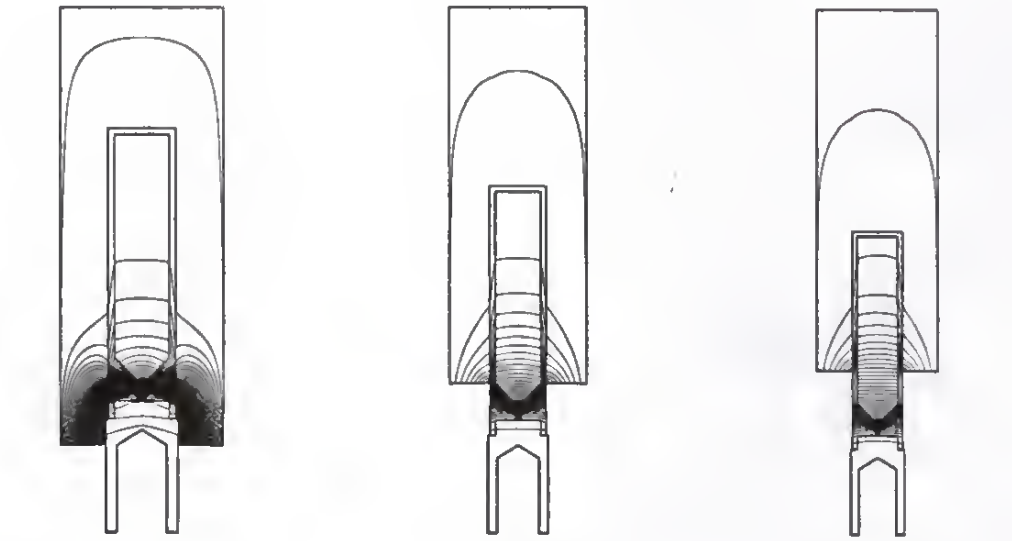

(b) Isotherm

Figure 3.3. Solution characteristics of the global simulation of NiAl system for three different H. (i) H=40mm (ii) H=80mm (iii) H=120mm. Ra_0=3.2x10^4, Pr_0=4.4x10^{-2}, and St_0=1.7

modeling work. While the general patterns of stream functions and isotherms seem insensitive, some critical aspects of the solutions are substantially affected. As an illustration, Fig. 3.4 shows the differences in the temperature distribution along the centerline and the inner wall of the ampoule, between the variable properties and constant properties simulations. Noticeable differences have been observed; for example, a 50 % difference exists along the bottom wall of the ampoule. The differences exhibited in Fig. 3.4 impact the temperature distribution in the crystal and its accurate prediction is necessary to understand its implications on crystal quality.

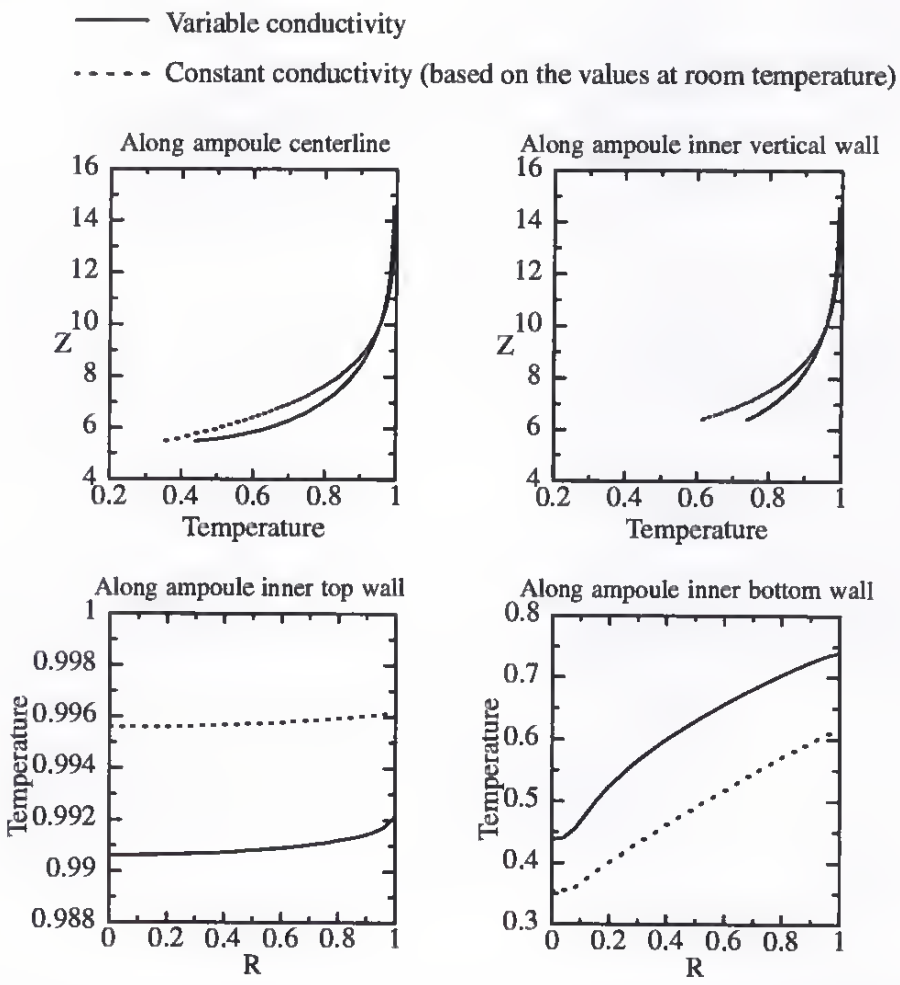

Figure 3.4. Comparison of the temperature profiles of the global furnace model with variable and constant thermal conductivities of Alumina and Copper for H=80mm.

3.2.1.2 The refined ampoule simulation

The refined ampoule (Level 2) simulation was conducted using the ampoule wall temperature distribution, obtained from Level 1, as the boundary condition. The grid resolution within the ampoule has been increased to 101x154 from 51x103 used at Level 1. Stream function and isotherm contours are presented in Fig. 3.5. Noticeable differences may be observed between the convection patterns in Fig. 3.3a (i–iii) and Fig. 3.5a (i–iii), and more significantly, the convection strengths are different, especially for H = 40 mm. At this ampoule position, more detailed secondary vortical structure in the central region above the solid–melt interface can be clearly observed from the refined solutions depicted in Fig. 3.5; at the global level, as shown in Fig. 3.3, such characteristics are less pronounced. This assessment shows that a fine grid is needed to capture convection dominated phenomena thus justifying the two level approach taken in this study.

Figure 3.6 contrasts the melt/crystal interface obtained from the two level simulation for all three ampoule locations. It may be observed that the differences between the coarse grid (Level 1) and the fine grid (Level 2) calculations are most significant when the melt volume decreases (as the crystal is pulled out). This observation just reinforces the trends exhibited in the stream function plots mentioned previously. The sensitivity to grid refinement increases as the melt volume decreases because of the constraining effect of the top wall. Since interface positions at the ampoule wall are the same between the two grid levels, it is significant that the temperature distributions predicted on them are different, resulting in different melt/crystal curvatures. This aspect impacts on the detailed distribution of temperature gradients in the interface region, resulting in different microstructures of the crystal.

To further illustrate the usefulness of the multi–level approach, a fine grid simulation of the H = 40 mm case, corresponding to Fig. 3.3a (i) and Fig. 3.5a (i), was carried on a refined grid of 223x284 nodes (73x154 nodes in the ampoule region). This represents a substantial refinement over the grid system shown in Fig. 3.2a with 151x213 nodes (51x103

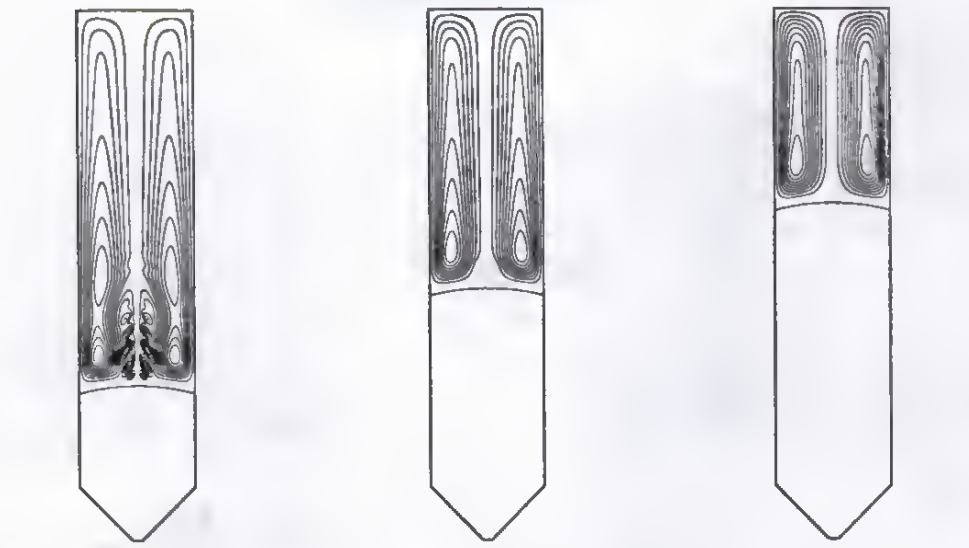

(a) Streamfuction

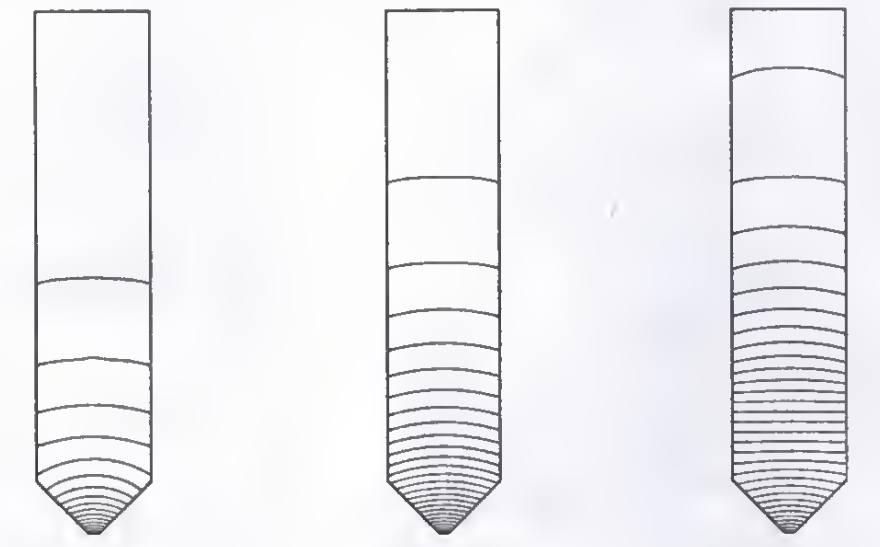

(b) Isotherm

Figure 3.5. Solution characteristics of the refined ampoule simulation of NiAl system for three different H. (i) H=40mm (ii) H=80mm (iii) H=120mm. Ra_0=3.2x10^4, Pr_0=4.4x10^{-2}, and St_0=1.7

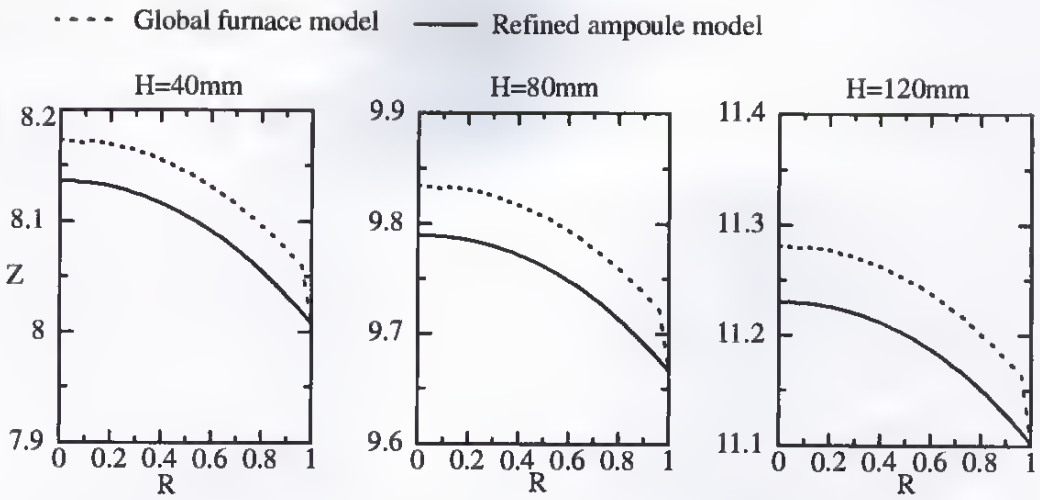

Figure 3.6. Comparison of the melt/solid interface positions between global furnace and refined ampoule models.

nodes in the ampoule region). Figure 3.7 a and b show the streamfunction and isotherms, respectively, obtained on this fine grid system. It can be observed that the fine grid solution captures more details of the convection pattern within the ampoule. Differences can be noted between the solutions presented in Fig. 3.3 and those presented in Fig. 3.7; more secondary vortical structures are captured on the fine grid. The fine grid solution is closer to the refined ampoule simulation (Fig. 3.5) than to the coarse grid solutions from the global furnace simulation. The fine grid results of the global furnace simulation clearly demonstrate the economy of the multi–level approach; instead of resorting to a fine grid distribution at the global level, carrying out the refined ampoule simulation yields the desired accuracy economically.

It has been shown above that the computational model we have developed, accounting for the combined effects of phase change, conduction/convection/radiation heat transfer, variable material properties and complex geometry, has been applied successfully to capture in detail the solution characteristics inside a vertical Bridgman growth system for NiAl crystal in an accurate and economic way. In the following section, we will further conduct the corresponding experiment to validate the current model.

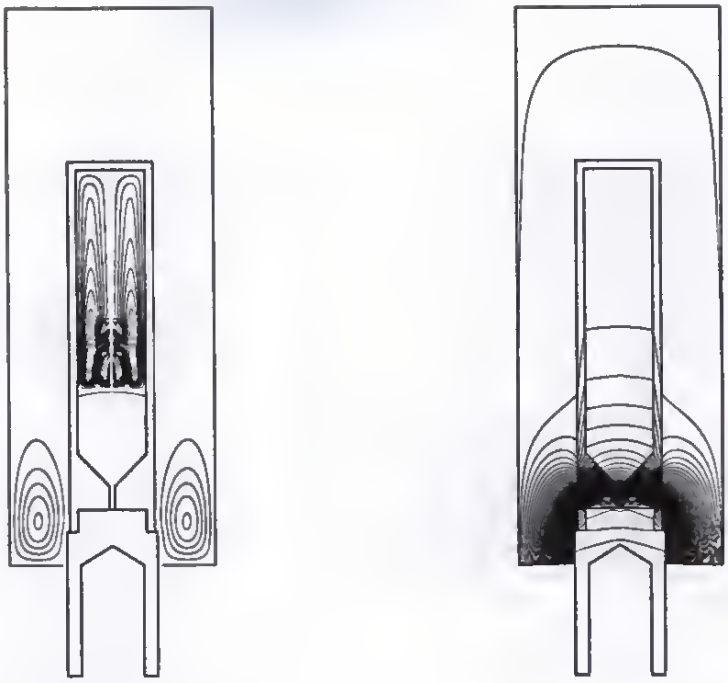

Inside the NiAl melt
Smax=4.18x10^{-2}, ΔS=4.4x10^{-3}
Inside the Argon gas
Smax=2.42x10^{-3}, ΔS=4.4x10^{-3}

(a) Streamfunction

T_{melt}=0.95 ΔT=0.02

(b) Isotherm

Figure 3.7. Solution characteristics of the global refined simulation of NiAl system for H=40mm with a total grid size of 223x284. Ra_0=3.2x10^4, Pr_0=4.4x10^{-2}, and St_0=1.7.

3.2.2 Experimental Procedure

3.2.2.1 System set–up

Compared to the previous schematic of Fig. 2.1, in this experimental set–up, the ampoule inner diameter has been increased from 25mm to 29mm diameter to grow a bigger size crystal. The feedstock of NiAl was prepared by vacuum induction melting and chill casting into a 28mm diameter rod, with a 5mm diameter hole in the center to allow for installation of a thermocouple.

Four type C tungsten–rhenium thermocouples with 3mm diameter were installed for measuring the temperature profiles and furnace hot zone temperature during the crystal growth process. Figure 3.8 shows the detailed arrangement of these thermocouples.

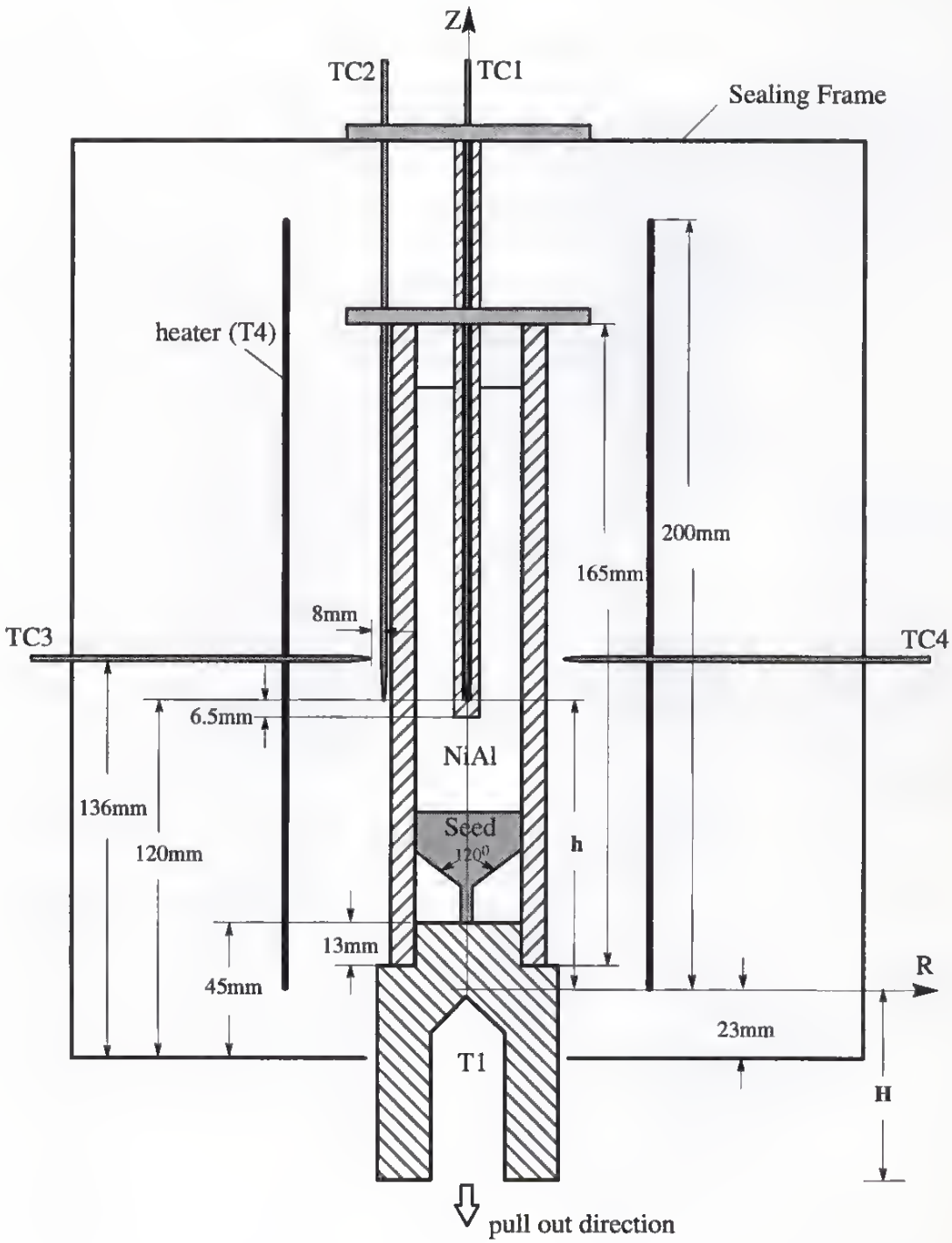

Figure 3.8. Setup of thermocouples for the experimental measurement of temperature.

Thermocouple 1 (TC1) was positioned along the centerline of the NiAl feedstock. To protect this thermocouple from reaction with the NiAl during the melting process, it was enclosed by an alumina tube that has 3mm inner diameter and 5mm outer diameter with a tip length of 6.5mm. This arrangement also allows thermocouple 1 to translate vertically along the NiAl centerline. Thermocouple 2 (TC2) was positioned along the outer ampoule wall and was also allowed to translate vertically. In addition, thermocouples 3 and 4 (TC3 and TC4) were fixed horizontally at about one-half height of the heater. They were used to help monitor the thermal condition in the furnace hot zone during the entire crystal growth process. All thermocouples were calibrated before the installation. However, it has to be mentioned that the confident limit for type C thermal couple is 1%.

The relative positions of the various components in the system were measured with respect to the baseline of the sealing frame as shown in Fig. 2.5 and Fig. 3.8. While the relative positions of the ampoule and thermocouples are taken with respect to the bottom of the heater, shown in Fig. 3.8 by the horizontal radial axis R. The ampoule position is denoted by *H*, which is initially set as 43mm. As the ampoule is pulled down, this number increases. h denotes the tip positions of thermocouple 1 or 2. Because of the interior complexity and small scale of the current system, the measurement of positions is estimated to have a confidence limit of $\pm$ 1mm.

3.2.2.2 Temperature measurement

In the course of making temperature measurements, the system was first heated up for about three and one–half hours until TC3 and TC4 reached 1740 C. Then the system was held for another 30～45 minutes to allow the NiAl feedstock to completely melt. Next, the ampoule/ram assembly was withdrawn from the furnace and stopped at designated positions to allow TC1 and TC2 to take measurements at different positions, as described next.

After the NiAl feedstock was fully melted, the alumina tube with thermocouple TC1 was moved down through the melt until it stopped and touched the melt/solid interface.

Hence, the interface position for the initial ampoule position of H=43 mm could be located. Thereafter, the alumina tube remained at this position, whereas TC1 was allowed to translate vertically. Once temperature readings from TC 1 and TC2 were stable, TC1 and TC2 were moved to a new height and the corresponding temperatures were obtained. It is mentioned that, for the convenience of measurement, TC1 and TC2 were always moved in tandem.

Table 3.3 Temperature versus Thermal Couple Positions (h) for Different Ampoule Positions (H)

H (mm)	Thermocouple 1 (Located along the NiAl centerline)						
43	h (mm)	82	88	98	108	118	
	T (C)	1737	1752	1766	1774	1778	
59	h (mm)	63	78	88	98	108	
	T (C)	1733.5	1762	1773.5	1779	1781.5	
67	h (mm)	56	68	83	93	103	
	T (C)	1733	1758	1772.5	1782	1784	
77	h (mm)	54	58	68	78	88	
	T (C)	1751.5	1757.5	1771.5	1780	1785	
87	h (mm)	54	63	73	83		
	T (C)	1762	1773	1780	1780		
97	h (mm)	54	58	68	73		
	T (C)	1767	1770	1777.5	1780		
H(mm)	Thermocouple 2 (Located along the ampoule outer wall)						
43	h (mm)	82	88	98	108	118	
	T (C)	1780	1786	1791	1794.5	1795.5	
59	h (mm)	54	63	78	88	98	108
	T (C)	1761	1773	1786.5	1791	1792.5	1793
67	h (mm)	56	68	83	93	103	
	T (C)	1772.5	1783	1792	1793.5	1794.5	
77	h (mm)	54	58	68	78	88	
	T (C)	1778.5	1781.5	1788	1792.5	1794	
87	h (mm)	54	63	73	83		
	T (C)	1778.5	1787	1790	1793		
97	h (mm)	54	58	68	73	83	93
	T (C)	1781.5	1783.5	1788.5	1790.1	1793	1793.5

After measurement at various h positions were made, the ampoule/ram assembly was withdrawn and stopped at a designated new ampoule position, e.g. *H*=59mm, where temperatures were once again measured. This process was repeated until the desired number of ampoule positions were measured. In the present work, temperature profiles, along the NiAl centerline and the ampoule outer wall, were measured for a total of six ampoule positions, i.e. *H*=43mm, 59mm, 67mm, 77mm, 87mm and 97mm.

Table 3.3 and Fig. 3.9 summarize the data collected. The number of data points collected decreases as the ampoule is pulled out (*H* increases), since the thermocouples transverse a smaller length. In addition, the interface position was only obtained for the first ampoule position of *H*=43mm. The measured interface position, with respect to the bottom line of the heater (R axis), is 75mm. This number is checked once again after the experiment when the solidified NiAl ingot was broken and the position of the tip trace of the alumina tube was measured. The results showed that the confidence limit for the interface

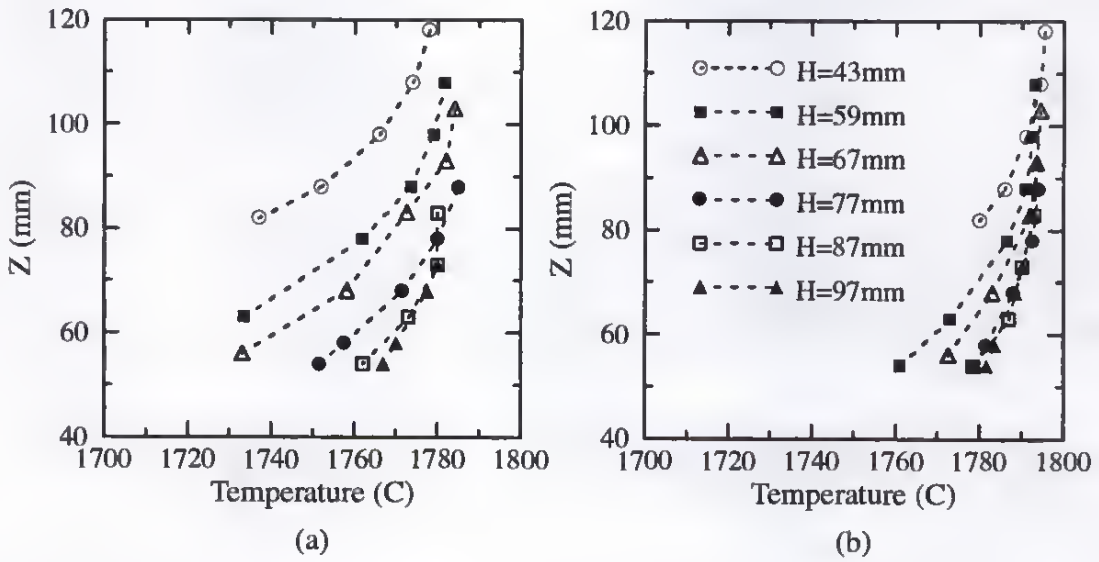

Figure 3.9. Experimental result of temperature profiles along (a) the NiAl centerline, and (b) the ampoule outer wall for different ampoule position H.

measurement is about ± 2mm. During the entire experimental process, a stable furnace temperature of 1740 ± 1 C (monitored by TC3/TC4) was maintained by manually adjusting the input power about a baseline value of 7 kW.

3.2.2.3 Experimental observation

From Table 3.3 and Fig. 3.9, it can be seen that the temperature measured along the outer ampoule wall can be up to 1796 C, which is higher than the value of 1740 C measured by TC3/TC4. Even at the same height, the temperature value at the ampoule outer wall is about 40 C degrees higher than that of TC3/TC4, although their horizontal gap is only about 8 mm as shown in Fig. 3.8. It is also observed that, when TC3 or TC4 touches the ampoule outer wall, it yields the same temperature as that is measured by TC2. However, when TC3 or TC4 is pulled horizontally away from ampoule, its temperature reading drops significantly. The cause of this substantial discrepancy of temperature is unclear at present, but might be explained by the effect of radiation view factor. Figure 3.10 shows this situation more clearly in a top view of the system. It can be seen that the tips of TC3 and TC4 both face directly to the ampoule wall instead of the heater, hence they receive less radiation from the heater than TC2, resulting in a lower temperature. In addition, it is also observed from

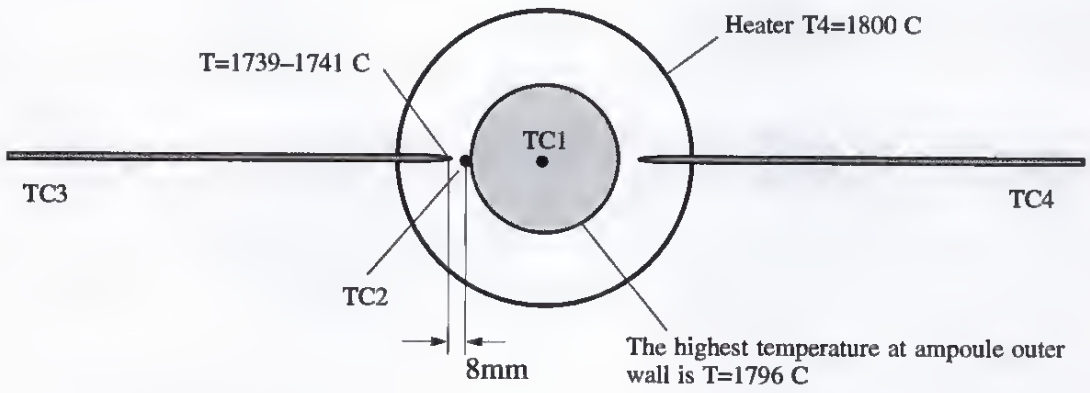

Figure 3.10. The top view of the arrangement of thermocouples in the NiAl furnace.

Fig. 3.9 that the temperature gradient in the axial direction is higher at the lower portion of the ampoule than at the higher portion of the ampoule. As the ampoule is pulled out (*H* increases), temperature profiles along both the NiAl centerline and the ampoule outer wall become more unified.

3.2.3 Comparison with Numerical Result

3.2.3.1 Modeling considerations

To compare modeling result with experimental measurement within a reasonable scope, several modifications to the model have been made to meet the specific conditions adopted in the current experiment. First, as explained previously, the geometry of the experimental system had to be changed to accommodate the thermocouples. The inserted alumina tube at the NiAl centerline, for protecting TC1 from corrosion by the NiAl melt, has a diameter about one sixth of the ampoule inner diameter of 29mm. Hence, the interference caused by the alumina tube had to be considered.

The second change is in boundary condition specification. In the previous calculation, we used *T4*=1740 C as the heater boundary condition, which is actually the temperature measured by TC3/TC4. From the observations of the experiment, we found that heater temperature is actually higher than this. Since the highest temperature along the ampoule outer wall is about 1796 C, the heater temperature *T4* was selected as 1800 C, based upon previous numerical results which showed a 3 to 5 C difference in temperature between the heater and the alumina wall. The cooling water temperature ranged from 5 to 10 C (city water). When the cooling water reaches the copper ram, it will be warmed up somewhat, so we use the upper limit of *T1*=10 C as the cooling boundary condition. For the rest of the boundaries in the furnace, temperature boundary conditions are difficult to be given directly. Estimation can be made, though, according to the experimental characteristics. We have mentioned that, during the entire crystal growth process, the furnace hot zone temperature was maintained at a stable value of 1740 C by manually adjusting the stable power input.

In another words, a condition of constant heat flux into the system is maintained. So the thermal boundary conditions of constant heat flux for the remaining furnace boundaries is taken, i.e., $\partial T^2/\partial n^2 = 0$.

The third consideration is the the accurate specification of material properties as a function of temperature. This is a very important factor in obtaining accurate numerical result. As shown in Table 3.2 or Fig. 3.9, the majority of the alumina ampoule is exposed to a temperature range above 1700 C, which exceeds the upper threshold 1127 C (1400 K) of conductivity as a function of temperature, *k(T)*, as shown in Fig. 2.3 (Perry et al. 1984). Therefore, in this modeling effort, conductivity of alumina above *T=1127 C* has been estimated by extrapolation of the gradient of *k(T)* at *T=1127 C*.

3.2.3.2 Modeling result

A similar set up of the computational domain as shown in Fig. 2.1 is applied here, except that the alumina tube has been considered in this case. In the present, all six ampoule positions measured in the experiment are simulated and the computational results are compared with experimental data as follows.

(i) Comparison of temperature profiles

Figures 3.11 and 3.12 show that the temperature distribution along the NiAl centerline and the ampoule outer wall obtained from the computational simulation matches the experimental measurements well overall. Satisfactory agreement is observed for all six ampoule positions, especially for the temperature along the outer alumina wall. This implies that the simplified radiation model we currently used for computing the heat flux between the alumina outer wall and the heater is accurate, and the boundary condition of constant heat flux at the heater bottom is reasonable. Along the ampoule centerline, agreement between experimental data and computational result is good for the three higher ampoule positions

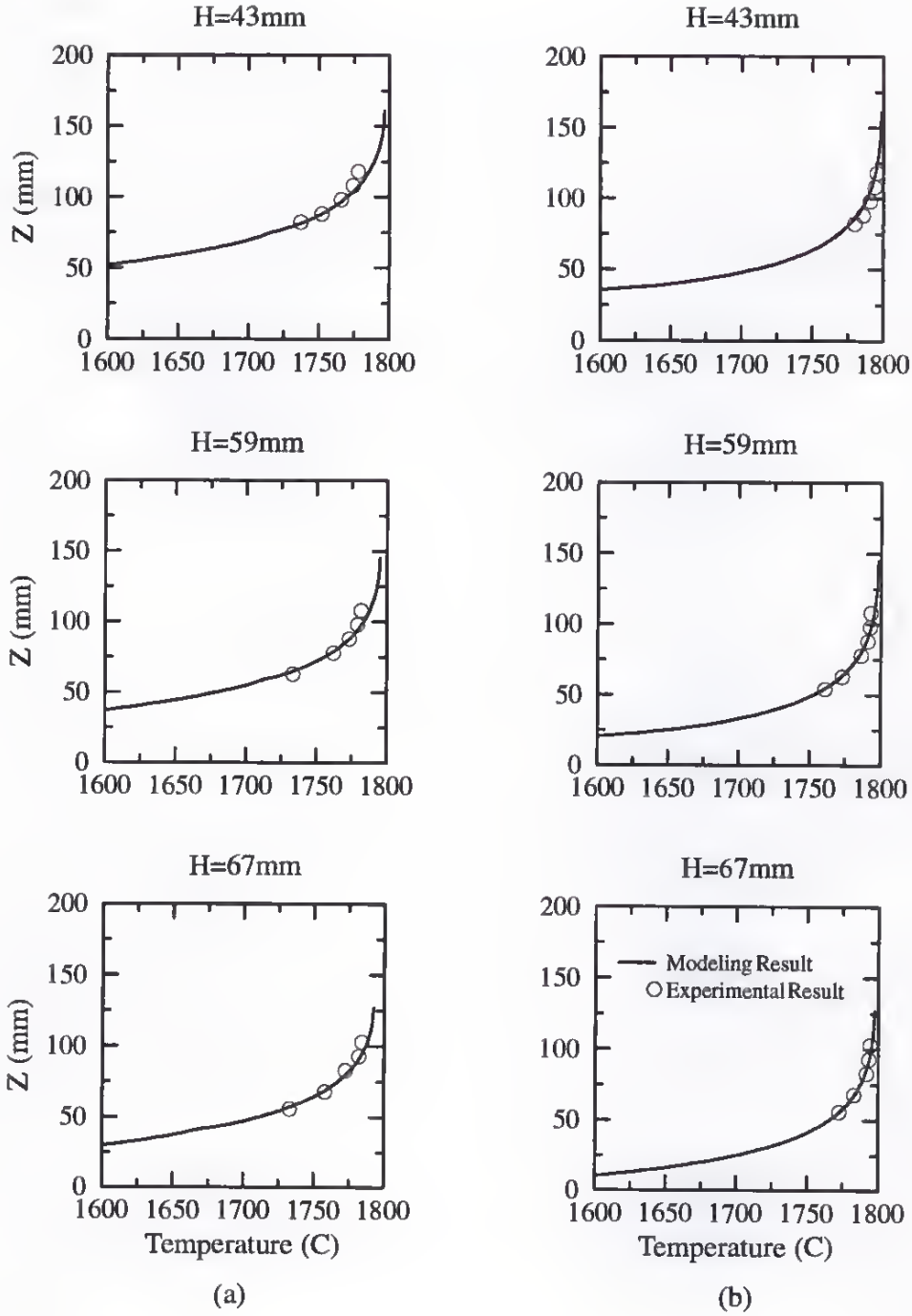

Figure 3.11. Comparisons of temperature profiles along (a) the NiAl centerline and (b) the ampoule outer wall between the modeling result and the experimental data for the three higher ampoule positions of H=43mm, H=59mm and H=67mm.

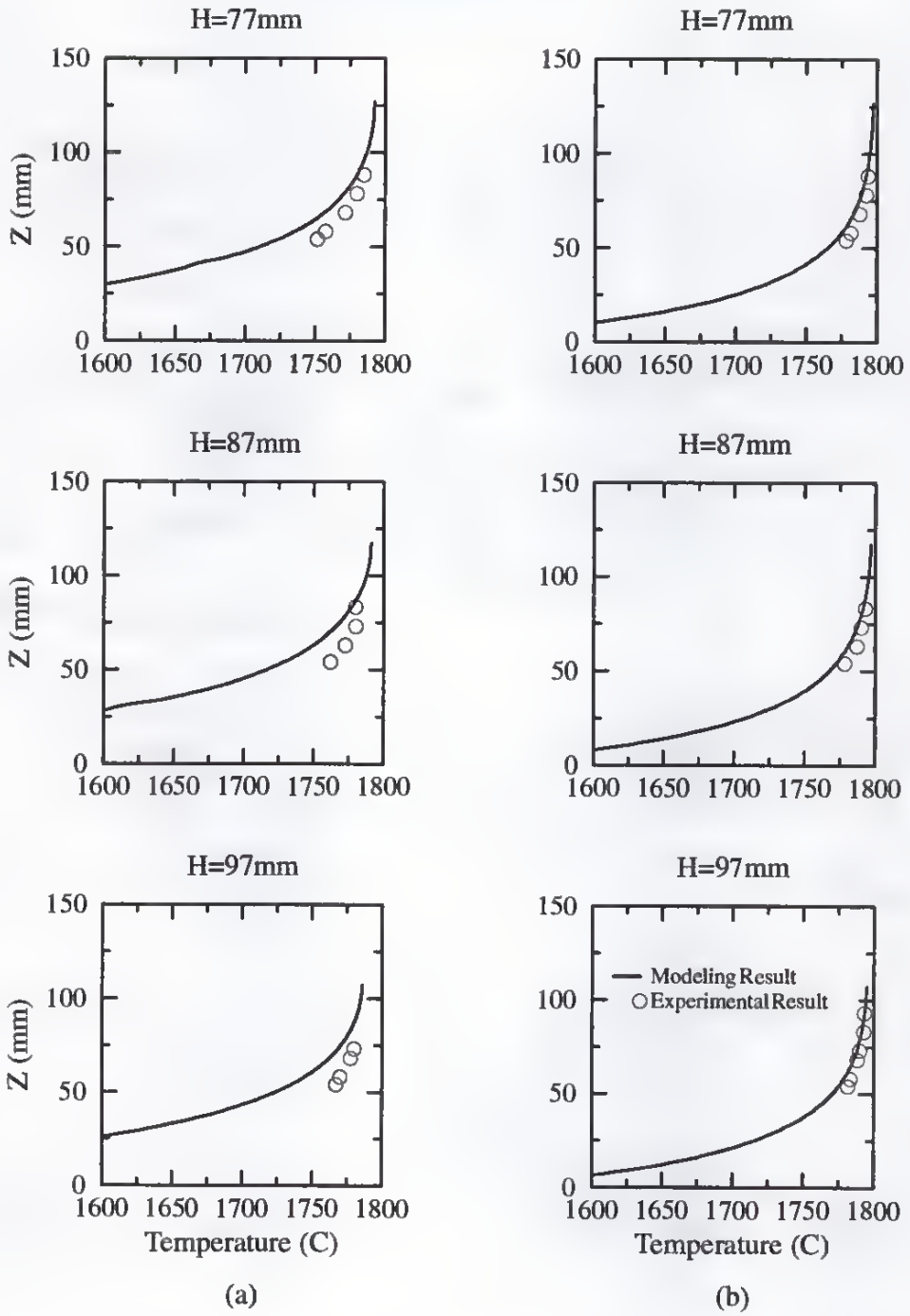

Figure 3.12. Comparisons of temperature profiles along (a) the NiAl centerline and (b) the ampoule outer wall between the modeling result and the experimental data for the three lower ampoule positions of H=77mm, H=87mm and H=97mm.

of H=43mm, H=59mm and H=67mm, but worsens for the three lower ampoule positions. This trend is explained in more detail below.

Figure 3.13 shows the streamfunctions and isotherm distributions for two selected ampoule positions, one at a higher location (H=43mm) and the other at a lower location (H=87mm). For the higher ampoule position, Fig. 3.13a shows that the ampoule base region is contained inside the furnace hot zone. Since the treatment of radiation heat transfer and boundary conditions appear reasonable there, the computed thermal distribution of this region is also accurate. Accordingly, the predicted temperature profiles along the NiAl centerline matches very well with experimental results. At the lower ampoule position, Fig. 3.13b shows clearly that the ampoule base region has been pulled out of the furnace hot zone. In this case, since the boundary condition at the outer wall of this region is still specified as a constant heat flux, this is no longer accurate. Furthermore, as the thermal distribution inside the ampoule is very sensitive to the isotherm change near the ampoule base, it is not surprising to observe in Fig. 3.12 the deviations between numerical results and experimental data along the NiAl centerline exist. Improvement of the modeling accuracy can be obtained by specifying realistic boundary condition at the outer ampoule wall as it is pulled out of the furnace. The temperature distribution along the ampoule outer wall in the furnace hot zone, though, is not influenced by this effect.

(ii) Melting temperature of β–NiAl

The melting temperature of NiAl at stoichiometric composition is reported in the literature as $Tmelt = 1638C$ (Noebe et al. 1993, Vedula et al. 1985). However, the accuracy of this value seems questionable. Based on the current experiment data and corresponding modeling results, we conducted an evaluation of the NiAl melting temperature of β–NiAl.

For the ampoule position of H=43mm, we measured the interface position by moving the alumina tube through the NiAl melt until it touched the solid/melt interface, which was found to be $h_{interf} = 75mm$. It is noted that, since the tip of TC1 is separated from the

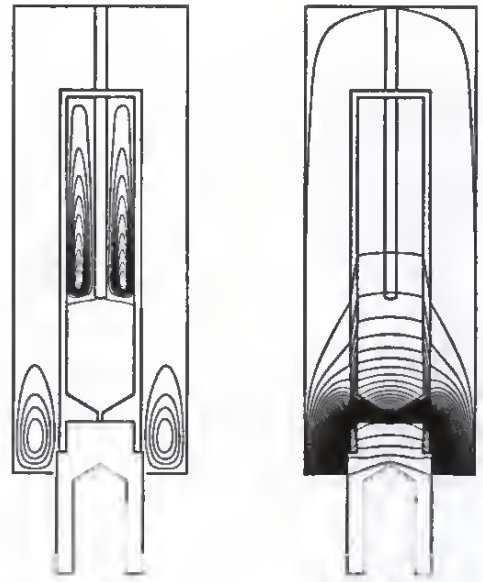

(a) H=43mm

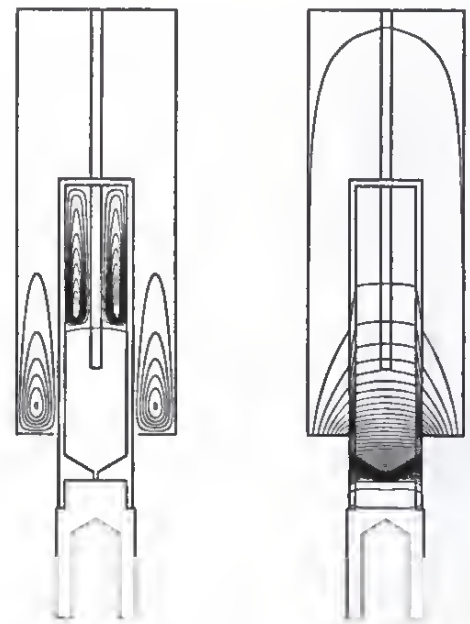

(b) H=87mm

Figure 3.13. Solution characteristics of NiAl furnace for selected ampoule positions of (a) H=43mm and (b) H=87mm.

interface by the closed end of the alumina tube (with a thickness of 6.5 mm shown in Fig. 3.8), the temperature reading of TC1 is not the melt/solid interface temperature. However, the detailed temperature profile along the entire ampoule centerline can be obtained from our numerical results. Combining these two results, the interface temperature of NiAl can be determined by interpolation, as shown in Fig. 3.14, yielding $T_{interf} = 1716C$. This result is surprising, as this value is at least 70 C higher than the melting temperature of NiAl widely reported in the literature. Waltson and Darolia (1995) have also reported recently an observation of NiAl melting temperature as high as 1682 C. Although *Tmelt* could not be determined directly in this study, the above estimation has its base. First, the current numerical model correlates well to experimental data; hence the temperature profile we used for interpolating the interface temperature is likely to be accurate. Second, thermocouples have been calibrated before the experiment. Although it has to be kept in mind that type C thermocouple does have a confident limit up to 1% and possibly brings in about 18 C difference in the current temperature measurement, this will not influence our current comparison between experimental results and numerical predictions. Third, the interface position is measured twice, i.e. during the experiment and after the experiment, with a confidence limit of ± 2 mm. Considering all possible errors that might arise during the

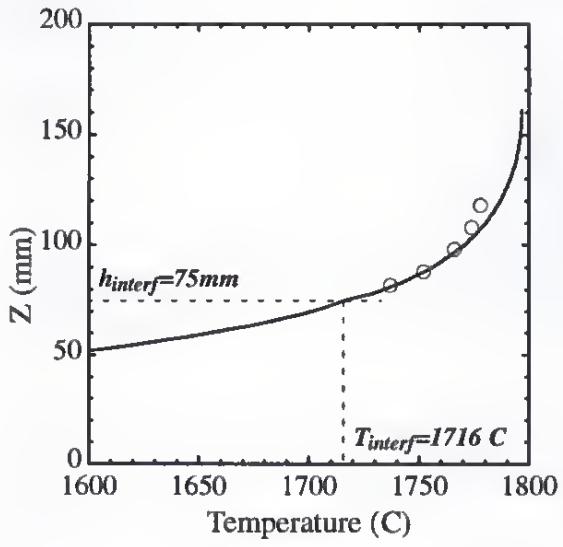

Figure 3.14. The estimation of melt/solid interface temperature of β–NiAl.

measurements of temperature and position, the melt/solid interface temperature we obtained for the current NiAl sample at stoichiometric composition from this study is still much higher than 1638 C.

3.2.4 Detailed Analysis of Processing Conditions

β–NiAl with high purity and improved mechanical property of high tensile elongation at room temperature has been produced routinely with the current design of the vertical Bridgman system (Levit et al. 1996). Therefore, it is valuable to describe the detailed characteristics of the processing conditions that are suitable for growing high quality single crystal NiAl. Furthermore, we will also provide suggestions for the improved design via numerical simulation with variations in selected furnace parameters.

3.2.4.1 Simulation of actual vertical Bridgman growth system

Satisfactory comparison between experimental and numerical results are obtained for the ampoule positions of H=43mm, H=59mm and H=67mm. Solution characteristics of the ampoule at these positions are further investigated for the current analysis. In this case, the alumina tube is not considered, since it was installed only for temperature measurement and would not exist in the actual Bridgman system.

Figure 3.15 shows the solution characteristics of the streamfunction and isotherm obtained for different H values. It can be observed that the streamfunctions in the melt share a very similar pattern for all positions, and the maximum velocity varies only slightly from 1.06 mm/s to 1.04 mm/s. The streamfunction patterns in the encapsulated argon gas change more noticeably, but the maximum velocity there is at least one or two orders of magnitude smaller than that in the NiAl melt due to the much smaller gas density. It appears that convection effects in the current crystal growth system are not strong. This is a desirable condition, for otherwise isotherms can be greatly distorted by convection which will cause nonuniform thermal conditions across the interface.

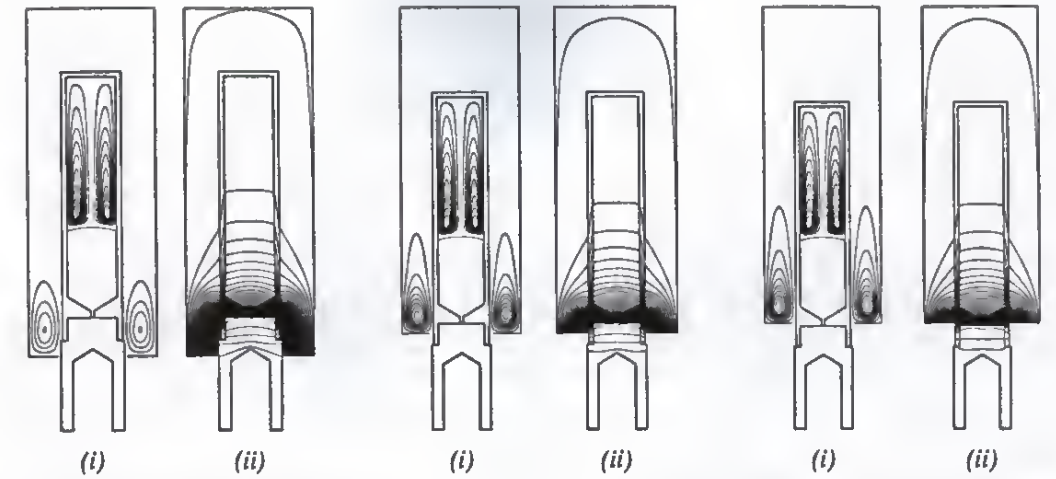

Figure 3.15. Solution characteristics of (i) streamfunctions and (ii) isotherm in a actual vertical Bridgman growth system for NiAl crystal for different ampoule positions. (a) H=43mm, (b) H=59mm and (c) H=67mm.

† *Streamfunctions inside encapsulated argon gas and inside the NiAl melt are not drawn by the same scales.*

It has been recognized in the literature that, for crystal growth from the melt in the vertical Bridgman growth system, a slightly convex (toward the melt) liquid–solid interface is favorable for grain selection and helps to prevent spontaneous nucleation at the ampoule wall. In addition, high temperature gradients across the interface and uniform distributions of thermal conditions along the interface are desirable for obtaining high purity crystals (Sen et al. 1988, Brown 1988, Kurz and Fisher 1989). In the following, these parameters as related to the current system are further discussed.

Figure 3.16 shows the interface shape and the vertical temperature gradient across the interface for different H values. It is observed that the interface shapes obtained from all three ampoule positions share a very similar convex pattern and develop parallel with each other. The difference between the centerline and inner ampoule wall locations is about 2mm. A similar feature is also observed for the temperature gradient across the interface as shown in Fig. 3.16b. For different ampoule positions, the gradients are all maintained in the range

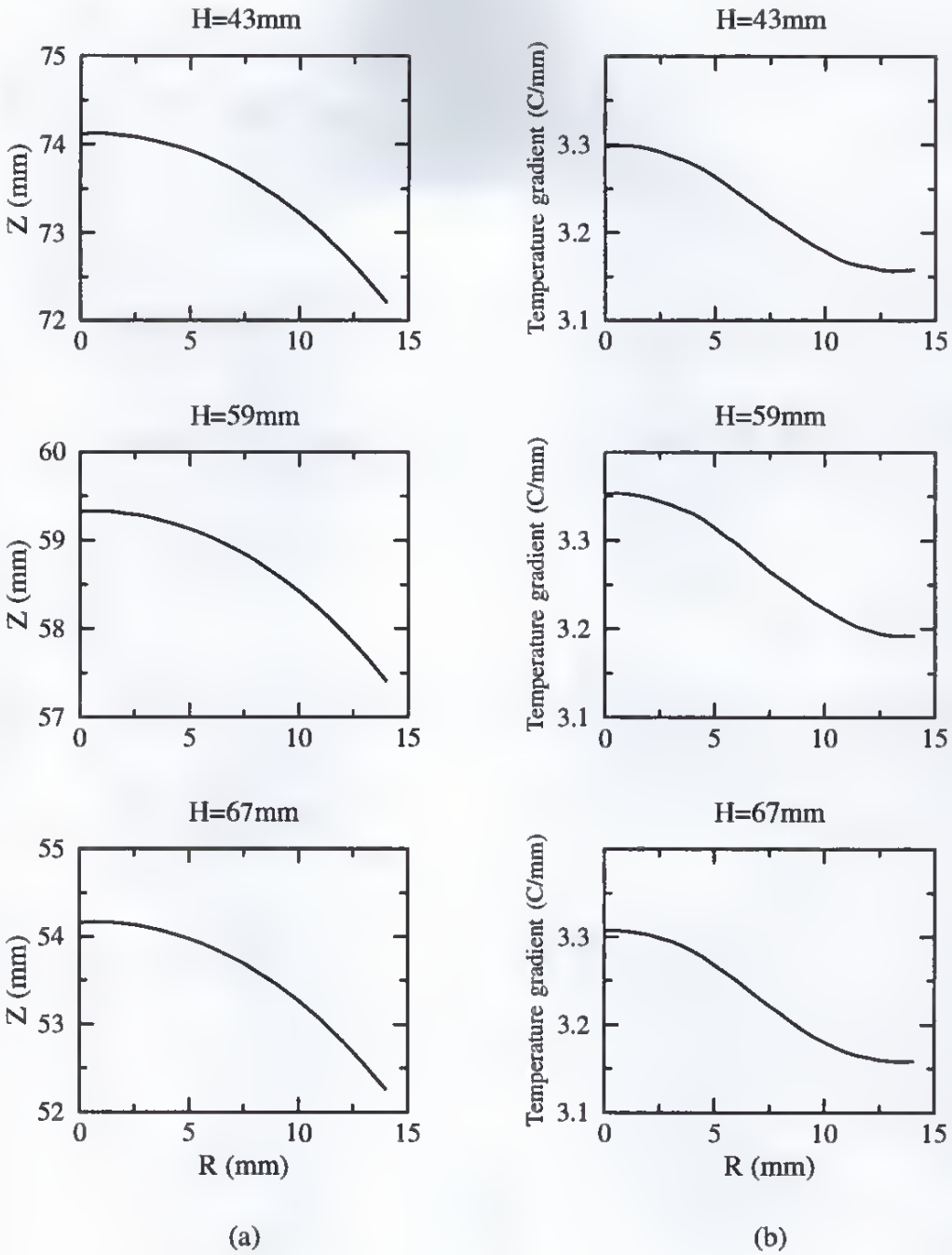

Figure 3.16. (a) Interface characteristics and (b) vertical temperature gradient across the interface for three ampoule positions of H=43mm, H=59mm and H=67mm.

of 3.16~3.35 C/mm and are quite stable. However, the gradient distribution along the interface is not uniform. The temperature gradient at the interface centerline is about 5% higher than that at the inner ampoule wall. This deviation is caused by the presence of convection effect in the melt. This phenomena indicates that a good furnace design should minimize the convection effect in order to maintain a uniform processing condition. Figure 3.17 explains this situation more clearly, in which the interface characteristics with convection effect and without convection effect are compared. It is observed that convection causes the interface position to be moved up about 0.5%, which is quite small. However, it causes the temperature gradient along the interface to deviate quite noticeably along the interface (5%), as is shown in Fig. 3.17b.

3.2.4.2 Suggestions for design improvement

In this section, we will vary design parameters with the goal of improving the processing conditions in the vertical Bridgman growth system. Since convection effects have been found insignificant, they are not included in order to save computational time.

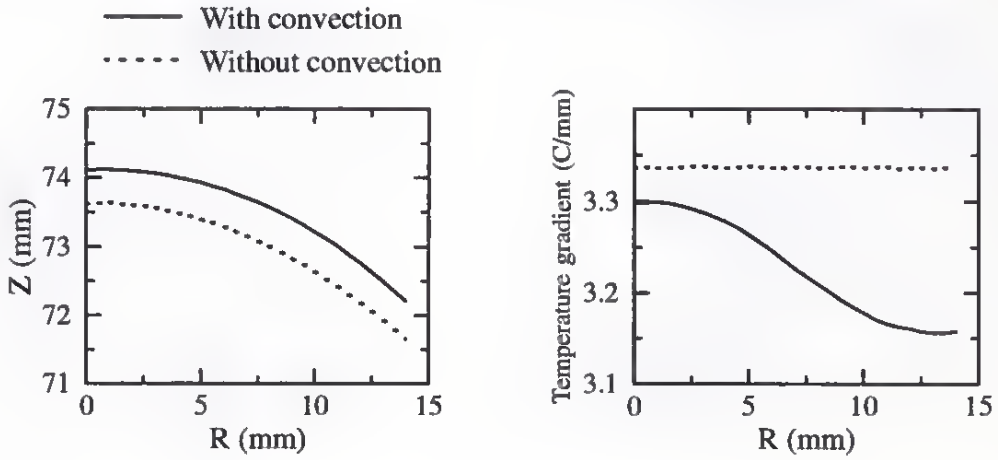

Figure 3.17. Comparison of (a) interface characteristics and (b) temperature gradient across the interface between solutions with convection and without convection effects for the ampoule position of H=43mm.

Parameters such as the ampoule emissivity, the geometry of the ampoule base, the thermal conductivity of the ram, and the ampoule wall thickness have been adjusted and their influence on the interface curvature, temperature gradient, etc., are compared. In the following, those cases that might lead to the improvement of the interface conditions are listed.

- Case 1: Use all parameters from the original design, i.e., the base case;
- Case 2: Increase the emissivity of the ampoule outer wall from 0.8 to 1.0. This can be achieved in reality by, for example, coating the alumina ampoule outer wall with high emissivity and high melting temperature materials;
- Case 3: Decrease the ampoule base angle from 120 degrees to 100 degrees, as shown in Fig. 3.8;
- Case 4: Use a higher thermal conductivity material for the chill ram. For example, replace copper by silver;
- Case 5: Decrease the ampoule outer diameter by 2 mm.

Figure 3.18 shows the interface characteristics from the variations of these parameters. It is observed that most of these variations can lead to certain increase of the temperature gradient, which is desirable. Especially for cases 2 and 5, i.e. the increase of emissivity of the ampoule outer wall and the decrease of the ampoule thickness, the increase of the temperature gradient is more prominent. However, the change of the ram material to one with a higher conductivity (Case 4) seems not to influence the interface conditions very much. It is interesting to observe that the interface curvature seems to be insensitive to all of these variations. This is seen in the parallel and convex shape interfaces that are obtained for all cases. The locations of the interface, though, were lowered for cases 2 and 5, moved higher for case 3, and remains nearly unchanged for case 4. It is desirable to further explore these factors by inspecting the quality of the crystal growth with these design modifications. There are also other possible variations of furnace design that might help to achieve an improved processing condition near the interface. For example, it is obvious that an increase of heater temperature of T4 or a decrease of the cooling temperature of T1 both help to

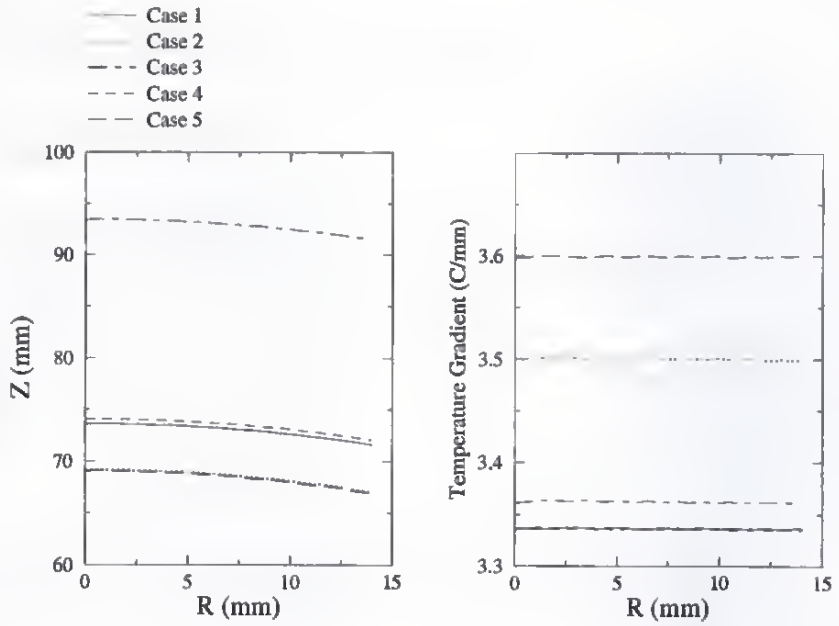

Figure 3.18. Effects of variations in processing parameters on the interface characteristics by solutions without convection. (a) Interface position and (b) Temperature gradient across the interface.

increase the temperature gradient inside the system, and an increase of the ampoule inner diameter helps to produce single crystal with larger size. However, care needs to be taken here because of the convection effect. It is observed from Fig. 3.17 that convection tends to cause the nonuniform distribution of temperature gradient along the interface, which is undesirable. Thus, any variations that might lead to the increase of convection effect should be made carefully.

3.3 Closure

In this chapter, we have systematically conducted a detailed analysis of thermal conditions in a vertical Bridgman growth system for the β–NiAl single crystal. In this system, there are strongly coupled effects of phase change, conduction, convection and radiation heat transfer, variable material properties as a function of temperature and complex

geometry and boundary conditions. Therefore, direct analysis of this system for optimizing the processing condition to control the crystal quality is challenging. However, through the coordinated computational and experimental study, we have been able to obtain satisfactory agreement of the temperature profiles along the NiAl centerline and the ampoule outer wall between the experimental measurements and the numerical predictions, which indicates that current model is accurate. It appears that the current design for the single crystal growth of β–NiAl is reasonable, evidenced by the interface shape and the temperature gradient across the interface.

Variations in processing parameters have also been explored for process improvement. For example, we have shown that coating the ampoule outer wall with a high emissivity material, or decreasing the ampoule wall thickness, will both lead to an improvement of the interface conditions. We have also found in this study that the melt/solid interface temperature of β–NiAl can be as high as about 1716 C, which is about 70 C higher than that reported in the literature. Because the high melting temperature of NiAl is one of its strongest attributes, the accurate definition of the melting temperature is important and is worthy of more effort in the future.

CHAPTER 4
MULTI–LEVEL SIMULATION OF VERTICAL BRIDGMAN GROWTH OF CdTe CRYSTAL

In this chapter, the numerical model we have developed in chapter 2 is applied to simulate the solidification process of CdTe crystal in two vertical Bridgman growth configurations. The model will account for the complex geometries of the entire growth system, the combined conduction, convection and radiation heat transfer, and the solidification dynamics in accordance with the scheduling of the thermal boundary condition. The sensitivities of the CdTe interface characteristics to the variations in boundary conditions, transport properties of CdTe (caused by phase change and temperature nonuniformity), and ampoule geometry will also be investigated.

4.1 Background

CdTe has certain properties which make it important and unique in several technological applications (Zanio 1978). For example, the combination of the high atomic number, wide bandgap, and good transport properties make it useful for room temperature gamma–ray and x–ray detectors. The high electro-optic coefficient combined with a low absorption coefficient makes it useful for electro-optic modulators. Low absorption from 1 to 30 mm makes it ideal for lenses, Brewster windows, partial reflectors, and fiber optics. Most importantly, CdTe and its solid solution systems (Cd, Zn)Te and Cd(Te, Se) are the most favored substrate materials for epitaxial deposition of the infrared detector material cadimium mercury telluride ($Hg_{1-x}Cd_xTe$) (Pfeiffer and Mühlberg 1992). At the present time, CdTe has not made as significant an impact as silicon because it is expensive and very difficult to grow. For example, its low thermal conductivity ($k \approx 1.5$ W/m K) makes the

temperature gradient very sensitive to minor variations in thermal condition within the system, and its low critical resolved shear stress (CRSS$\approx$0.5 x 10^{-3} dynes/$m^{2)}$ makes it very prone to formation of dislocations (Brown 1988).

The vertical Bridgman growth system has been widely used for producing single crystals of CdTe from the melt (Pfeiffer and Mühlberg 1992, Sen et al. 1988, Rudolph and Mühlberg 1993, Parfeniuk et al. 1992). To obtain high quality CdTe crystal within this system, thermal condition surrounding the melt/crystal interface is a main concern. Of particular interest to CdTe growth is that the interface can assume either concave or convex shapes, depending on many factors. These include the distribution and the scheduling of the overall temperature profile (Sen et al. 1988, Rudolph and Mühlberg 1993), the strong effect of temperature and phases on thermal conductivities (Pfeiffer and Mühlberg 1992), and the design of ampoule geometry and the selection of ampoule material (Koai et al. 1994, Brunet et al. 1993). Furthermore, the addition of a small quantity of cadmium to the starting stoichiometric melt composition, and a controlled overpressure of cadmium vapor appear to lower the content of precipitates, inclusions, and residual impurities of the grown CdTe crystal distinctly (Rudolph and Mühlberg 1993). Overall, it seems intuitively sensible to create a convex solid-melt interface so that the crystal tends to grow along an outward direction, producing a larger size of the single crystal in the middle of the ampoule. In this work we attempt to identify the factors responsible for directly affecting the solid–melt interface shape.

The crystal growth process of the vertical Bridgman system in configurations considered is controlled by translating the system downwards. Figures 4.1 and 4.2 show the schematic of two designs, along with the thermal boundary conditions imposed during the growth of CdTe. Both systems are axisymmetric and are composed of two parts:

1 Enclosure wall, made of mullite or quartz and the encapsulated argon gas or air;

2 The quartz ampoule containing seedless CdTe melt and crystal.

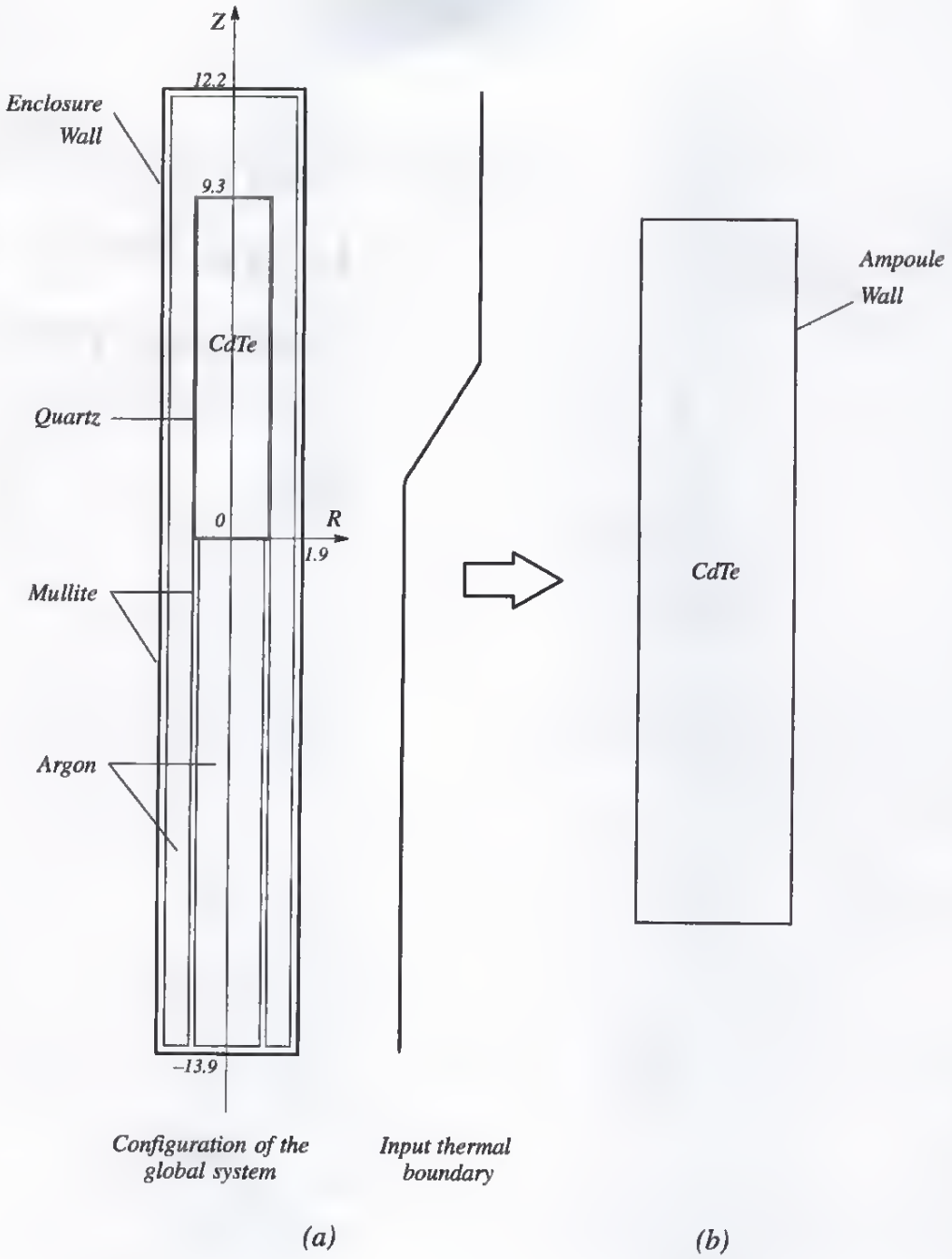

Figure 4.1. Schematic of a flat base vertical Bridgman growth system for growing CdTe. (a) Configuration of the global system and the input thermal boundary. (b) Configuration of the refined ampoule region.

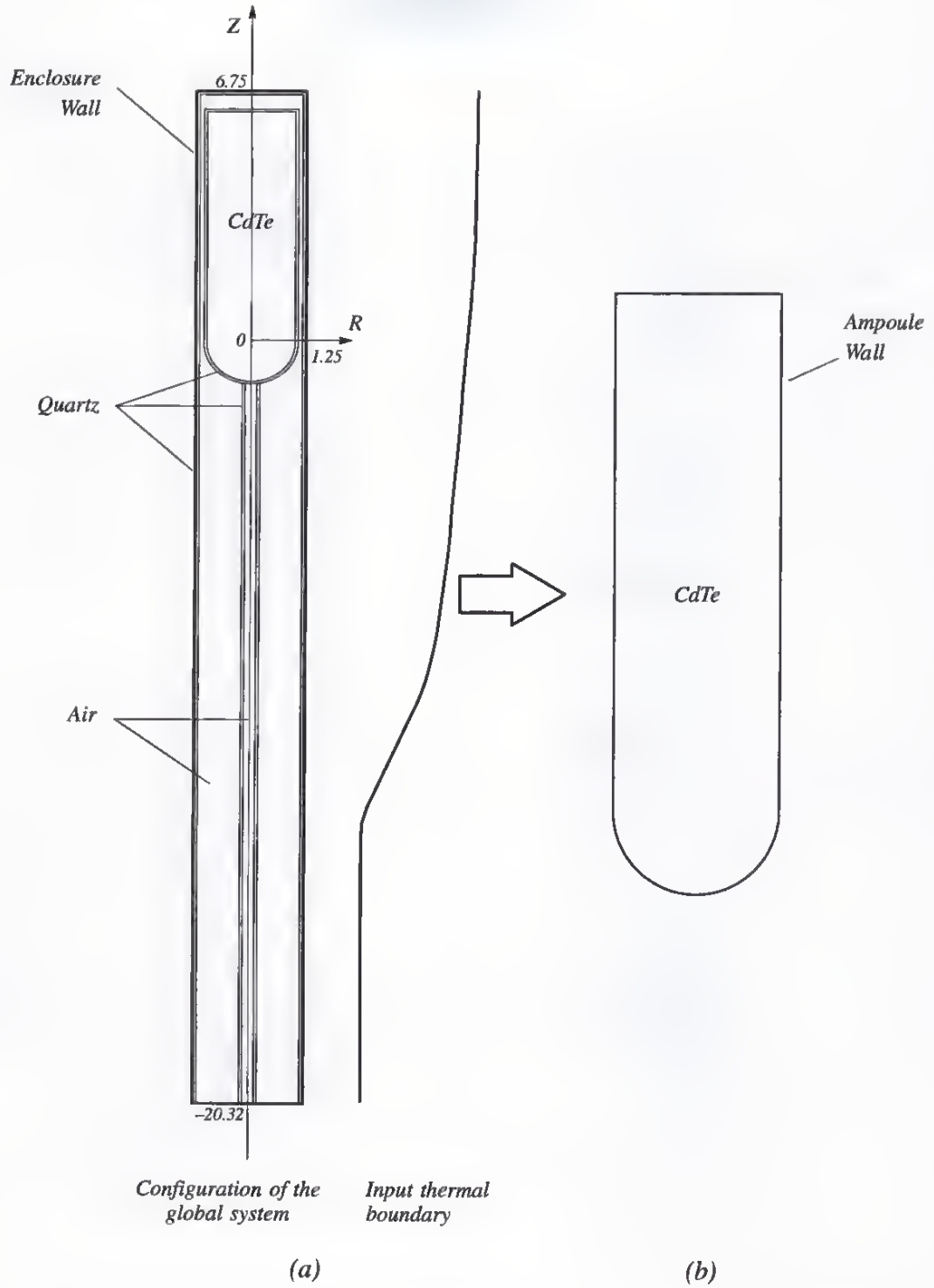

Figure 4.2. Schematic of a semi–spherical base vertical Bridgman growth system for growing CdTe. (a) Configuration of the global system and the input thermal boundary. (b) Configuration of the refined ampoule.

The main difference between the two configurations is the ampoule geometries, one having a flat base and the other a semi–spherical base. The gap between the enclosure and ampoule walls in the flat base system is wider than that in the semi–spherical base system. Accordingly, the heat input profiles in the two systems are different as shown schematically in Fig. 4.1 and Fig. 4.2 and quantitatively in Fig. 4.3. These differences reflect the current industrial practices and a possible design change; hence the two configurations considered here are realistic. Our interest is to simulate and analyze the crystal growth processes in both configurations.

Different system designs will lead to different thermal environment and interface characteristics. Nevertheless, the following physical phenomena are of key importance in

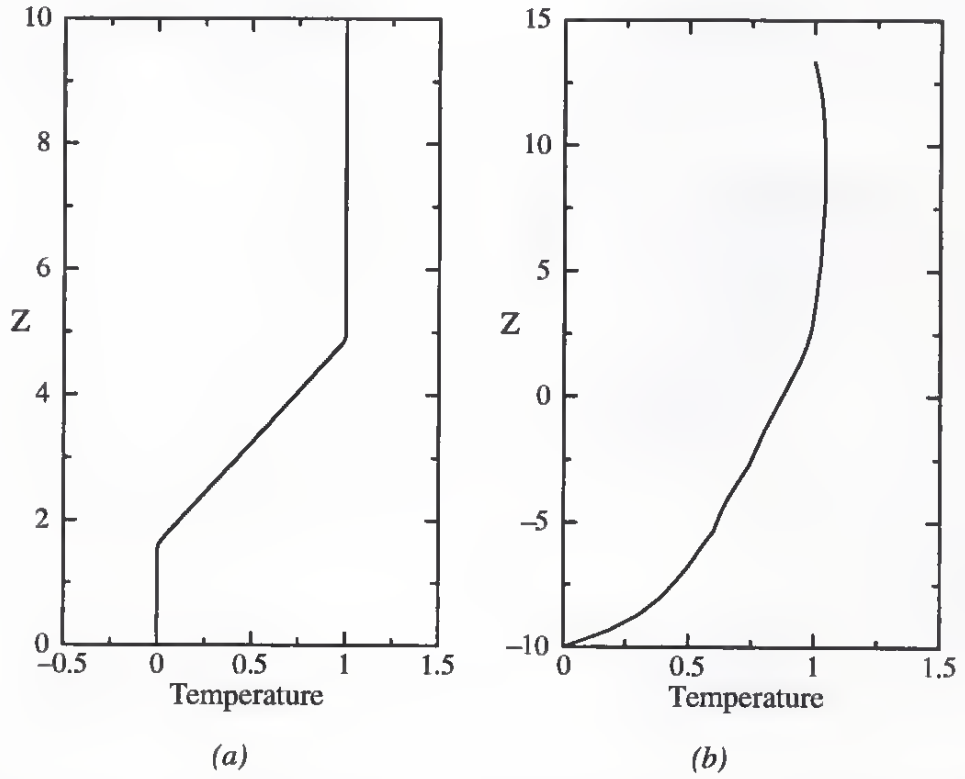

Figure 4.3. Distributions of thermal boundaries along the outer vertical wall of the enclosure for (a) the flat base system, where the nondimensionlized melting temperature is 0.75, and (b) the semi–spherical base system, where the nondimensionlized melting temperature is 0.921.

both configurations and is similar to that of the vertical Bridgman system for growing NiAl crystal.

- Phase change within the ampoule;
- Heat conduction within the quartz/mullite enclosure and the support;
- Convection in the melt and in the encapsulated gas;
- Radiation between the enclosure wall and the ampoule wall.

For the present effort, only the pure CdTe is considered to maintain a reasonable scope. Materials properties of different components in the two configurations of CdTe systems are listed in Table 4.1.

Table 4.1 Material properties of CdTe systems

Material	ϱ (kg/m^3)	μ (kg/m–s)	k (W/m–K)	C_p (J/kg–K)	β (K^{-1})	ε
CdTe	5680	2.49x10^{-3}	1.5(s) 3.0(l)	160.(s) 187.(l)	5.x10^{-4}	0.5
Air	1.2928 (0 C 1atm)	4.73x10^{-5} (1200 K)	7.83x10^{-2} (1200 K)	1175 (1200 K)	8.33x10^{-4} (1200 K)	
Argon	0.487	5.42x10^{-5}	4.27x10^{-2}	520	8.33x10^{-4}	
Quartz	2649.	†	4.82	–	–	0.8

† Assigned big values
Latent heat = 209.2 J/g

4.2 Numerical Solutions of CdTe System

Two ampoule configurations, namely, the flat base system and the semi–spherical base system have been investigated in the present study. Steady state calculations are conducted based on the aforementioned two–level approach. Based on the refined model at the ampoule scale, we have further investigated the interplay of the transport properties of CdTe, especially its low thermal conductivity and the effects of the thermal boundary condition on growth dynamics. The parameters chosen in the present work are Ra_0=1.0x10^5, Pr_0=0.4, and St_0=0.2. A major aspect of CdTe is that the thermal conductivity of the melt is twice as

large as that of the solid, i.e. $k_l=2k_s$. This aspect is investigated. The relative merits of the flat base and semi–spherical base in producing desirable solid–melt interface characteristics are also compared qualitatively.

Figure 4.4 shows portions of the global body–fitted grid distributions around the ampoule regions for both the flat base and the semi–spherical systems. For the refined model, the grids within the ampoules are increased to 161x101 nodes from 31x101 nodes used by the global model for the flat base system, and to 121x219 from 61x110 for the semi–spherical system.

4.2.1 The Flat Base System

In this design, a given temperature profile is imposed on the outer vertical wall of the enclosure, which is shown in Fig. 4.1a and Fig. 4.3a where $z=0$ is defined at the flat base of ampoule.

Figures 4.5a and b present, respectively, the solution characteristics obtained by the global model and the refined model. In both cases, the predicted convection strength and pattern have similar feature with the refined model capturing two additional recirculation cells near the top region. The isotherm distributions obtained by both models are close; the difference in the interface position predicted by the global and the refined models at the ampoule center is only about 0.3%. This agreement indicates that accurate solutions have been obtained with the present boundary condition and transport properties.

To shed light on the influence of the variations in thermal boundary conditions on solidification dynamics, a simulation is conducted by directly applying the boundary condition employed by the global model on the ampoule vertical wall. This exercise amounts to ignoring the influence of radiation heat transfer between the enclosure and the ampoule, and ignoring the convection heat transfer of the encapsulated argon gas. Figure 4.6 shows the thermal profiles of that imposed by the external boundary condition and that deduced from the global model. It is observed that a smeared profile is obtained as a result

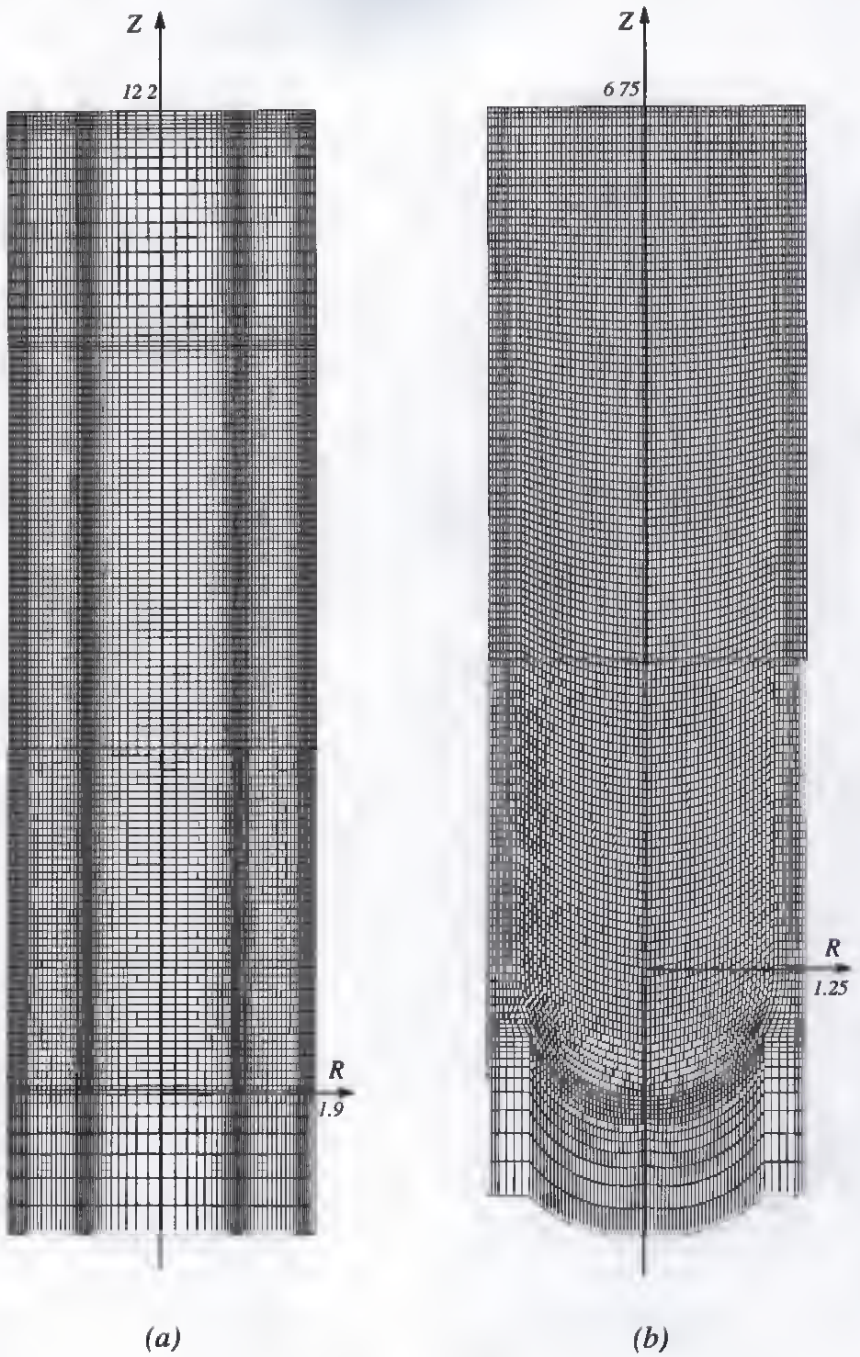

Figure 4.4. Global grid distributions around the ampoule regions for (a) the flat base system with a total grid size of 79x167 and 31x101 in the ampoule region, and (b) the semi–spherical system with a total grid size of 79x175 and 61x110 in the ampoule region.

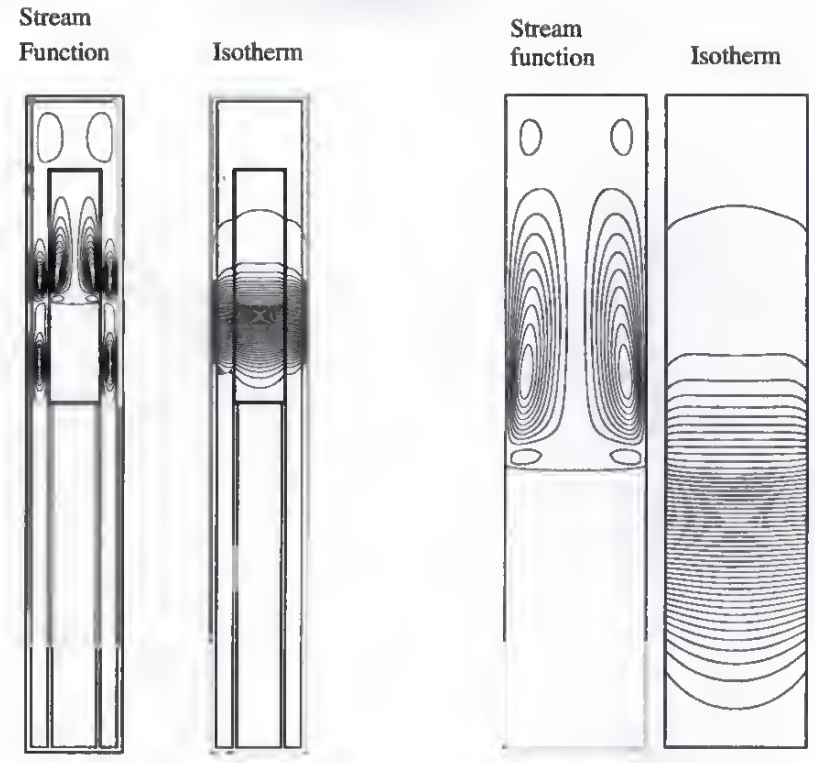

Figure 4.5. Solution characteristics of the flat base system for (a) the global model (Grid size=79x167 with 31x101 in the ampoule region) and (b) the refined model (Grid size=161x101). $Ra_0=10^5$, $Pr_0=0.4$, $St_0=0.2$, and $k_l=2k_s$

† *Streamfunctions inside argon and inside CdTe melt are not drawn by the same scales.*

of the diffusive effect of the encapsulated argon gas, the conduction through the enclosure and the ampoule walls, and the radiation heat transfer between them; however, the two thermal profiles are largely consistent.

Figure 4.7 shows the streamline and isotherm distributions of this calculation. It is found that even though the two boundary conditions differ only in a seemingly modest manner, significant changes in solution characteristics appear. In Fig. 4.7, the main convection cells are of smaller size while the value of the maximum streamfunction is doubled. These changes are apparently caused by the sharper temperature profile directly imposed on the ampoule wall.

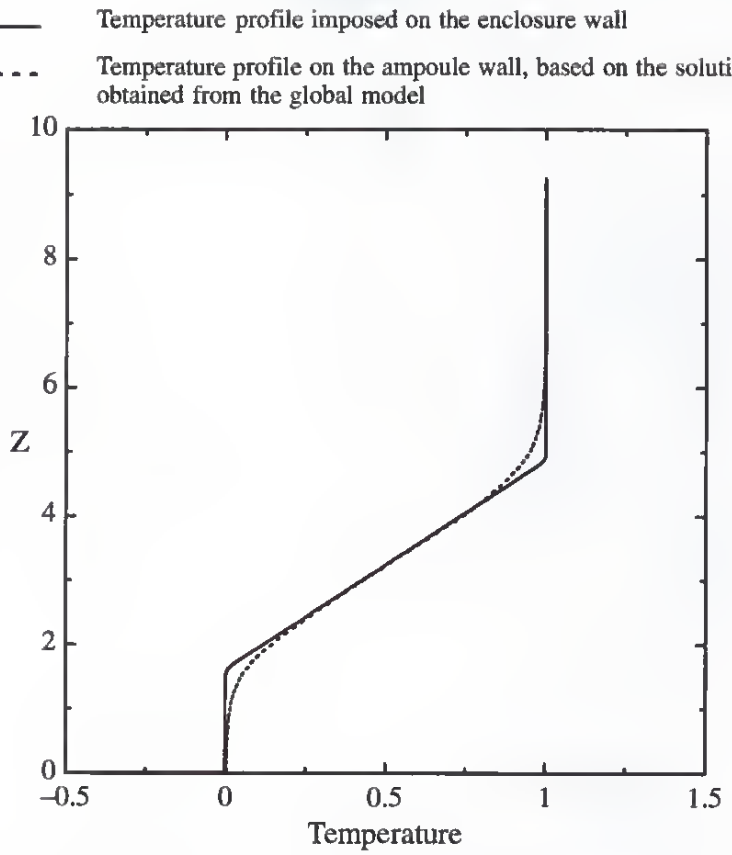

Figure 4.6. Comparison of the temperature profiles on the enclosure wall and on the ampoule wall.

Figure 4.8 compares in detail the change of the solid–melt interface position and curvature as a result of this minor variation of thermal boundary condition. Elevated interface position at the ampoule wall and a more concave interface shape are observed. Based on the results shown in Figs. 4.7 and 4.8 it is clear that in order to faithfully simulate the growth process one must accurately supply the thermal boundary condition for the ampoule region. Hence, the entire furnace needs to be considered.

In addition, to investigate the effect of the variation in thermal conductivities of CdTe between melt and crystal on the interface curvature, we present in Fig. 4.9 the refined ampoule solutions with a constant conductivity, i.e. $k_l=k_s$. Figure 4.10 presents the comparison of the interface shapes and locations. It is striking to observe that the interface shape changes from concave to convex due to the change in the thermal conductivity. While

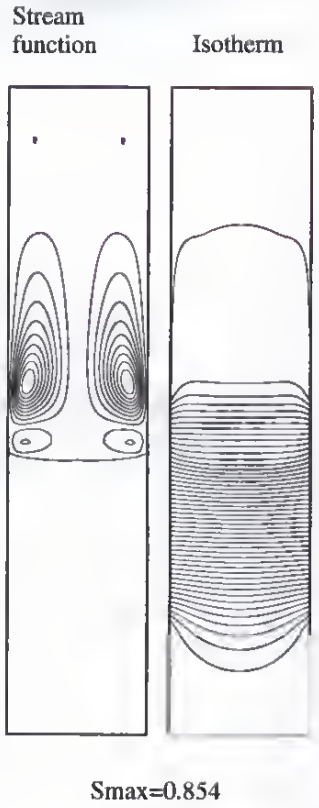

Figure 4.7. Solution characteristics of the refined model with direct application of the enclosure thermal condition, i.e., by neglecting the heat transfer between enclosure and ampoule walls. $Ra_0=10^5$, $Pr_0=0.4$, $St_0=0.2$, and $k_l=2k_s$

the comparison between Fig. 4.5b and Fig. 4.9 shows that the main convective pattern in the melt is largely unchanged, the two smaller cells near the interface region observed with $k_l=2k_s$ no longer exist with $k_l=k_s$.

4.2.2 The Semi–Spherical Base System

In this design, the thermal boundary condition applied on the outer vertical enclosure wall is shown in Fig. 4.3b.

Figures 4.11a and b show, respectively, the streamfunction and isotherm distributions predicted by the global model and the refined model. Almost identical distributions of streamfunction and isotherm within the ampoule region are obtained by both models, again indicating that grid independent solutions have been reached.

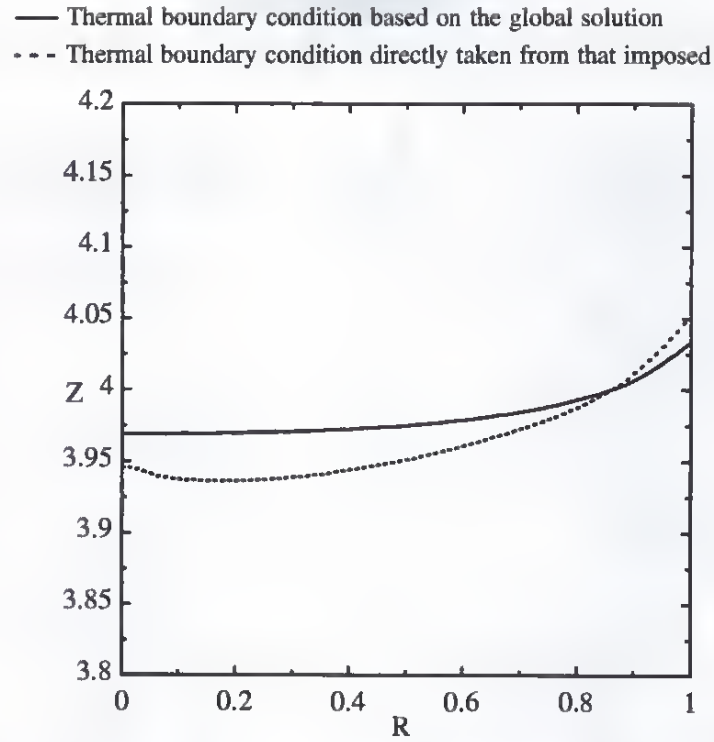

Figure 4.8. Effect of thermal boundary conditions on the solid–melt interface characteristics of the flat base system.

To show the impact of the ampoule configuration on interface characteristics, Figure 4.12 compares the interface curvature obtained by the flat base system and by the semi–spherical base system by imposing their locations on the wall together. This comparison shows that a concave interface appears in both systems. Despite the dramatic change in ampoule geometries, the change of the interface curvature is rather small. The difference of the interface position at the ampoule center is only about 5%. Thus at this point, no obvious improvement of one system over the other is achieved by changing the ampoule geometry.

By comparing the streamfunctions and the isotherms in Fig. 4.5 and Fig. 4.11, it is observed that in both systems minor cells appear in the region close to the interface due to the concave shape of the interface. Nevertheless, the main convection cells assume very different shapes and strengths between the two systems. In Fig. 4.11, the convection cells

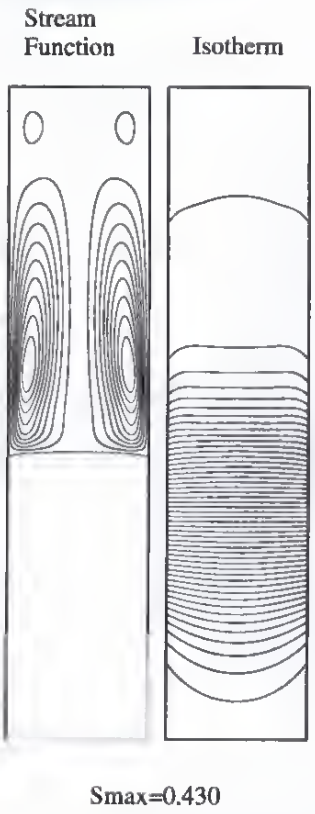

Figure 4.9. Solution characteristics of the refined model with constant thermal conductivity of CdTe, i.e. $k_l=k_s$. $Ra_0=10^5$, $Pr_0=0.4$, and $St_0=0.2$

are more stretched over the whole melt domain and their magnitudes are smaller. Since the thermal boundary conditions of the two systems are different in that one changes abruptly and the other varies smoothly, these changes are not surprising. However, the change in the main convection characteristics does not seem to substantially influence the interface curvature.

4.3 Closure

In this chapter, numerical simulation has been carried out for the single crystal growth of CdTe in two vertical Bridgman crystal growth configurations. It is found that both the flat base and the semi–spherical base system produce slightly concave solid–melt interface which is less than desirable. However, the curvature of the melt/crystal interface seems to

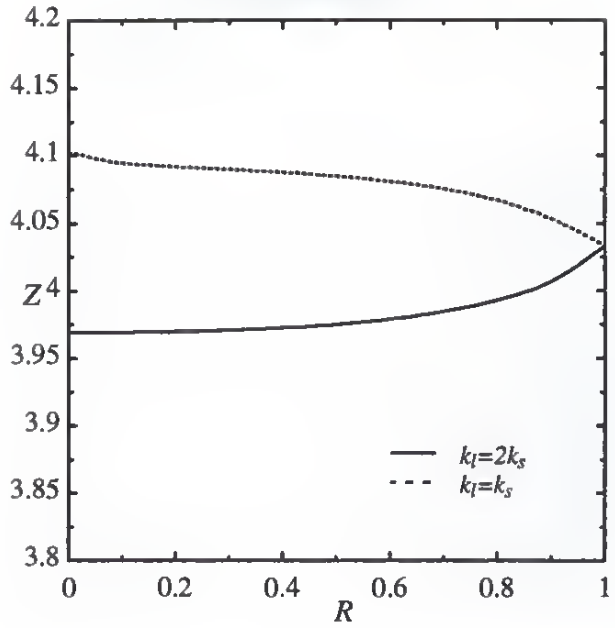

Figure 4.10. Effect of conductivity on the interface characteristics.

depend strongly on the variations in thermal conductivities. Furthermore, it is also observed that the thermal boundary condition plays a very critical role in determining the solidification characteristics. Accordingly, in order to accurately simulate the crystal growth process, temperature profile on the ampoule wall must be actually determined, which, in turn, indicates that heat transfer surrounding the ampoule should be carefully accounted for.

In the following two chapters, our emphasis will be directed toward the physical modeling and numerical implementations of alloy solidification. A distinct difference between single crystal growth and alloy solidification is that alloy solidifies over a range of temperature depending on different compositions. Therefore, species transport and the interactions between formations of microscopic structure and macroscopic processing conditions, which have not become issues for the previous modeling and simulation of the single crystal growth systems of NiAl and CdTe, will then need to be considered carefully.

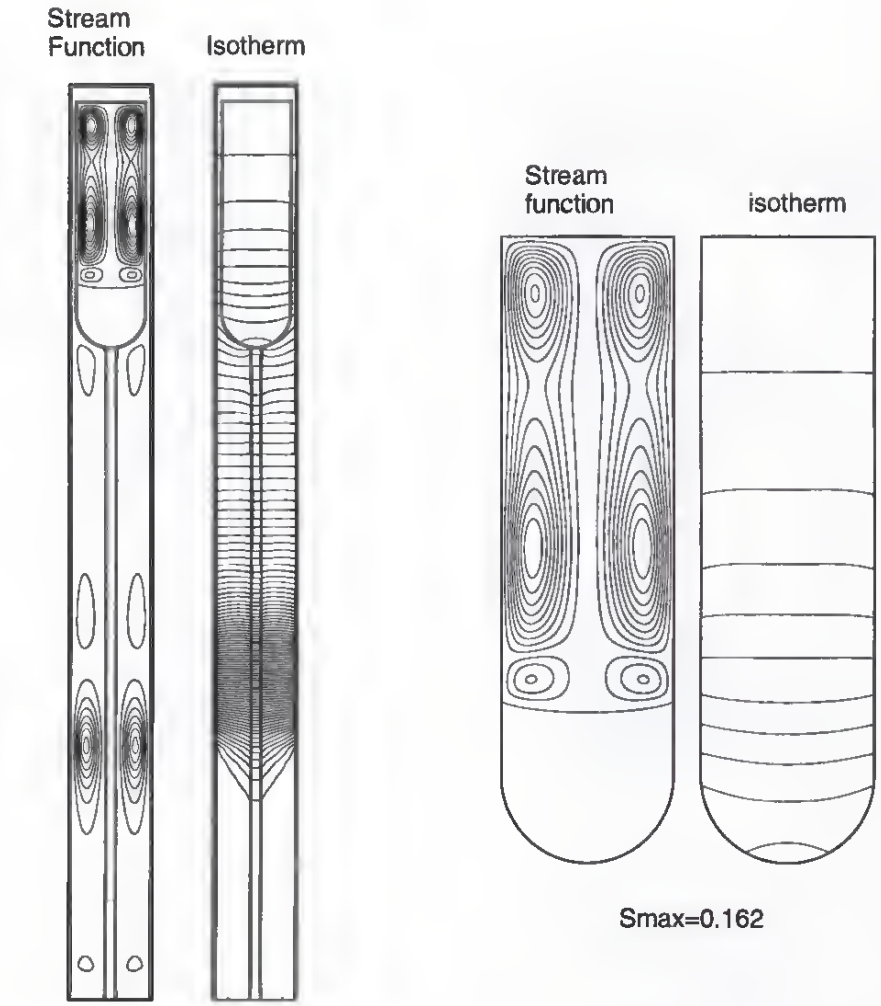

Figure 4.11. Solution characteristics of the simulation of the semi–spherical base system from (a) the global model (Grid size=79x175 with 61x110 in the ampoule region) and (b) the refined model (Grid size=121x219). $Ra_0=10^5$, $Pr_0=0.4$, $St_0=0.2$, and $k_l=2k_s$

† *Streamfunctions inside air and inside CdTe melt are not drawn by the same scales.*

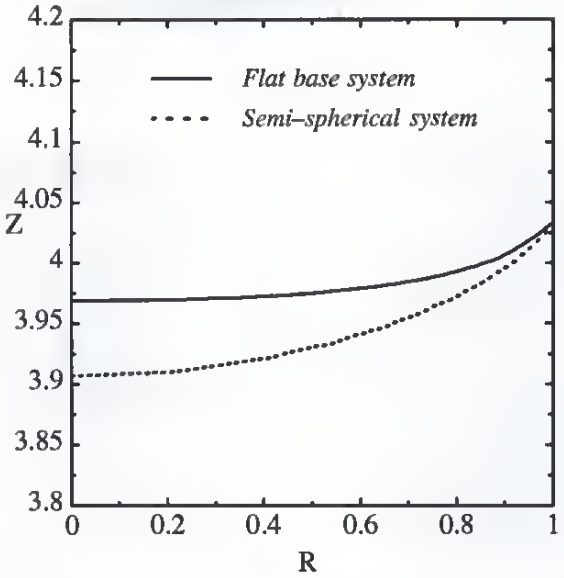

Figure 4.12. Comparison of interface shapes between the flat base system and the semi–spherical base system, where same location at the ampoule wall has been imposed. The actual interface location of the semi–spherical system at ampoule wall is z=0.86.

CHAPTER 5
FORMULATION OF MACROSCOPIC TRANSPORT EQUATIONS FOR ALLOY SOLIDIFICATION

The concept of the macroscopic formulation of transport equations has its roots in the analysis of multiphase flow, encountered in a wide variety of engineering problems involving porous media, particle suspensions, solute sedimentation, energy conversion, chemical reaction, etc. Of these applications, the study of macroscopic momentum transport in porous media has received much attention. Theoretical analysis and experimental verification on this topic is abundant in literature (Drew 1983, Whitaker 1967, Slattery 1967, Ghaddar 1995).

In materials solidification, the transport phenomena of mass, momentum as well as energy and species are all important, hence their combined effects have to be considered. In this chapter, the detailed derivation of the macroscopic transport equations of mass, momentum, energy and species within the context of the solidification process is reviewed and presented in a rigorous and systematic way. Some issues that are neglected by other researchers in the area of solidification modeling, e.g., Beckermann and Viskanta(1993), Ganesan and Poirier (1990), are also discussed. Since macroscopic transport equations are derived upon the classical microscopic transport equations, a brief discussion of the microscopic equations is presented below.

5.1 Microscopic Transport Equations

Solid, liquid or gas is composed of distinct molecules or atoms. However, in many of engineering models materials are conveniently treated as continuous media instead of individual molecules or atoms. This is because engineers are mostly concerned about the

averaged features of materials, represented by such quantities as density, velocity, pressure, temperature, etc., which vary continuously in space and time. For example, density is defined in continuum by

$$\varrho = \lim_{\Delta V \to 0} \frac{\Delta M}{\Delta V} \tag{5.1}$$

where ΔV is an infinitesimal volume and ΔM is the mass contained in ΔV. Physically, ΔV cannot be allowed to shrink to zero, since if ΔV has a characteristic size so comparable to the length of molecular free path, ΔM would vary discontinuously, depending on the number of molecules in ΔV. In order for continuum mechanics to hold, the lower limit of ΔV should be selected to some finite (but small) value ε in order to eliminate molecular effects. Transport equations based on this hypothesis are referred microscopic transport equations.

According to Reynolds' transport theorem (Malvern 1969), the general form of microscopic transport equations of certain quantity Φ can be rigorously derived from conservation laws and is given by,

$$\frac{\partial \Phi}{\partial t} + \nabla \cdot (\Phi V) = \nabla J + S \tag{5.2}$$

where Φ represents mass ϱ, momentum ϱV, enthalpy ϱH or species concentration ϱC; J is a tensor of order one greater than that of Φ and accounts for the diffusive effect of momentum, heat, or species; and S is a source term. Neglecting viscous heat dissipation, compression work, volumetric energy and species sources, which is appropriate for many practical solidification systems, the microscopic transport equations of mass, momentum, energy and species are

$$\frac{\partial \varrho}{\partial t} + \nabla \cdot (\varrho V) = 0 \tag{5.3}$$

$$\frac{\partial \varrho V}{\partial t} + \nabla \cdot (\varrho VV) = \nabla \cdot \sigma + b \tag{5.4}$$

$$\frac{\partial \varrho H}{\partial t} + \nabla \cdot (\varrho HV) = -\nabla q \tag{5.5}$$

$$\frac{\partial \varrho C}{\partial t} + \nabla \cdot (\varrho CV) = -\nabla j \tag{5.6}$$

where σ is the stress tensor, $\boldsymbol{b}$ is the body force, $\boldsymbol{q}$ is the heat flux and $\boldsymbol{j}$ is the species diffusion flux. The detailed expressions for these terms are supplied by constitutive equations based on the characteristics of molecular or atomic movement.

5.2 Background of Macroscopic Transport Equations

Although transport phenomena in materials solidification can be described in detail by transport equations at the microscopic level, capable of handling the morphological characteristics during phase change, the direct application of the microscopic transport equations to solidification modeling is generally difficult, mainly because of the morphological complexities and the disparate scales.

5.2.1 Morphological Complexities and Disparate Scales

In the solidification process of alloys, a mushy zone forms between solid and liquid, where solid and liquid coexist as shown in Fig. 5.1. The geometry of the morphological structure between solid and liquid interface in this region is very complicated, and depends on the materials properties and the phase change environment such as thermal conditions and species distribution. Although analytical and numerical efforts have been made to investigate the details of the morphological structure in solidification (Langer 1980, Shyy et al. 1996a), difficulties exist in extending the computations to cover the whole mushy zone because of the disparate scales involved.

As an illustration, Figure 5.1 shows schematically two typical scales and corresponding physical phenomena that are involved in solidification. Other scales also exist in the solidification process, such as solute diffusion length scale and capillary length scale, but are not discussed here (Kurz and Fisher 1989, Shyy et al. 1996b).

First, at the macroscopic scale (i.e. characteristic size of an ampoule, normally having an order of magnitude of at least 10^{-2} m for most of the materials processing systems), convective–conductive heat transfer and macroscopic segregation are present (Fig. 5.1a).

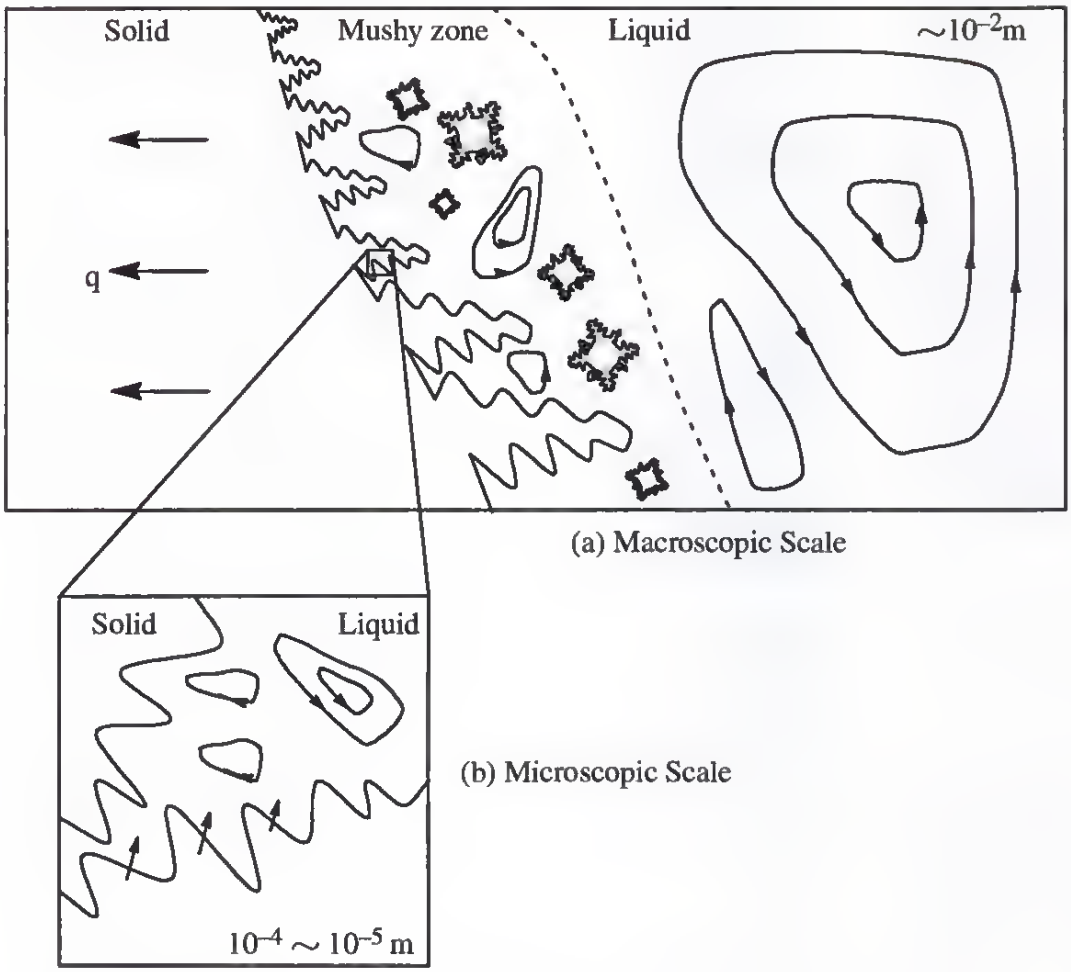

Figure 5.1. Disparate scales in solidification process.

Second, at the microscopic scale or morphological scale (i.e. $10^{-4} \sim 10^{-5}$ m for the typical microstructure of aluminum alloys), the interdendritic flow due to shrinkage, latent heat release due to phase change and species partition between solid and liquid phase appear (Fig. 5.1b). It is mentioned here that dendrites, eutectics, or combinations of these make up the microscopic morphology of any metallic microstructure after solidification (Kurz and Fisher 1989). The formation of a dendrite begins with the breakdown of an unstable planar solid/liquid interface. Perturbations are amplified until a marked difference in tip growth and depressions of the perturbed interface has occurred. The growth rate, morphology, or spacing of dendrites are all largely dependent upon the growth behavior of the tip region,

where heat or solute are redistributed. Dendrites are often encountered for undercooled pure materials or for directional solidification of dilute binary alloys (Beckermann and Viskanta 1993, Langer 1980). Eutectic morphologies also exist, which are characterized by the simultaneous growth of two (or more) phases from the liquid, and exhibit a wide variety of geometrical arrangements (Kurz and Fisher 1989).

As the morphological (microscopic) scale of dendritic or eutectic evolution and the macroscopic scale of global heat and fluid flows are different by several orders of magnitude, solving an entire solidification process as a microscopic problem is a formidable task. It requires grid resolutions of at least the dendritic or eutectic arm spacings for numerical modeling so that the detailed morphologies can be captured. Such direct numerical modeling is impractical even with the computational power available to date. In order to make the computational task tractable, a micro–macro model needs to be developed (Rappaz 1989, Shyy et al. 1996b). In other words, it is necessary to introduce some intermediate scale model to represent the physics of scales smaller than the computational mesh. In the following, a methodology based on the volume averaging procedure is presented.

5.2.2 Definition of Averaging Volume

The averaging volume dV is thus defined for such a purpose so that the scale it represents is small enough to capture the global fluid motion, heat transfer and species distribution as well as to track the liquid, solid and mushy zones, but large enough to smooth out the details of morphological complexities and the interdendritic fluid flow, heat release and species redistribution. In addition, based on the continuum hypothesis, the volume averaged quantities such as density, velocity and temperature should still be continuous functions of space and time. The morphological characteristics will be accounted for by the construction of constitutive equations, introduction of some effective coefficients of diffusivity, and their incorporation into the macroscopic equations derived by volume averaging.

As an illustration, Figure 5.2 shows the definition of the average density in the mushy zone as a function of the characteristic size of the averaging volume (Ganesan and Poirier 1990, Gray 1975). The average density is defined as the total mass of solid and liquid in the averaging volume divided by the averaging volume, dV. When dV is very small, the average density of the interdendritic mixture fluctuates because portions of liquid or solid phases included in dV are location dependent. This fluctuation diminishes as the size of dV increases, and within a certain characteristic size of dV, the density or any other average quantities become independent of dV. This region is represented by the horizontal line in Fig. 5.2. Accordingly, the averaging volume dV should have a characteristic length that satisfies:

$$O(l) < O(d) \tag{5.7}$$

where l is microscopic characteristic length (e.g. dendritic arm spacings), and d is characteristic length of the averaging volume. However, the characteristic size of dV should not be too large, otherwise, it becomes property dependent upon the global variations of location, temperature and composition.

The macroscopic transport equations based on the averaging volume dV, have been formulated in the literature mainly from two approaches. One is the so–called volume

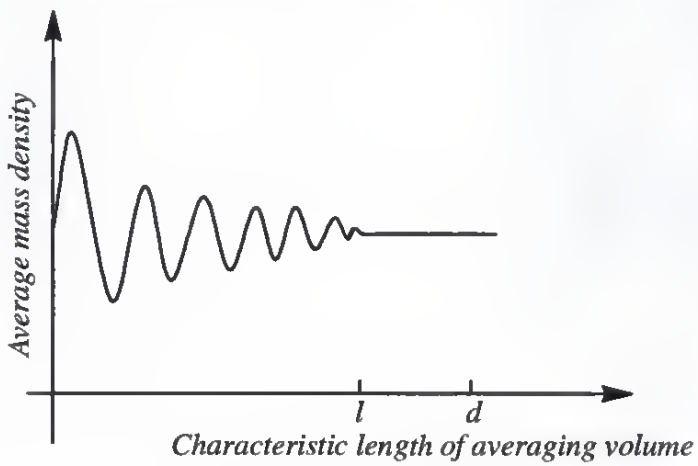

Figure 5.2. Average mass density as a function of the characteristic length of the averaging volume

averaging approach (Drew 1983, Slattery 1967, Whitaker 1967, Gray 1975, Gray 1983, Beckermann and Viskanta 1993, Ganesan and Poirier 1990). In this approach, the macroscopic equations of transport are directly derived from the microscopic equations. The second we call it the mixture approach (Bennon and Incropera 1987a, Poirier et al. 1991, Voller et al. 1989, Prescott and Incropera 1994). With this approach, certain mixture quantities in the mushy zone are first defined at the macroscopic scale, and then macroscopic equations are written down based on the conservation laws and mixture quantities. In the following, the details of these approaches will be given. Our emphasis will be placed on the volume averaging approach, which we consider to be more rigorous and systematic.

5.3 Volume Averaging Approach

The application of the concept of volume averaging to solidification processes is relatively recent. For example, Ganesan and Poirier (1990) derived in detail the macroscopic transport equations of mass and momentum for the flow of interdendritic liquid during solidification. They introduced two permeability coefficients in order to better describe the resistance of the solid to interdendritic liquid flow in the mushy zone. Further numerical calculation of the permeability for high volume fraction of liquid as a function of microscopic morphology, which merges with the empirical data at the low volume fraction, is recently reported in Bhat et al. (1995 a and b).

Beckermann and Viskanta (1993) systematically formulated the macroscopic transport equations of energy and species as well as mass and momentum. They discussed the possible mathematical constructions of the constitutive models that could incorporate the microscopic complexities into macroscopic equations. Follow-up numerical modeling based on their derived equations and the sensitivity study of solution characteristics to selections of constitutive models are also reported (Schneider and Beckermann 1995). They found that different constitutive models of microstructure predict quite different solidification characteristics in terms of solid concentration, eutectic fractions, number,

length and orientation of segregated channels, etc. They further suggested that constitutive models as a function of mushy zone microstructure should be obtained by combining the experimental measurement and numerical simulation.

Despite these consistent efforts that have been initiated for the modeling of solidification process, it appears that there are still important issues related to the formulation of macroscopic transport equations that need to be further resolved. For example, microscopic deviation terms result from the nonuniformity of the dendritic growth rate, temperature and species concentration have not been addressed, although both Ganesan and Poirier (1990) and Viskanta and Beckermann (1993) mentioned that these terms are important in regions of high volume fraction of liquid in the mushy zone. To date, no robust models have been proposed in the literature to capture such phenomena as columnar or equiaxed growth, constitutive undercooling and morphologies of dendritic or eutectic evolution. Another issue that needs to be clarified further is the introduction of the effective coefficients of diffusivity which are supposed to account for the reduced diffusive effects of heat and species in the interdendritic meshwork.

In this study, we will attempt to address the derivation of unified macroscopic transport equations, valid in solid, liquid and mushy zones, for the modeling of materials solidification, by following the literature (Drew 1983, Slattery 1967, Whitaker 1967, Gray 1975, Gray 1983, Beckermann and Viskanta 1993, Ganesan and Poirier 1990). In particular, we will propose a microscopic deviation model adopting the concept of the subgrid scale model in turbulent large eddy simulation and also discuss corresponding closure problems. Concepts that are used by the averaging procedure are first given, followed by detailed derivations of the macroscopic transport equations. Then the application of this approach to mass, energy, species and momentum equations is given. All the assumptions made during the derivations will be highlighted. They are invoked only at the final stage of derivation and can be easily relaxed.

5.3.1 Definitions and Theorems

(1) Phase function γ_k:

The phase function γ_k is a function of space and time, equalling 1 in phase k and zero elsewhere. It has also been denoted by X_k (Drew 1983, Beckermann & Viskanta 1993) or a_k (Whitaker 1967) in the literature.

(2) Volume fraction g_k:

The volume fraction g_k is defined as

$$g_k = \frac{1}{dV}\int_{dV} \gamma_k(r,t)dv = dV_k/dV \tag{5.8}$$

where dV_k is the portion of dV that is occupied by phase k, and dv is an infinitesimal element relative to dV. Some researchers denote volume fraction as ε_k (Beckermann & Viskanta 1993, Gray 1975).

(3) Intrinsic volume averaged (or pore) quantity $\overline{\Psi_k}^k$:

The intrinsic volume averaged quantity is defined as

$$\overline{\Psi_k}^k = \frac{1}{dV_k}\int_{dV} \Psi_k(r,t)\gamma_k(r,t)dV \tag{5.9}$$

$\langle\Psi_k\rangle^k$ has also been used by others to represent this quantity. The definition of $\overline{\Psi_k}^k$ here represents the averaged value of $\Psi_k(r,t)$ in the control volume dV_k; if $\Psi_k(r,t)$ is uniformly distributed in dV_k, then $\overline{\Psi_k}^k = \Psi(r,t)$. (The augments r and t will be dropped subsequently for conciseness.)

(4) Volume averaged (or superficial) quantity $\overline{\Psi_k}$:

The volume averaged quantity is defined as

$$\overline{\Psi}_k = \frac{1}{dV}\int_{dV} \Psi_k \gamma_k dV \tag{5.10}$$

It is the averaged value of quantity Ψ_k in phase k over the entire averaging volume dV. By comparing Eq. (5.9) and (5.10), we obtain

$$g_k \overline{\Psi}_k = \overline{\Psi}_k^k \tag{5.11}$$

(5) Fluctuating component $\hat{\Psi}_k$:

The fluctuation component $\hat{\Psi}_k$ represents the deviation of Ψ_k from the intrinsic volume average, and

$$\hat{\Psi}_k = (\Psi_k - \overline{\Psi}_k^k)\gamma_k \tag{5.12}$$

In phase k, it is zero only when Ψ_k is uniformly distributed, i.e. $\Psi_k = \overline{\Psi}_k^k$. According to this definition, we have the following identity for changing the average of two products to the product of averaged quantities (Gray 1975):

$$\overline{\Psi_k \Phi_k} = g_k \overline{\Psi}_k^k \overline{\Phi}_k^k + \overline{\hat{\Psi}_k \hat{\Phi}_k} \tag{5.13}$$

where $$\overline{\hat{\Psi}_k \hat{\Phi}_k} = \frac{1}{dV}\int_{dV} \hat{\Psi}_k \hat{\Phi}_k dv$$

It should be mentioned here that this identity is incorrectly expressed by Beckermann and Viskanta (1993) and Ganesan and Poirier (1990), in which the first term on the right hand side of Eq. (5.13) is expressed as either a $\overline{\Psi_k \Phi_k}$ or a $\overline{\Psi}_k^k \overline{\Phi}_k^k$ (without g_k). Gray (1975) gives a very clear derivation of this identity.

(6) Volume averaging theorems:

The volume averaging theorems listed below have been derived rigorously by several workers (Howes and Whitaker 1985, Gray 1975).

Theorem 1: Relates the average of the time derivative to the time derivative of the average, i.e.

$$\frac{1}{dV}\int_{dV}\left(\frac{\partial \Psi_k}{\partial t}\right)\gamma_k dv = \frac{\partial}{\partial t}\left[\frac{1}{dV}\int_{dV}\Psi_k\gamma_k dv\right] - \frac{1}{dV}\int_{dA_k}\Psi_k \boldsymbol{w}\cdot\boldsymbol{n}_k da$$

or

$$\overline{\frac{\partial \Psi_k}{\partial t}} = \frac{\partial \overline{\Psi_k}}{\partial t} - \frac{1}{dV}\int_{dA_k}\Psi_k\gamma_k \boldsymbol{w}\cdot\boldsymbol{n}_k da \tag{5.14}$$

where dA_k is the interfacial area of phase k with other phases, $\boldsymbol{n}_k$ is the outward unit normal of the infinitesimal element of area da of phase k, and $\boldsymbol{w}$ is the velocity of the microscopic interface.

Theorem 2: Relates the average of the spatial derivative to the spatial derivative of the average, i.e.

$$\frac{1}{dV}\int_{dV}(\nabla\Psi_k)\gamma_k dv = \nabla\left[\frac{1}{dV}\int_{dV}\Psi_k\gamma_k dv\right] + \frac{1}{dV}\int_{dA_k}\Psi_k\boldsymbol{n}_k da$$

or

$$\overline{\nabla\Psi_k} = \nabla\overline{\Psi_k} + \frac{1}{dV}\int_{dA_k}\Psi_k\boldsymbol{n}_k da \tag{5.15}$$

A variation of this theorem is given by (Gray 1975) as

$$\overline{\nabla\Psi_k} = g_k\nabla\overline{\Psi_k}^k + \frac{1}{dV}\int_{dV}\hat{\Psi}_k\boldsymbol{n}_k da \tag{5.16}$$

5.3.2 The Derivation Procedure

Applying the general microscopic transport equation (5.2) to phase k, we have

$$\frac{\partial \Phi_k}{\partial t} + \nabla\cdot(\Phi_k V_k) = \nabla\cdot J_k + S_k \tag{5.17}$$

Multiplying each side of Eq. (5.17) by γ_k and average over dV, it becomes

$$\underbrace{\frac{1}{dV}\int_{dV}\frac{\partial \Phi_k}{\partial t}\gamma_k dv}_{1st} + \underbrace{\frac{1}{dV}\int_{dV}\nabla\cdot(\Phi_k V_k)\gamma_k dv}_{2nd} = \underbrace{\frac{1}{dV}\int_{dV}\nabla\cdot J_k\gamma_k dv}_{3rd} + \underbrace{\frac{1}{dV}\int_{dV} S_k\gamma_k dv}_{4th} \tag{5.18}$$

Applying Theorem 1, shown in Eq. (5.14), to the first term, we obtain

$$\frac{1}{dV}\int_{dV}\left(\frac{\partial \Phi_k}{\partial t}\right)\gamma_k dv = \frac{\partial \overline{\Phi_k}}{\partial t} + \frac{1}{dV}\int_{dA_k}\Phi_k w_k\cdot n_k da \tag{5.19}$$

Applying Theorem 2, shown in Eq. (5.15), to the second, third and fourth terms, we get

$$\frac{1}{dV}\int_{dV}(\nabla\Phi_k V_k)\gamma_k dv = \nabla\cdot\overline{\Phi_k V_k} + \frac{1}{dV}\int_{dA_k}\Phi_k V_k\cdot n_k da \tag{5.20}$$

$$\frac{1}{dV}\int_{dV}\nabla\cdot J_k\gamma_k dv = \nabla\cdot\overline{J}_k + \frac{1}{dV}\int_{dA_k} J_k\cdot n_k da \tag{5.21}$$

$$\frac{1}{dV}\int_{dV} S_k\gamma_k dv = \overline{S_k} \tag{5.22}$$

Furthermore, by applying the identity of Eq. (5.13), $\nabla\cdot\overline{\Phi_k V_k}$ in Eq. (5.20) becomes

$$\nabla\cdot\overline{\Phi_k V_k} = \nabla\cdot g_k\overline{\Phi_k}^k\overline{V_k}^k + \nabla\cdot\overline{\hat{\Phi}_k\hat{V}_k} \tag{5.23}$$

Substituting Eqs. (5.19 ~ 5.23) into Eq. (5.18), we get

$$\frac{\partial \overline{\Phi}_k}{\partial t} + \nabla\cdot g_k\overline{\Phi_k}^k\overline{V_k}^k = \nabla\cdot\overline{J_k} + \overline{S_k} + \tag{5.24}$$

$$\underbrace{\nabla\cdot\frac{1}{dV}\int_{dV}(-\hat{\Phi}_k\hat{V}_k)dv}_{I_k^D} + \underbrace{\frac{1}{dV}\int_{dA_k} J_k\cdot n_k da}_{I_k^J} + \underbrace{\frac{1}{dV}\int_{dA_k}\Phi_k(w_k - V_k)\cdot n_k da}_{I_k^Q}$$

This is the exact form of the macroscopic transport equations. Compared with the exact microscopic equations of transport, i.e. Eq. (5.17), three extra terms of I_k^D, I_k^J and I_k^Q appear from this volume averaging procedure. We call I_k^D the microscopic deviation term and I_k^J and I_k^Q the interfacial terms, because I_k^D involves volume integration and I_k^J and I_k^Q

involve surface integration. In order to solve Eq. (5.24), these terms have to be modeled, i.e. the so–called macroscopic constitutive equations must be constructed, as discussed below.

5.3.3 The Treatment of Microscopic Deviation and Interfacial Terms

(i) Microscopic deviation term I_k^D

This term appears because of the deviation of field quantities $\Phi_k(\boldsymbol{r}, t)$ and $V_k(\boldsymbol{r}, t)$ from their intrinsically averaged counterparts. From the definition of Eq. (5.13), I_k^D is zero only when $\Phi_k(\boldsymbol{r}, t)$ or $V_k(\boldsymbol{r}, t)$ are uniformly distributed in dV_k, i.e. $\hat{\Phi}_k$ or $\hat{V}_k$ are zero. However, at the microscopic (or morphological) scale, there always exist species, temperature and velocity gradients in the liquid, due to solute rejection, heat release, and no slip velocity conditions; hence $\Phi_k(\boldsymbol{r}, t)$ and $V_k(\boldsymbol{r}, t)$ are not uniform within the averaging volume. Despite this fact, almost all solidification models reported in the literature neglected the microscopic deviation term (Ganesan and Poirier1990, Voller et al. 1989, Bennon and Incropera 1987b, Prescott and Incropera 1994, Schneider and Beckermann 1995). By neglecting this term, the real mechanisms of columnar or equiaxed growth cannot be captured. Therefore, a microscopic deviation model needs to be developed to relate the deviation of velocity, temperature and species concentration from their averaged counterparts to the corresponding gradients. Analogy can be found in subgrid scale (SGS) model in Large Eddy Simulation (LES).

In large eddy simulation, the subgrid–scale model representing the action of scales smaller than the computational mesh of large scale is introduced in order to increase the Reynolds number in the simulations (Moin et al. 1991, Lesieur 1993). The large–scale field is computed directly from the solution of the local volume averaged Navier–Stokes equations, and the subgrid scale stresses are modeled. The subgrid scale model then represents the effect of the small scales on the large scale motions. This concept of LES can

help alleviate the severe Reynolds number restriction in direct numerical simulation (DNS) by modeling the subgrid behavior. Among many SGS models existing in the literature, the simplest one is the Smagorinsky model (Moin et al. 1991, Lesieur 1993). If we denote the extra terms that arise from the volume averaging procedure of the inertial term in Navier–Stokes equation as τ'_{ij}, which appears because of the fluctuation of turbulent velocity from its volume averaged counterpart, then this term can be expressed similarly in terms of strains of the flow field through an eddy viscosity coefficient, i.e.

$$\tau'_{ij} = 2KS_{ij} \tag{5.25}$$

where S_{ij} is the volume averaged strain rate tensor, i.e.

$$S_{ij} = \frac{1}{2}\left(\frac{\partial \overline{V_i}}{\partial x_j} + \frac{\partial \overline{V_j}}{\partial x_i}\right) \tag{5.26}$$

and

$$K = (C_s\Delta)^2(2S_{ij}S_{ij})^{\frac{1}{2}} \tag{5.27}$$

A basic ingredient that characterizes the subgrid scale model used in the large eddy simulation is that their characteristic length scale is usually given by the grid size (Germano 1992). In the above expression, Δ represents a grid spacing and C_s is an adjustable constant. C_s can be obtained by either using direct numerical simulation from isotropic turbulence, homogeneous shear flow, etc., or conducting corresponding experiments (Moin et al. 1991). It might be interpreted as the ratio of the characteristic subgrid size to the computational grid size.

The concept of averaging volume we used for the formulation of macroscopic transport equations can draw analogy to the concept of subgrid scale. Since the microscopic deviation term I_k^D also arises from the deviation of microscopic quantities $\Phi_k(\boldsymbol{r}, t)$ and $V_k(\boldsymbol{r}, t)$ from their averaged counterparts in dV_k, it is then also plausible for us to relate this term to the gradients of $\overline{\Phi_k}(\boldsymbol{r}, t)$ and $\overline{V_k}(\boldsymbol{r}, t)$. Therefore, we can adopt a formulation similar to that of Smagorinsky model, in which the integral portion of I_k^D is expressed as

$$\frac{1}{dV}\int_{dV}(-\hat{\Phi}_k\hat{V}_k)dv = 2K\nabla\overline{\Phi}_k^{\,k} \tag{5.28}$$

In this expression, $\nabla\overline{\Phi}_k^{\,k}$ has been extended to represent not only the strain rate as in LES, but also the gradient of temperature and species concentration. K is given by the same format as in Eq.(5.27) as

$$K = (a_k l)^2(2S_{ij}S_{ij})^{\frac{1}{2}} \tag{5.29}$$

where a_k is also an adjustable constant of phase k that should be decided based on experimental evidence. It should be noted that since the capillary effect has not been explicitly accounted for in the averaging process, its implication will need to be reflected by the adjustable coefficient. Accordingly, the value of this coefficient will change according to the variations in microscopic morphologies. In addition, l here does not represent the computational mesh size, but the morphological length scale, which, according to the established theory (Langer 1980, Sbyy 1994), can be taken as the square root of the product of the capillary and conduction scales for dendritic structures.

This formulation of Eq. (5.28) can be seen to reflect some basic features of interdendritic actions. For example, in the mushy zone where the liquid volume fraction is close to unity, dendrites or eutectics grow as a result of gradients in velocity, temperature and species concentration. According to Eq.(5.28), the microscopic deviation effect in this region is therefore significant. Hence, the inclusion of microscopic deviation term is expected to be able to capture in more detail the dendritic or eutectic evolution in this region. In the mushy zone where the liquid volume fraction is approaching zero, i.e. near the dendrite root region, as the interdendritic fluid motion is nearly stagnant, the microscopic deviation term will gradually diminish as the solid region is approached.

It should be mentioned here that, although the treatment of the microscopic deviation term is virtually absent in the literature concerning the modeling of solidification phenomena, it has been discussed elsewhere. For example, Whitaker (1967) considered the microscopic deviation term in the macroscopic equation of species transport as a function

of variables such as the averaged species concentration and the gradients of concentration and velocity. Although it provided a basis for the correlation of experimental data and illustrated the connection between the microscopic and macroscopic equations, his definition of the fluctuating component was ambiguous and led to a non–zero value of microscopic deviation term even when Φ_k is uniform in dV_k (Gray 1975). By our definition of fluctuating components and the proposed model for microscopic deviation term, these problems will not appear.

(ii) Interfacial terms I_k^I and I_k^Q

It can be seen from Eq. (5.24) that these two terms arise from the interfacial integration over dA_k. I_k^Q accounts for the interfacial transfer due to phase change. Physically, it represents advection of interfacial mass, momentum, heat or species of phase k due to the relative motion of the solid–liquid interface. I_k^I accounts for the effect of interfacial stress, heat and species transfer. Physically, it represents the transport phenomena between the phases within dV by diffusion and are related to the gradients of microscopic velocity, temperature and species concentration on each side of the solid–liquid interface dA_k (Beckermann and Viskanta 1993). Depending on different modeling efforts, these terms are treated differently, as outlined below.

(1) The two–phase model.

In this model, the transport equation (5.24) is applied to each phase and is solved separately (Ni and Beckermann 1990). The equations are coupled through the interfacial conditions estimated by I_k^I and I_k^Q, which are expressed as a function of the interfacial concentration S_v ($S_v = dA_k/dV$). The variable S_v has been adopted by many researchers in the multiphase research community to account for the morphological complexities of porous media or solidification dendritic meshwork. Gray (1975) formed the interfacial species transfer due to the concentration gradient as a product of mass transfer coefficient

and a concentration driving force. Beckermann and Viskanta (1993) represented the interfacial transfer due to phase change (I_k^Q) and the interfacial transfer due to variable gradient (I_k^J) all as the product of the interfacial area concentration S_v and a mean interfacial flux.

The main advantage of the two–phase model, as argued by Ni and Beckermann (1990), is that it can account for non–equilibrium effects during solidification, such as rapid solidification, floating and settling of small equiaxed crystals, nucleation, etc. However, numerical computations with such a model requires explicit treatment of the boundary between highly irregular domains. In addition, detailed and accurate formulation of those interfacial transfer terms has to be provided.

(2) The one–phase model.

In this model, since the averaged macroscopic equations from different phases are added within the averaging volume dV, detailed modeling of the interfacial transfer terms I_k^J and I_k^Q can be avoided. Because the heat or mass lost from interface by one phase is gained by other phases, i.e.

$$\sum I_k^Q = 0 \qquad \text{and} \qquad \sum I_k^J = 0 \tag{5.30}$$

Hence the explicit treatment of interfacial flux is not necessary here. However, this one–phase model has the disadvantage that relationships between the macroscopic variables of each phase have to be provided. Compared to the two–phase model, the one–phase model is easier to implement, and will be presented in more details in the following, including the averaged macroscopic equations of mass, heat, species and momentum in the context of alloy solidification.

5.4 Macroscopic Transport Equations via Volume Averaging Approach

To aid the discussion, assumptions in the modeling of binary solidification processes are first made.

Assumption 1: Only two phases, liquid and solid, are considered, i.e. k=l or s.

Assumption 2: Variations of material properties in dV_k are neglected, although globally they may vary, i.e.

$$\overline{\varrho_k}^k = \varrho_k = \overline{\varrho_k}/g_k, \quad \overline{\varrho_k \Phi_k} = \varrho_k \overline{\Phi_k}$$

$$\overline{\mu_k}^k = \mu_k \ , \quad \overline{k_k}^k = k_k \ , \quad \overline{D_k}^k = D_k$$

In the above, μ is viscosity, k is thermal conductivity and D is the coefficient of binary species diffusivity. In the following derivations, the momentum equation will be featured last because it has been studied widely in the research community and is also the most controversial.

5.4.1 Macroscopic Equation of Mass Conservation

In this case, $\Phi = \varrho, \boldsymbol{J} = 0$ and $S = 0$. According to Eq. (5.24) the liquid and solid mass equations yield, respectively,

$$\frac{\partial \overline{\varrho_l}}{\partial t} + \nabla \cdot g_l \varrho_l \overline{\boldsymbol{V}_l}^l = I_l^{\varrho} \tag{5.31}$$

$$\frac{\partial \overline{\varrho_s}}{\partial t} + \nabla \cdot g_s \varrho_s \overline{\boldsymbol{V}_s}^s = I_s^{\varrho} \tag{5.32}$$

where

$$I_l^{\varrho} = \frac{1}{dV} \int_{dA_k} (\boldsymbol{w}_l - \boldsymbol{V}_l) \cdot \boldsymbol{n}_l da \qquad \text{and} \qquad I_s^{\varrho} = \frac{1}{dV} \int_{dA_k} (\boldsymbol{w}_s - \boldsymbol{V}_s) \cdot \boldsymbol{n}_s da$$

Here the microscopic deviation term disappeared due to the assumption 2, i.e. $\hat{\varrho}_l = \hat{\varrho}_s = 0$. Now adding Eqs. (5.31) and (5.32) and considering the interfacial mass flux balance, i.e. the mass lost by one phase is gained by the other phase, or $I_l^{\varrho} + I_s^{\varrho} = 0$, we get

$$\frac{\partial \left(\overline{\varrho_l} + \overline{\varrho_s} \right)}{\partial t} + \nabla \cdot \left(g_l \varrho_l \overline{\boldsymbol{V}_l}^l + g_s \varrho_s \overline{\boldsymbol{V}_s}^s \right) = 0 \tag{5.33}$$

5.4.2 Macroscopic Equation of Energy Conservation

In this case, $\Phi = \varrho H$, where H represents the total enthalpy, and $S = 0$. Furthermore, we utilize Fourier's law, neglecting other heat diffusion fluxes such as Soret and Dufour effects (Bird et al. 1960) as they are not important in conventional solidification process, i.e.

Assumption 3: Fourier's law for heat flux, i.e. $\boldsymbol{J} = -k\nabla T$

Then for liquid and solid phases, the averaged energy equations yield:

$$\frac{\partial \varrho_l \overline{H_l}}{\partial t} + \nabla \cdot g_l \varrho_l \overline{H_l}^l \overline{V_l}^l = \nabla \cdot \overline{(k_l \nabla T_l)} + I_l^D + I_l^Q + I_l^J \tag{5.34}$$

$$\frac{\partial \varrho_s \overline{H_s}}{\partial t} + \nabla \cdot g_s \varrho_s \overline{H_s}^s \overline{V_s}^s = \nabla \cdot \overline{(k_s \nabla T_s)} + I_s^D + I_s^Q + I_s^J \tag{5.35}$$

The physical meaning of the terms on the left hand side of Eqs. (5.34) and (5.35) are obvious, as they are the same as their microscopic counterparts. The terms on the right hand side of Eqs. (5.34) and (5.35), however, need further discussions. Equation (5.34) will be used for this purpose.

(i) $\nabla \cdot \overline{k_l \nabla T_l}$

By applying Theorem 2 (Eq. (5.16)) and using assumption 2, $\overline{k_l \nabla T_l}$ can be further expanded as

$$\overline{k_l \nabla T_l} = g_l k_l \nabla \overline{T_l}^l + k_l \frac{1}{dV} \int_{dA_k} \hat{T}_l \boldsymbol{n}_l da \tag{5.36}$$

where the term involving the area integration is called the tortuosity factor (Gray 1975), because it accounts for a decreased diffusion rate due to the geometry of the dendrites. In addition, since the thermal diffusion effect should be zero when the temperature in the liquid is uniform, this implies that this term is related to the temperature gradient. Based on this argument, an effective conductivity is introduced and is related to the macroscopic variable as (Beckermann and Viskanta 1993, Whitaker 1967)

$$\overline{k_l \nabla T_l} = g_l k_l^* \nabla \overline{T}_l^l \tag{5.37}$$

where the contribution of the area integration is accounted for with the newly defined effective conductivity k_l^*. To close this formulation, k_l^* as a function of the microscopic morphology needs to be specified. A commonly used variable to account for the morphological tortuosity is the interfacial area concentration S_v, and k_l^* is written as a function of S_v. An alternative variable to account for the tortuosity is the dendritic arm number N. As the number of dendritic arms increases, the value of S_v increases and hence the structure is more tortuous. The exact functional form of k_l^* is based on empirical studies. Beckermann and Viskanta (1993) have reviewed several empirical relations proposed in the literature, in the form of $k_l^* = k_l^*(S_v)$, where S_v is expressed as a function of the liquid volume fraction g_l. To illustrate such an approach, let us use the following example.

It is known that during solidification, S_v in the mushy region increases from zero near the dendrite root, eventually reaches a maximum value and then decreases again to zero near the primary dendrite tip region where the fluid fraction is approaching 1. According to these characteristics, an empirical relation suggested by Speich and Fisher (1966) is

$$S_v = c g_l (1 - g_l) \tag{5.38}$$

where c is a constant. Furthermore, as the effective conductivity of $k_l^*(S_v)$ should reduce to its microscopic counterpart as it approaches the liquid or solid zone, hence the following relation can be considered:

$$k_l^*(S_v) = k_l(1 - S_v/c) \tag{5.39}$$

hence

$$k_l^*(S_v) = k_l(1 - g_l + g_l^2) \tag{5.40}$$

These relations are shown in Fig. 5.3.

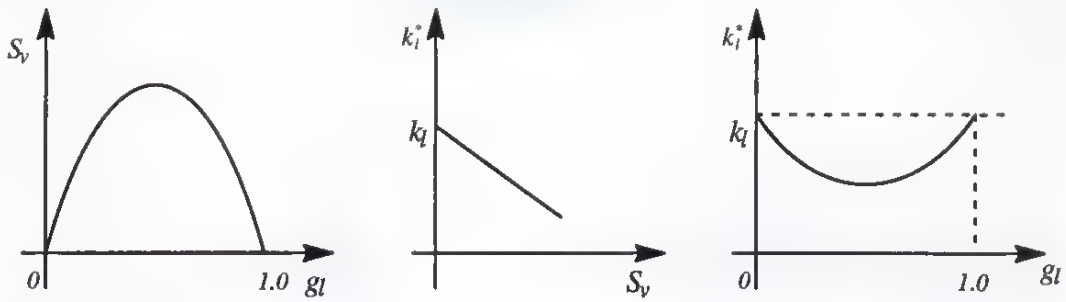

Figure 5.3. Schematic of the effective conductivity as a function of microscopic morphology.

The above example is just a schematic illustration to the closure and the construction of effective coefficient as a function of microscopic complexity. In reality, the relation might not be so simple as parabolic or linear and should be determined from experimental measurement or direct numerical modeling of dendrite morphology (Bhat et al. 1995 a and b). This is an area that has recently received considerable attention in the solidification community; however, further effort will be required.

(ii) I_l^D

From the microscopic deviation model of Eq. (5.28) in section 5.3.3, I_l^D can be written as

$$I_l^D = \nabla \cdot (2\varrho CpK)\nabla \overline{T}_l^I$$

and

$$K = (a_l I)^2 (2S_{ij}S_{ij})^{\frac{1}{2}}$$

where a_l is a constant that should be decided from experimental or theoretical analysis. Furthermore, let us define the microscopic deviation conductivity as $k_l^D = 2\varrho CpK$, then Eq. (5.34) becomes

$$\frac{\partial \varrho_l \overline{H}_l}{\partial t} + \nabla \cdot g_l \varrho_l \overline{H}_l^I \overline{V}_l^I = \nabla \cdot (g_l k_l^* + g_l k_l^D)\nabla \overline{T}_l^I + I_l^Q + I_l^J \qquad (5.41)$$

It is noted that k_l^* accounts for the reduced diffusion effect due to the tortuosity, while k_l^D accounts for the increased effect of diffusion due to the gradient of temperature. The deviation of k_l^* from its microscopic counterpart is significant when dendritic morphology is complex, as shown by Fig. 5.3, while k_l^D is significant when the volume fraction of liquid approaches unity.

In the same manner, Eq. (5.35) can also be written as

$$\frac{\partial \varrho_s \overline{H_s}}{\partial t} + \nabla \cdot g_s \varrho_s \overline{H_s}^s \overline{V_s}^s = \nabla \cdot (g_s k_s^* + g_s k_s^D) \nabla \overline{T_s}^s + I_s^Q + I_s^J \tag{5.42}$$

(iii) I_l^J and I_l^Q

Since the one phase model is applied here, these interfacial terms need not be modeled because the interfacial heat flux and heat transfer between phases during solidification are balanced with each other, i.e.

$$\left(I_l^Q + I_s^Q\right) = \left(I_l^J + I_s^J\right) = 0$$

So adding Eq. (5.41) and (5.42), the final form of the macroscopic mixture equation of energy conservation is

$$\frac{\partial\left(\varrho_l \overline{H_l} + \varrho_s \overline{H_s}\right)}{\partial t} + \nabla \cdot \left(g_l \varrho_l \overline{H_l}^l \overline{V_l}^l + g_s \varrho_s \overline{H_s}^s \overline{V_s}^s\right) = \nabla \cdot \left[g_l\left(k_l^* + k_l^D\right)\nabla \overline{T_l}^l + g_s\left(k_s^* + k_s^D\right)\nabla \overline{T_s}^s\right] \tag{5.43}$$

5.4.3 Macroscopic Equation of Species Conservation

In this case, $\Phi = \varrho C$, in which C is species concentration in weight percentage, and $S = 0$. Furthermore, we utilize the Fick's law for species diffusion flux, i.e.

Assumption 4: Fick's law for binary species flux, i.e. $\boldsymbol{J} = -\varrho D \nabla C$

where D is the binary diffusion coefficient. For liquid and solid phases, the averaged species equations yield, respectively,

$$\frac{\partial \varrho_l \overline{C_l}}{\partial t} + \nabla \cdot g_l \varrho_l \overline{C_l}^l \overline{V_l}^l = \nabla \cdot \overline{(\varrho_l D_l \nabla C_l)} + I_l^D + I_l^Q + I_l^J \tag{5.44}$$

$$\frac{\partial \varrho_s \overline{C_s}}{\partial t} + \nabla \cdot g_s \varrho_s \overline{C_s}^s \overline{V_s}^s = \nabla \cdot \overline{(\varrho_s D_s \nabla C_s)} + I_s^D + I_s^Q + I_s^J \tag{5.45}$$

Following the same argument as in the derivation of energy equation, the first term on the right hand side of Eq. (5.44) can be written in terms of the effective diffusion coefficient as

$$\overline{\varrho D_l \nabla C_l} = g_l \varrho_l D_l^* \nabla \overline{C_l}^l \tag{5.46}$$

where the area integral effect has been brought into the newly defined effective diffusivity D_l^*, which may be written as a function of area concentration S_v. The detailed expression for D_l^*, which accounts for the reduced diffusivity due to increased tortuosity, can be determined by an argument similar to that presented in section 5.4.2 for the treatment of k_l^*.

In addition, from Eq. (5.28), the liquid microscopic deviation term can be written as

$$I_l^D = \nabla \cdot (2\varrho K) \nabla \overline{C_l}^l$$

Defining the microscopic deviation diffusion coefficient as $D_l^D = 2\varrho K$, Eq. (5.44) becomes

$$\frac{\partial \varrho_l \overline{C_l}}{\partial t} + \nabla \cdot g_l \varrho_l \overline{C_l}^l \overline{V_l}^l = \nabla \cdot (g_l \varrho_l D_l^* + g_l \varrho_l D_l^D) \nabla \overline{C_l}^l + I_l^Q + I_l^J \tag{5.47}$$

Eq. (5.45) can also be rewritten in the same manner as

$$\frac{\partial \varrho_s \overline{C_s}}{\partial t} + \nabla \cdot g_s \varrho_s \overline{C_s}^s \overline{V_s}^s = \nabla \cdot (g_s \varrho_s D_s^* + g_s \varrho_s D_s^D) \nabla \overline{C_s}^s + I_s^Q + I_s^J \tag{5.48}$$

Adding Eqs. (5.47) and (5.48) together, and taking into account that the interfacial species flux and species transfer due to solidification balance with each other, i.e.

$$\left(I_l^Q + I_s^Q\right) = \left(I_l^J + I_s^J\right) = 0$$

the final form of the macroscopic mixture equation of species conservation is

$$\frac{\partial\left(\varrho_l\overline{C_l} + \varrho_s\overline{C_s}\right)}{\partial t} + \nabla\cdot\left(g_l\varrho_l\overline{C_l}^l\overline{V_l}^l + g_s\varrho_s\overline{C_s}^s\overline{V_s}^s\right) = \nabla\cdot\left[g_l\varrho_l\left(D_l^* + D_l^D\right)\nabla\overline{C_l}^l + g_s\varrho_s\left(D_s^* + D_s^D\right)\nabla\overline{C_s}^s\right] \tag{5.49}$$

5.4.4 Macroscopic Equation of Momentum Conservation

In this case, $\Phi = \varrho V$, in which V is velocity vector and $S = b$ is the body force vector. Furthermore, we assume a Newtonian fluid and hence the viscous stress is proportional to the ratio of deformation, i.e.,

Assumption 5: Newtonian Fluid Flow, i.e. $J = -\nabla P + \mu[\nabla V + (\nabla V)^t]$

Then for liquid and solid phases, the averaged momentum equations yield:

$$\frac{\partial\varrho_l\overline{V_l}}{\partial t} + \nabla\cdot g_l\varrho_l\overline{V_l}^l\overline{V_l}^l = -\nabla\overline{P_l} + \nabla\cdot\left[\overline{\mu_l\nabla V_l} + \overline{\mu_l(\nabla V_l)^t}\right] + I_l^D + I_l^Q + I_l^J + \overline{b_l} \tag{5.50}$$

$$\frac{\partial\varrho_s\overline{V_s}}{\partial t} + \nabla\cdot g_s\varrho_s\overline{V_s}^s\overline{V_s}^s = -\nabla\overline{P_s} + \nabla\cdot\left[\overline{\mu_s\nabla V_s} + \overline{\mu_s(\nabla V_s)^t}\right] + I_s^D + I_s^Q + I_s^J + \overline{b_s} \tag{5.51}$$

Following the same argument as in the derivation of energy and species equations, the second term on the right hand side of Eq. (5.50) can be written in terms of the effective viscosity as

$$\overline{\mu_l\nabla V_l} + \overline{\mu_l(\nabla V_l)^t} = \mu_l^*\left[\nabla\overline{V_l}^l + (\nabla\overline{V_l}^l)^t\right] \tag{5.52}$$

With this assumption, and combined with the model we proposed earlier for the microscopic deviation term shown in Eq. (5.28), i.e.

$$I_l^D = \nabla\cdot(2\varrho K)\left[\nabla\overline{V_l}^l + \left(\nabla\overline{V_l}^l\right)^t\right]$$

Eq. (5.50) becomes

$$\frac{\partial \varrho_l \overline{V_l}}{\partial t} + \nabla \cdot g_l \varrho_l \overline{V_l}^l \overline{V_l}^l = -\nabla \overline{P_l} + \nabla \cdot (g_l \mu_l^* + g_l \mu_l^D) \left[\nabla \overline{V_l}^l + \left(\nabla \overline{V_l}^l \right)^t \right] + I_l^Q + I_l^J \tag{5.53}$$

where the microscopic deviation viscosity is defined as $\mu_l^D = 2\varrho K$, Eq. (5.51) can also be rewritten in the same manner as

$$\frac{\partial \varrho_s \overline{V_s}}{\partial t} + \nabla \cdot g_s \varrho_s \overline{V_s}^s \overline{V_s}^s = -\nabla \overline{P_s} + \nabla \cdot (g_s \mu_s^* + g_s \mu_s^D) \left[\nabla \overline{V_s}^s + \left(\nabla \overline{V_s}^s \right)^t \right] + I_s^Q + I_s^J \tag{5.54}$$

Eqs. (5.53) and (5.54) may be added, according to the fact that the interfacial momentum fluxes due to solidification balance each other, i.e.

$$\left(I_l^Q + I_s^Q \right) = 0$$

However, the interfacial stress in this case is not balanced; across the interface, there is a jump condition due to surface tension (Drew 1983), i.e.

$$\left(I_l^J + I_s^J \right) = \sigma \varkappa$$

where σ is the surface tension, assumed to be constant, and $\varkappa$ is the mean curvature of the interface. Many previous derivations do not explicitly include this term (Beckermann and Viskanta 1993, Ganesan and Poirier 1990), as this effect is small in alloy solidification and hence often negligible. This term is considered here for completeness. The final form of the macroscopic mixture equation of momentum conservation then yields

$$\frac{\partial \left(\varrho_l \overline{V_l} + \varrho_s \overline{V_s} \right)}{\partial t} + \nabla \cdot \left(g_l \varrho_l \overline{V_l}^l \overline{V_l}^l + g_s \varrho_s \overline{V_s}^s \overline{V_s}^s \right) = -\nabla \left(\overline{P_l} + \overline{P_s} \right) + \tag{5.55}$$
$$\nabla \cdot \left\{ g_l \left(\mu_l^* + \mu_l^D \right) \left[\nabla \overline{V_l}^l + \left(\overline{V_l}^l \right)^t \right] + g_s \left(\mu_s^* + \mu_s^D \right) \nabla \left[\overline{V_s}^s + \left(\overline{V_s}^s \right)^t \right] \right\} + \boldsymbol{b} + \sigma \varkappa$$

5.4.5 Special Comment on the Formulation of Effective Coefficients

In section 5.4.2 ~ 5.4.4, we used Eq. (5.16) of Theorem 2 to expand the terms that are related to the viscosity, conductivity and species diffusivity. This method was adopted by

Gray (1975) and Beckermann and Viskanta (1993) also. This procedure leads to the introduction of effective coefficients to handle the corresponding morphological complexity. However, there is another method of derivation for treating these terms. This method is summarized below.

Using the macroscopic energy equations (5.34) and (5.35)as an example, the first terms on their right hand sides can be expanded according to the first equation of Theorem 2, Eq. (5.15). This method is adopted by Whitaker (1967) and Poirier (1990),

$$\overline{k_l \nabla T_l} = k_l \nabla g_l \overline{T_l}^l + k_l \frac{1}{dV} \int_{dA_k} T_l \boldsymbol{n}_l da \tag{5.56}$$

and

$$\overline{k_s \nabla T_s} = k_s \nabla g_s \overline{T_s}^s + k_s \frac{1}{dV} \int_{dA_k} T_s \boldsymbol{n}_s da \tag{5.57}$$

Considering the continuous distribution of temperature over the liquid and solid phase boundary, i.e. $T_l = T_s$, and the relation between the unit normal, i.e. $\boldsymbol{n}_l = -\boldsymbol{n}_s$, the two integral terms from Eq. (5.56) and (5.57) will cancel each other when they are added, resulting in

$$\overline{k_l \nabla T_l} + \overline{k_s \nabla T_s} = k_l \nabla g_l \overline{T_l}^l + k_s \nabla g_s \overline{T_s}^s \tag{5.58}$$

In the above, no effective conductivity is introduced, but g_l and g_s appear within the spatial derivatives. The previous method with effective conductivity yields

$$\overline{k_l \nabla T_l} + \overline{k_s \nabla T_s} = k_l^* g_l \nabla \overline{T_l}^l + k_s^* g_s \nabla \overline{T_s}^s \tag{5.59}$$

with g_l and g_s appearing outside the spatial derivatives. Eq. (5.58) can be expanded with respect to the spatial derivative to yield

$$\overline{k_l \nabla T_l} + \overline{k_s \nabla T_s} = k_l \left(g_l \nabla \overline{T_l}^l + \overline{T_l}^l \nabla g_l \right) + k_s \left(g_s \nabla \overline{T_s}^s + \overline{T_s}^s \nabla g_s \right) \tag{5.60}$$

Comparing it with Eq. (5.59), it can be seen that

$$k_l^* = k_l\left\{1 + \left(\frac{\nabla g_l}{g_l}\right)\left[\frac{\overline{T_l}^l}{\nabla \overline{T_l}^l}\right]\right\} \quad \text{and} \quad k_s^* = k_s\left\{1 + \left(\frac{\nabla g_s}{g_s}\right)\left(\frac{\overline{T_s}^s}{\nabla \overline{T_s}^s}\right)\right\} \quad (5.61)$$

The same derivation holds true for the treatment of the diffusivity terms in species and momentum transport equations. However in the species transport process, in general there is a jump condition of species concentration over the solid/liquid interface, i.e. $C_l \neq C_s$. The corresponding surface integrations shown in Eq. (5.56) or (5.57) will not cancel each other; thus the effective diffusivity of species as a function of microscopic complexity still has to be introduced.

5.4.6 Special Comment on Momentum Equation

Investigations on the formulation of the macroscopic momentum equation are abundant in the literature because of its wide application in porous media problems and two–phase flows (Drew 1983). Most formulations eventually reduce the liquid momentum equation to the form of Darcy's law, or may include an additional term to account for inertial effects. Then the solution of the momentum equation is in essence transferred into a problem of deciding the permeability that is required by Darcy's law.

While the measurement of permeability for flows with low liquid volume fraction or isotropic porous structure is well established, the study of the permeability of flow through anisotropic porous media or flow with high liquid volume fraction is difficult experimentally. Numerical or theoretical efforts have been combined with experimental evidence to tackle this problem. For example, Ochoa–Tapia and Whitaker (1995 a an b) developed a method to continuously connect the velocity boundary between a porous media and a homogeneous fluid. Ghaddar (1995) developed a parallel computational method to compute the permeability of a randomly distributed array. Bhat et al. (1995 a and b) numerically computed the permeability at high volume fraction of liquid that merge with the empirical data at the lower volume fraction.

In materials solidification, Darcy's law is only applicable when the solid phase is stationary, and the fluid moves with a sufficiently low velocity. In traditional porous media flow, the porous media is assumed to be a fixed structure. During solidification process, however, the morphology of dendrites varies in space and time, thus the description of permeability in solidification modeling is more challenging. It is also noticed that if solid particles are dispersed into the liquid and moves with it, then Darcy's law no longer applies. In this case, one has to directly apply the general form of macroscopic equation of momentum, i.e. Eq. (5.55). Voller et al. (1989) gave an illustration of this application. Nevertheless, in the following, we present a derivation based on Darcy's treatment, starting from the liquid momentum equation (5.50), which can also be written as

$$\frac{\partial}{\partial t}(\varrho_l g_l \overline{V_l}^l) + \nabla \cdot (\varrho_l g_l \overline{V_l}^l \overline{V_l}^l) = -\nabla(g_l \overline{P_l}^l) + \nabla \cdot \left[\overline{\mu_l \nabla V_l} + \overline{\mu_l (\nabla V_l)^t}\right] + I_l^D + I_l^Q + I_l^I + \overline{\boldsymbol{b}_l} + g_l \varrho_l \boldsymbol{g} \quad (5.62)$$

where I_l^D represents the microscopic deviation momentum flux, I_l^I represents the interfacial stresses, and I_l^Q represents the interfacial momentum transfer due to phase change.

As only the liquid phase is considered here, all these terms need to be modeled in detail as discussed in Drew (1983), Ganesan and Poirier (1990), Slattery (1967) and Beckermann and Viskanta (1993). Discrepancies in the interpretation of different terms may arise from different derivations. Nevertheless, they can all eventually be reduced to the same form, i.e. Darcy's law, after making appropriate assumptions. For example, if I_l^D is interpreted as the interfacial stress of a combination of "viscous drag" and "form drag", and assumed to be dependent on the relative mass averaged velocity between the liquid and the solid, it can be written as (Whitaker 1967, Ganesan and Poirier 1990)

$$I_l^I = -\mu \Gamma (V_l - V_s)$$

where Γ is a resistance coefficient which is a function of the morphology of the solid in the mushy zone.

Furthermore, by assuming that the momentum exchange caused by volume change

during phase change is negligible, i.e. $I_l^Q = 0$, and neglecting the momentum microscopic deviation term, i.e. $I_l^D = 0$, Eq. (5.62) then yields

$$\frac{\partial}{\partial t}(\varrho_l g_l \overline{V}_l^l) + \nabla \cdot (\varrho_l g_l \overline{V}_l^l \overline{V}_l^l) = -\nabla(g_l \overline{P}_l^l) + g_l \varrho_l \boldsymbol{g} + \nabla \cdot \left[\overline{\mu \nabla (g_l V_l^l)} + \overline{\mu \nabla (g_l V_l^l)^T}\right] - \mu \Gamma \cdot (\overline{V}_l^l - \overline{V}_s^s) \tag{5.63}$$

In addition, by assuming (a) steady and slow flow, i.e. $\overline{V}_l^l \to 0$, and hence the inertial term can be neglected; (b) the volume function of liquid g_l is uniform and constant; and (c) the forces of the liquid–liquid interactions are negligibly small, Eq. (5.63) then becomes

$$\overline{V}_l^l = -\frac{g_l^2 \Gamma}{\mu}[\nabla \overline{P}_l^l - \varrho_l \boldsymbol{g}] \tag{5.64}$$

which is Darcy's law with an additional body force for approximating the velocity in the mush zone.

5.5 Mixture Approach

From the above derivation, it can be seen that by the volume averaging approach, the macroscopic equations are rigorously derived from the exact microscopic equations. If appropriate relations between the macro–micro scales are given, the phase change process can be accurately modeled. While in the mixture approach, as the validity of certain continuum relations on a macroscopic scale has to be first assumed, no direct connection has been established in the literature with regard to the microscopic characteristics. This approach applies the conservation law of certain quantity Φ_k directly within the averaging volume dV, and is expressed as a balance of the net outflow by convection, diffusion, and volumetric production, i.e.

$$\frac{\partial}{\partial t}\int_{dV} \varrho_k \Phi_k dV_k + \int_{dA} (\varrho_k V_k \Phi_k) \cdot \boldsymbol{n} dA_k = \int_{dA} -\boldsymbol{J}_k \cdot \boldsymbol{n} dA_k + \int_{dV} S_k dV_k \tag{5.65}$$

where $\boldsymbol{n}$ is the outward unit normal to the surface, $\boldsymbol{J}_k$ is a surface flux vector and S_k is a volumetric source term which includes production or annihilation of Φ_k (Incropera and

Bennon 1987a). When g_k is assumed continuous, the integrands of above equations are continuous and differentiable functions, and the integral theorem of Leibnitz and Gauss can be applied. Furthermore, as the averaging control volume is arbitrary, the above equation can then be expressed in differential form as

$$\frac{\partial}{\partial t}(\varrho_k g_k \Phi_k) + \nabla \cdot (\varrho_k g_k V_k \Phi_k) = -\nabla \cdot (g_k J_k) + g_k S_k \qquad (5.66)$$

where Φ_k equals 1, V_k, H_k and C_k for mass, momentum, energy and species equations, respectively. By applying this equation to different phases in the averaging control volume dV and then adding them, the so–called macroscopic continuum mixture equations by the mixture approach result.

5.6 Closure

In this chapter, the macroscopic transport equations are systematically derived from the microscopic continuum equations via a volume averaging approach. These equations can be applied to solve a variety of multi–phase problems including alloy solidification, in which the coupled effects of fluid flow, heat transfer as well as species transport are present. In this effort, the formulation of microscopic deviation terms, which arise from the averaging procedure and have been neglected in the literature, have been addressed via an approach analogous to the turbulence modeling. By the current mathematical formulations of macroscopic transport equations, coupling between complex morphologies at the microscopic level and transport phenomena at the macroscopic level can be established via appropriate constructions of effective coefficients of diffusivity and microscopic deviation terms.

CHAPTER 6
NUMERICAL SIMULATION OF COLUMNAR SOLIDIFICATION OF BINARY ALLOYS

In this chapter, the macroscopic transport equations derived in the previous chapter are applied to a special case of columnar solidification of binary liquid–solid alloys. In order to accomplish this, simplified transport equations are obtained from the general macroscopic transport equations based on assumptions related to the characteristics of columnar solidification of binary mixture. Then, corresponding numerical techniques for the solutions of governing equations and implementations of phase diagram are illustrated. Finally, numerical results are discussed and compared with experimental observations.

6.1 The Simplification of Transport Equations

Several additional assumptions have been made to simplify the governing equations for the columnar solidification of binary alloys. They are listed in Table 6.1. Assumption 6 is made because in columnar solidification, the solid phase is a rigid region that is fixed to a cooled wall, therefore, the velocity in the solid region is zero. Assumption 7 can be justified by the high thermal diffusivity of metal alloys and the presence of creeping flow in the columnar mushy zone (Beckermann and Viskanta 1993). Assumption 8 is typically good for the liquid within the interdendritic meshwork, but it produces errors at the dendritic tips due to solute undercooling (Flood and Hunt 1987, Huppert 1990). The main drawback of this assumption is that a kinetic law for the movement of the dendritic tips can not be introduced (Rappaz 1989). But this effect can now be accounted for with our consideration of microscopic deviation terms. Assumption 9 applies to almost all solidification process because the species (solute) diffusion in the solid is much smaller than that in the liquid, i.e.

Table 6.1 Assumptions for the Modeling of Columnar Solidification of Binary Alloys

Assumption 6:

$$\overline{V_s}^s = \overline{V_s} = V_s = 0$$

Assumption 7: All phases in the averaging volume are in thermal equilibrium, i.e.

$$\overline{T_s}^s = \overline{T_l}^l = T$$

Assumption 8: The liquid in the averaged volume is solutally well mixed, i.e.

$$\overline{C_l}^l = C_l$$

and, at the liquid–solid interface, the relation of solidus and liquidus concentration is given by the phase diagram.

Assumption 9: The species flux in the solid region is neglected, i.e.

$$D_s = 0$$

$D_s << D_l$. However, this assumption does not necessarily imply that the species (solute) distribution in the solid of the averaged volume is uniform. In fact, species (solute) concentration in the solid phase is usually assumed in the literature with either complete or no diffusion (Level Rule or Scheil) models (Kurz and Fisher(1989)), which will be explained in detail later.

With these assumptions, the macroscopic transport equations of mass, heat and species can then be simplified from Eq. (5.33), (5.43) and (5.49), respectively, and yield

$$\frac{\partial\left(g_l\varrho_l + g_s\varrho_s\right)}{\partial t} + \nabla\cdot\left(g_l\varrho_l\overline{V_l}^l\right) = 0 \tag{6.1}$$

$$\frac{\partial\left(g_l\varrho_l\overline{H_l}^l + g_s\varrho_s\overline{H_s}^s\right)}{\partial t} + \nabla\cdot\left(g_l\varrho_l\overline{H_l}^l\overline{V_l}^l\right) = \nabla\cdot\left[g_l\left(k_l^* + k_l^D\right) + g_s k_s^*\right]\nabla T \tag{6.2}$$

$$\frac{\partial\left(g_l\varrho_l\overline{C_l}^l + g_s\varrho_s\overline{C_s}^s\right)}{\partial t} + \nabla\cdot\left(g_l\varrho_l\overline{C_l}^l\overline{V_l}^l\right) = \nabla\cdot\left[g_l\varrho_l\left(D_l^* + D_l^D\right)\nabla\overline{C_l}^l\right] \tag{6.3}$$

Further simplification of momentum equation of Eq. (5.55) is rather difficult, because the effective viscosity in the mushy region can not be estimated directly. For columnar

solidification, in which the solid region is also fixed, we will adopt Darcy's approximation. The momentum equation can then be obtained from Eq. (5.63) as

$$\frac{\partial}{\partial t}(\varrho_l g_l \overline{V}_l^l) + \nabla \cdot (\varrho_l g_l \overline{V}_l^l \overline{V}_l^l) = -\nabla(g_l \overline{P}_l^l) + g_l \varrho_l \boldsymbol{g} + \nabla \cdot \left[\overline{\mu \nabla (g_l \overline{V}_l^l)} + \overline{\mu \nabla (g_l \overline{V}_l^l)^T}\right] - \mu \Gamma \overline{V}_l^l \tag{6.4}$$

where Γ is the resistance coefficient. Adopting the Kozeny–Carman equation for flow in a porous media (Bennon and Incropera 1987b), it yields that

$$\Gamma = K_0 \frac{(1 - g_l)^2}{g_l^3} \tag{6.5}$$

where K_0 is a permeability constant depending on the morphology of the mushy zone during phase change.

Furthermore, we define that

$$\varrho = \varrho_s g_s + \varrho_l g_l \qquad \varrho f_s = \varrho_s g_s \qquad \varrho f_l = \varrho_l g_l \tag{6.6}$$

and

$$\boldsymbol{V} = f_l \overline{V}_l^l \qquad \varrho_l g_l \overline{V}_l^l = \varrho f_l \overline{V}_l^l = \varrho \boldsymbol{V} \tag{6.7}$$

where ϱ is the averaged density and $\boldsymbol{V}$ is the averaged velocity in the averaging volume dV, f_s and f_l are mass fractions of solid and liquid, respectively, and $f_l + f_s = 1$ for binary alloys with no pores. Then Eq. (6.1) of mass conservation becomes

$$\frac{\partial \varrho}{\partial t} + \nabla \cdot (\varrho \boldsymbol{V}) = \boldsymbol{0} \tag{6.8}$$

and Eq. (6.4) for momentum conservation becomes

$$\frac{\partial}{\partial t}(\varrho \boldsymbol{V}) + \nabla \cdot (\varrho \boldsymbol{g} \boldsymbol{V} \boldsymbol{V}) = -\nabla(P) + \varrho \boldsymbol{g} + \nabla \cdot \left[\mu \nabla \boldsymbol{V} + \mu \nabla \boldsymbol{V}^T\right] - \mu K_0 \frac{(1 - g_l)^2}{g_l^3} \boldsymbol{V} \tag{6.9}$$

This equation reveals that, in the pure solid, when $g_l = 0$ and $\Gamma \to \infty$, it gives $\boldsymbol{V} = 0$; in

the pure liquid, $g_l = 1$ and $\Gamma \to 0$, it reduces to the classical Navier–Stokes equations; while in the mushy zone, it incorporates the Darcy's law for porous media flow.

For the energy conservation equation, we define that

$$\Delta H = \overline{H_l}^l - \overline{H_s}^s \tag{6.10}$$

where $\overline{H_l}^l$ is the averaged total enthalpy of the interdendritic liquid. $\overline{H_s}^s$ is the averaged total enthalpy of the solid and ΔH is an effective latent heat, which varies during solidification of alloys (Poirier et al. 1988). Substituting $\overline{H_l}^l$ by $\overline{H_s}^s + \Delta H$ into the time dependent term of Eq. (6.2) of energy conservation, and using the definition of Eqs. (6.6) and (6.7), Eq. (6.2) can then be cast into the following form

$$\frac{\partial}{\partial t}(\varrho \overline{H_s}^s + \varrho f_l \Delta H) + \nabla \cdot \left[\varrho V\left(\overline{H_l}^s + \Delta H\right)\right] = \nabla \cdot \left[\left(g_l k_l^* + g_s k_s^*\right) + g_l k_l^D\right]\nabla T \tag{6.11}$$

Since $\overline{H_s}^s = CpT$, where Cp is a function of both temperature and composition (Poirier et al. 1988), the energy equation can then be further cast as

$$\frac{\partial}{\partial t}(\varrho CpT) + \nabla \cdot (\varrho CpTV) = \nabla \cdot \left[\left(g_l k_l^* + g_s k_s^*\right) + g_l k_l^D\right]\nabla T - \left[\frac{\partial}{\partial t}(\varrho f_l \Delta H) + \nabla \cdot (\varrho V \Delta H)\right] \tag{6.12}$$

For the solute (species) conservation equation, the extent of diffusion in the local solid of a control volume dV must be estimated in order to account for the partitioning of the solute between the local dendritic solid and the interdendritic liquid (Poirier et al. 1991). Two models, that of complete diffusion and no diffusion, also referred in the literature as Level Rule model and Scheil model, respectively, are commonly used. The complete diffusion model assumes that the solute concentrations in both the local solid portion (C_s) and in the local liquid portion (C_l) within an averaging volume dV are completely uniform. On the other hand, the no diffusion model assumes that no diffusion takes place in the solid while

the solute concentration in the local liquid (C_l) is uniform.

Now let us introduce

$$\overline{C} = f_l \overline{C}_l^{\,l} + f_s \overline{C}_s^{\,s} \tag{6.13}$$

or

$$f_l = \frac{\overline{C} - \overline{C}_s^{\,s}}{\overline{C}_l^{\,l} - \overline{C}_s^{\,s}} \tag{6.14}$$

where $\overline{C}$ is the averaged weight percentage of solute concentration in the averaged volume dV.

According to the definition of Eq. (6.13), Eq. (6.3) then becomes

$$\frac{\partial}{\partial t}(\varrho \overline{C}) + \nabla \cdot (\varrho \overline{C}_l^{\,l} V) = \nabla \cdot \left[\varrho f_l \left(D_l^* + D_l^D\right) \nabla \overline{C}_l^{\,l}\right] \tag{6.15}$$

Replacing $\overline{C}_l^{\,l}$ by $\overline{C}_l^{\,l} + \overline{C} - \overline{C}$, Eq. (6.15) can further be written as

$$\begin{aligned} \frac{\partial}{\partial t}(\varrho \overline{C}) + \nabla \cdot (\varrho \overline{C} V) \;=\; & \nabla \cdot \left[\varrho f_l \left(D_l^* + D_l^D\right) \nabla \overline{C}\right] + \\ & \left\{\nabla \cdot \left[\varrho (\overline{C} - \overline{C}_l^{\,l}) V\right] + \nabla \cdot \left[\varrho f_l \left(D_l^* + D_l^D\right) \nabla (\overline{C}_l^{\,l} - \overline{C})\right]\right\} \end{aligned} \tag{6.16}$$

This form of solute equation has the advantage of allowing implementation of different microscopic diffusion models, avoiding the necessity of changing the form of governing equations every time the microscopic diffusion model is changed. For example, Voller et al. (1989) and Poirier et al. (1991) have to change their solute equations when their diffusion models are changed. In order to do this, they have to first represent $\overline{C}_l^{\,l}$ in terms of $\overline{C}$ according to the definition of Eq. (6.13), substitute it back into Eq. (6.15), and then apply mathematical operations such as Newton–Leibnz's rule to regroup the equation. This way, different diffusion models yield different forms of governing equations, which makes numerical implementation rather difficult. With the present way of deriving the solute equation, however, any types of diffusion model can be accounted for by Eq. (6.16). The effect of diffusion models comes into play via the different constructions of Eq. (6.14).

Equations (6.8), (6.9), (6.12) and (6.16) are then the final forms of our simplified governing equations for the modeling of columnar solidification of binary alloys. Fluid fraction of f_l can be determined from Eq. (6.14), where the phase diagram comes into play. However, to close the problem, the constitutive equations of the microscopic deviation and effective coefficients included in these equations have also to be supplemented as a function of microscopic transport characteristics. According to previous discussions, the microscopic deviation coefficients of diffusivity are approximated by

$$k_l^D = 2\varrho CpK \quad \text{and} \quad D_l^D = 2\varrho K \tag{6.17}$$

where K is given by Eq. (5.27).

For the purpose of showing the basic approach of incorporating the microscopic complexities into the macroscopic transport equations, the formulations of effective coefficients of diffusivity adopted here are simple empirical models as discussed in the last chapter (Speich and Fisher 1966). They are given in the following as

$$k_l^* = k_l(1 - g_l + g_l^2), \quad k_s^* = k_s(1 - g_s + g_s^2) \quad \text{and} \quad D_l^* = D_l(1 - g_l + g_l^2) \tag{6.18}$$

It is mentioned that the accurate construction of these constitutive equations of microscopic deviation or effective coefficients requires extensive experimental investigations or direct numerical simulations of morphological evolution (Rappaz 1989).

6.2 Implementation of the Numerical Procedure

6.2.1 Solution Procedure

The calculation of the coupled effect of mass, momentum, heat and solute transport is a transient process. The following steps have been developed in the current study to accomplish this process.

(1) Give the initial conditions at t=0, i.e., initial values of V, T, $\overline{C}$, f_l and $\overline{C}_l^l$;

(2) Go to t=t+Δt;

(3) Solve V, T and $\overline{C}$ according to Eqs. (6.8), (6.9), (6.12) and (6.16);

(4) Update f_l according to the newly obtained T and $\overline{C}$ via Eq. (6.14);

(5) With the newly updated f_l and $\overline{C}_l^l$ to recalculate the source term of Eq. (6.16), go back to step (3) and repeat the procedure. If the solution is converged, then go to step (6);

(6) Go back to step (2) for the next time step;

In this procedure, step 4 is where the phase diagram comes into play and where the energy and solute equations are coupled. Different microscopic diffusion models will lead to different expressions of f_l. This issue is discussed in more detail next.

6.2.2 Implementation of Diffusion Model

Most of the numerical models reported in the literature only consider the complete diffusion model (Prescott and Incropera 1994, Beckermann and Viskanta 1993, Bennon and Incropera 1987a, Prakash and Voller 1989, Viskanta 1990). Voller et al. (1989) derived the solute equation assuming that no diffusion takes place in the local solid. However, their numerical updating method for f_l seems to still adopt the one based on the complete diffusion model and is inconsistent with the governing equation. Poirier et al. (1991) took full account of both models and derived the corresponding governing equations, but their calculation is quite limited and they presented only qualitative results. They assume the cooling speed is known *a priori* such that they can define a new coordinate system z' that moves with the solidus interface. The boundary condition at z'=0 is then given by the eutectic temperature and eutectic solute composition. In addition, their computation is only one dimensional. Since these calculations are based on the solute transport equations derived via different models and inadequate numerical resolution, it is difficult to separate physical and numerical uncertainties.

In the current study, for the complete diffusion model, as it is assumed that the solute concentrations of the local solid (C_s) and of the local liquid (C_l) in a control volume dV are completely uniform, i.e.

$$\overline{C} = f_l C_l + f_s C_s \tag{6.19}$$

Then combining Eq. (6.14) and (6.19), we can directly obtain that

$$f_l = \frac{\overline{C} - C_s}{C_l - C_s} \tag{6.20}$$

wbere C_s and C_l can be decided by phase diagram as shown schematically in Fig. 6.1 when temperature T is given. The mushy zone can then be identified in the following ways. If $\overline{C} < C_s$ and thus $f_l<0$, for example at point A, then we specify that $f_l=0$ and know that A is in the solid region; if $\overline{C} > C_l$ and thus $f_l > 1$, for example at point B, then we let $f_l=1$ and know that B is in the liquid zone; otherwise, if $0<f_l<1$, the corresponding point P, must be located in the mushy zone. With this approach of updating f_l, no assumption is necessary for the liquidus and solidus curves to be straight lines, neither it is necessary that the constant partition coefficient k_p is specified. As long as the liquidus or solidus curves are given in the form of a set of data or certain curve fitting functions, C_s and C_l can be decided with a given temperature.

For the no diffusion model, it is assumed that the solute concentration of the local solid (C_s) is not diffusive, while the solute concentration in the local liquid (C_l) is uniform. Then it follows that

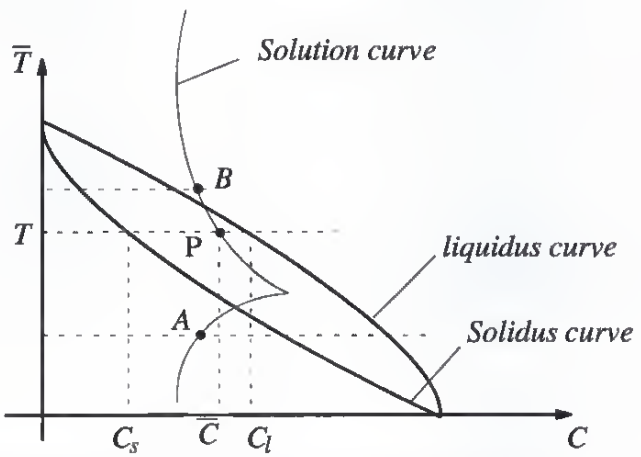

Figure 6.1. Schematic of the calculation of fluid fraction and mushy region

$$\overline{C} = \int_0^{f_s} C_s(\eta)d\eta + f_l C_l \tag{6.21}$$

where $C_s(\eta)$ is an unknown function, in which η represents the solidus volume fraction. In this case f_l cannot be obtained directly from Eq. (6.14). However, we can always approximate the function $C_s(\eta)$ by curve fitting. For example, if we want to update f_l of a designated averaging volume, we can record the solute concentration at the instant when the material in that volume starts to solidify, i.e. $C_s(0)$ at $f_s = 0$ from the previous calculations. At the current time instant, the solidus concentration at the solid/liquid interface, which is in equilibrium with the liquidus concentration C_l, is given by $C_s^*(f_s)$. Then by assuming a linear variation of $C_s(\eta)$ as a function of η, it can be shown that

$$\int_0^{f_s} C_s(\eta)d\eta = \frac{[C_s(0) + C_s(f_s^*)]}{2} \tag{6.22}$$

So we can still update f_l by the expression

$$f_l = \frac{\overline{C} - C_s^*}{C_l - C_s^*}$$

which is in the same form as Eq. (6.20), except that

$$C_s^* = \frac{[C_s(0) + C_s^*(f_s)]}{2} \tag{6.23}$$

which is no longer the real equilibrium solidus concentration that corresponds to the equilibrium temperature *T*. We call it the effective solidus concentration which accounts for the non–uniform distribution of solidus concentration in the local control volume.

This approach of updating f_l is flexible and easy to modify. For example, if we want to obtain more accurate approximation of $C_s(\eta)$ as a function of solidus fraction η, we just need to store one more point calculated at previous time instant, i.e., $C_s(f_{s1})$ at $f_s = f_{s1}$. By assuming a quadratic function of $C_s(\eta)$, C_s^* can thus be expressed in terms of $C_s(0)$, $C_s(f_{s1})$

and $C_s^*(f_s)$. In addition, different liquidus diffusion models, which are necessary near the dendritic tip region where liquidus solute gradients play an important role, can also be accounted for by the current approach.

6.3 Numerical Simulation of Solidification Process of NH4Cl–H2O Mixture

In this section, we present the numerical result of a solidification process of aqueous ammonium chloride (NH_4Cl–H_2O) and compare it with experimental observations. It is mentioned that, at this stage, our computation is still preliminary because of the lack of data on the detailed microstructure of NH_4Cl–H_2O mixture. Therefore, the following numerical computations are conducted only for the case with $k_l^D = 0$, $D_l^D = 0$, $k_l^* = k_l$, $k_s^* = k_s$, and $D_l^* = D_l$ in Eqs (6.17) and (6.18), i.e., the morphological complexities are neglected in the present effort.

6.3.1 System Set–Up

First, the thermal properties of NH_4Cl–H_2O binary solution is listed in Table 6.3. This solution is selected for the current study for the following reasons (Christenson and Incropera 1988a)

- It is semitransparent, which facilitates flow visualization;
- It is similar to liquid metal solidification in terms of dendritic growth of the solid phase;
- Its thermophysical property data are available, which facilitates numerical simulation, and
- It has the flexibility allowing for experiment measurement over a wide range of conditions.

The equilibrium phase diagram for aqueous ammonium chloride solution, which has a eutectic temperature and composition (water mass fraction) of $T_e = -15.4^oC$ and $f_e = 80.3\%$, is shown in Fig. 6.2. Figure 6.3 shows the schematic of the experimental

Table 6.3 Thermophysical Properties of NH4Cl–H2O

	Solid	Liquid
Specific heat (J kg^{-1} K^{-1})	1870	3249
Thermal conductivity (W m^{-1} K^{-1})	0.393	0.468
Density (kg m^{-3})	1078	1078
Diffusion coefficient (m^2 s^{-1})	–	4.8×10^{-9}
Viscosity (kg m^{-1} s^{-1})	–	1.3×10^{-3}
Latent heat of fusion, L (J kg–1)		3.138×10^{5}
Permeability coefficient, K_0 (m^2)		5.56×10^{-11}
Thermal expansion coefficient, β_T (K^{-1})		3.832×10^{-4}
Solutal expansion coefficient, β_S		0.257
Eutectic temperature T_e (K)		257.75
Eutectic composition, f_e		0.803
NH4Cl melting point, T_m (K)		633.59
Equilibrium partition ratio, k_P		0.30

set–up (Nishimura et al. 1994). This is a rectangular test cell with inner dimensions of 37mm in length, 50mm in height and 30mm in width. The initial temperature of the solution is $T_i = 25C$ and the initial composition is $C_i = 0.75$ wt% water. At t=0, the right wall temperature is dropped to $T_{cold} = -14.4C$. Under these experimental conditions, dendritic crystals of NH_4Cl–H_2O are only formed and a mushy zone comprises a mixed region of liquid and crystals since the cold wall is above the eutectic temperature T_e=*–15.4 C*. In the present computation, we have used 75x101 grid points, a time interval of $\Delta t = 1s$ and run the transient solidification process up to 10 minutes.

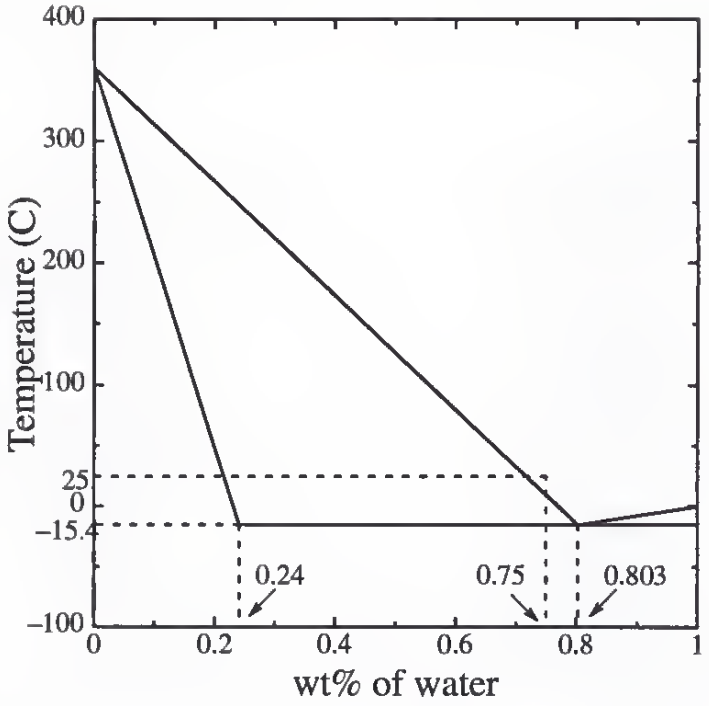

Figure 6.2. Phase diagram of the NH_4Cl–H_2O solution.

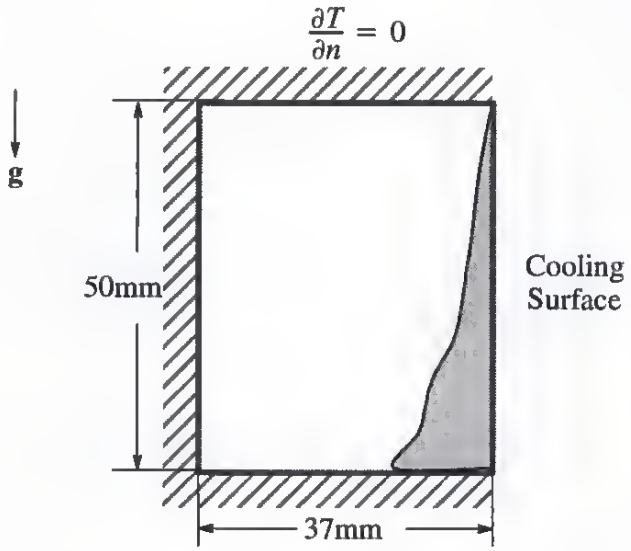

Figure 6.3. Schematic of experimental set–up.

6.3.2 Numerical Result and Comparison with Experimental Observations

Figure 6.4 shows the streamfunction and isotherms obtained for different time instants. It can be observed that in the initial cooling process (t=2 min), heat transfer is the only transport process and a large clockwise circulation dominates due to thermal convection. Crystallization starts to occur at the lower right corner on the cold wall, and a small volume of water–rich fluid is released. As the cooling progresses, the cold water–rich fluid, released by the crystal formation, rises up through the mushy zone, forms a finger shape pattern heading downward (t=4 min). At t=6 min, this water–rich solute volume is pushed back by thermal convection and continues to rise up. At t=8 min, it penetrates into the hot liquid and forms a sharp density front near the top of the cavity, marking the beginning of the compositional stratification. The fluid below the density front is dominated by thermal convection, but this is damped by the compositional stratification in the liquid above it. When the upper layer above the density front reaches a certain thickness, a clockwise circulation formed inside the density front, moves downwards and double diffusive cells are formed above the density front (t=10 min). It is also observed in Fig. 6.4 that isotherms revealed by liquid crystals are tilted downwards when the fluid in the diffusive interface is stagnant and the isotherms are tilted upwards when a strong clockwise circulation is observed.

Features of double diffusive convection cells during solidification can be further described as follows. A thin diffusive interface exists between cells and each cell behaves as a separate cell as shown in Fig. 6.4 at t=8 min. These cells are generated in a sequential fashion, rather than simultaneously. The diffusive interface which changes into a new cell is initially stagnant. As the thickness of the interface reaches a certain size, the fluid in the interface begins to rotate in the same direction as old cells. It is expected that as time evolves, the density front will move downwards with time due to the release of the water–rich fluid. Each convection cell generated from a diffusive interface will then grow up and move downwards with progressing solidification.

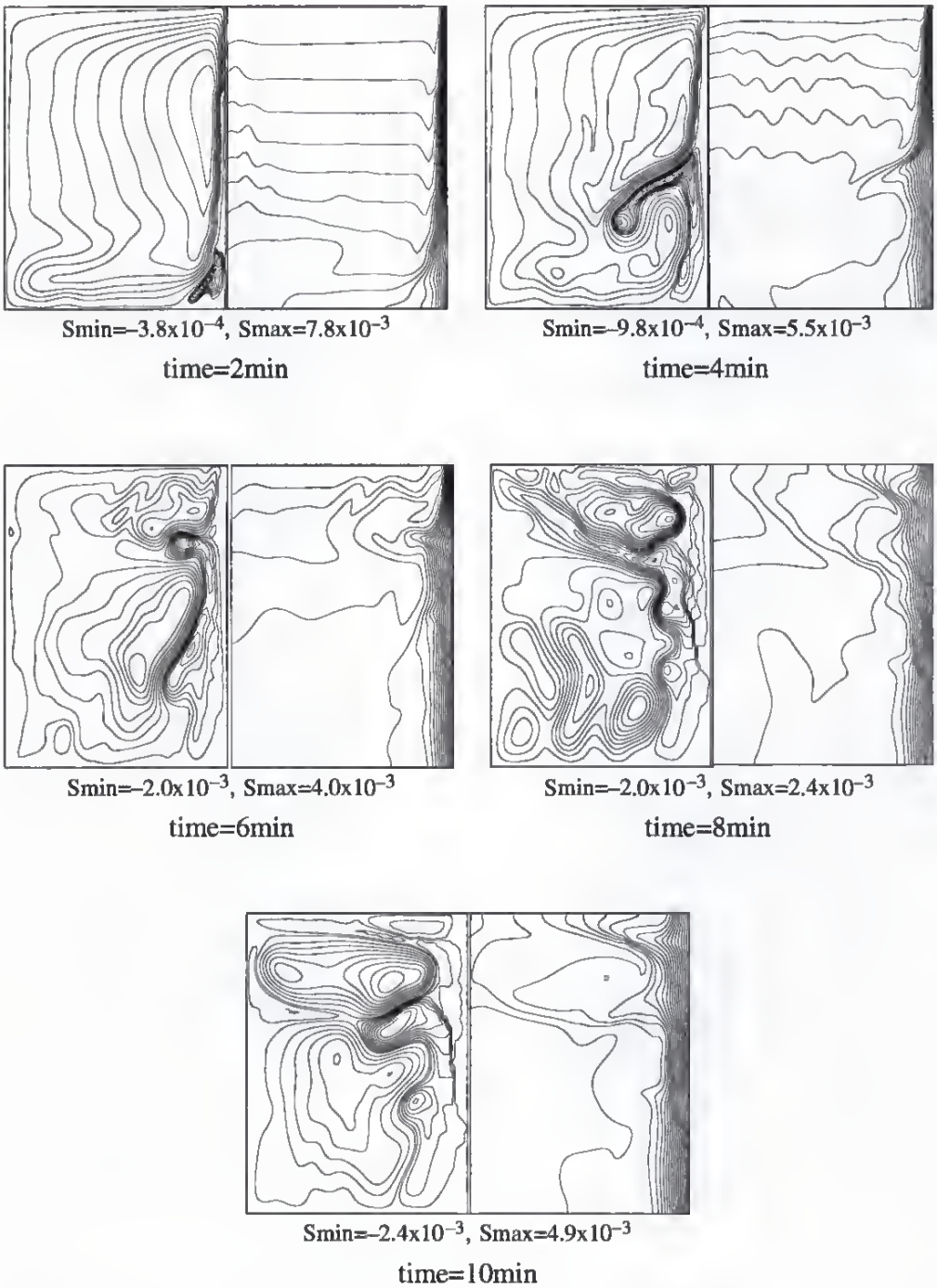

Figure 6.4. Streamfunction (on the left) and isotherms (on the right) of the solidification process of NH_4Cl–H_2O mixture at different time instants.

Figure 6.5 shows the concentration profiles along the vertical central line of the rectangular domain at different time instants. By comparing with Fig. 6.4, it is found that within each convection cell, the solute field is nearly uniform, while solute levels change abruptly across the interface, which is exemplified by an abrupt jump of concentration profiles across diffusive interfaces at t=8 min and t=10 min. This effect is caused by the separation between convection cells and the diffusive interface. So solute diffusion is dominant in the diffusive interface between two convective cells with almost vertical concentration gradient as shown in Fig. 6.5.

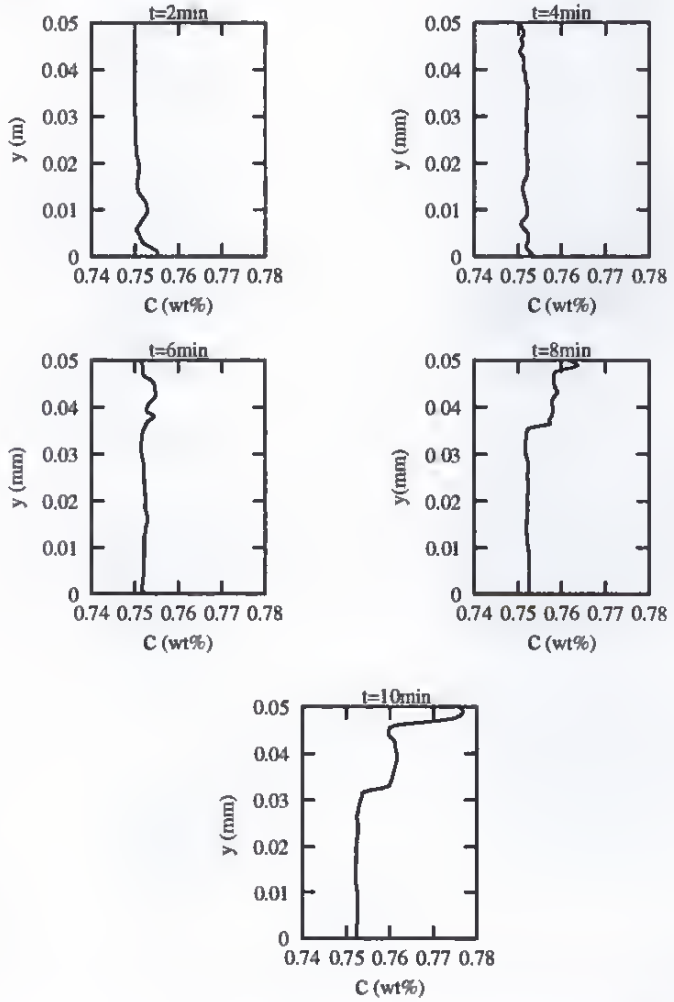

Figure 6.5. Concentration profiles along the rectangular centerline at different time instants.

The double diffusive phenomena we have predicted in the current study is in qualitative agreement with that observed by Nishimura et al. (1994). These agreements include the formation of the solute diffusive layers, generation and growth of convection cells in a sequential fashion, and isotherm distributions. However, there is a main discrepancy in that, the time instant when similar double diffusive pattern appears recorded by experiment is substantially different from that predicted by the current computation. For example, solution characteristics of our modeling result at t=8 min is comparable with that of experimental observation at t=25 min, which is shown in Fig. 6.6 for the upper portion of the solidification domain. It has been shown that this type of double diffusive pattern in solidification is very sensitive to a small change of initial temperature conditions and initial solute composition (Christenson and Incropera 1988b). In addition, it is again mentioned here that, the current computation has not included the morphological complexities, whose incorporations are expected to provide more accurate results.

6.4 Closure

In this chapter, we have applied the macroscopic transport equations to the simulation of columnar solidification of binary alloys. A convenient form of solute transport equation

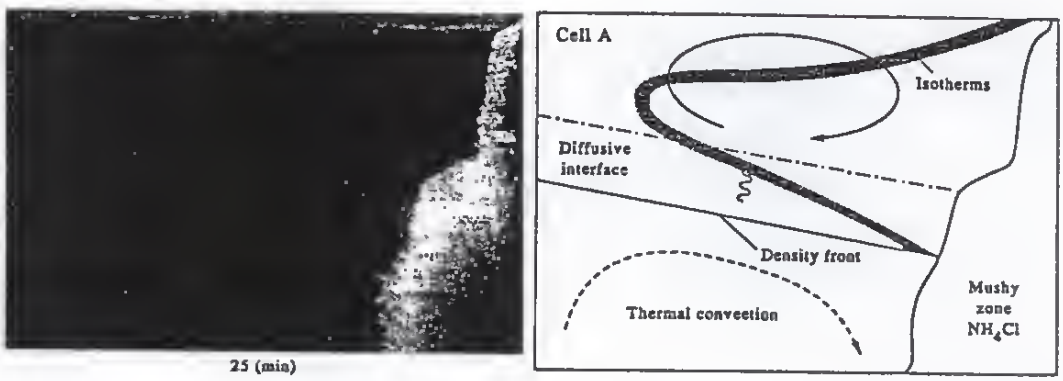

Figure 6.6. Visualization photograph of flow and temperature fields above the density front (Nishimura et al. 1994)

has been derived for the easy update of fluid fraction via the introduction of an effective solidus concentration. In the case of complete diffusion (Level Rule model), this effective solidus concentration is simply equal to the equilibrium solidus temperature that corresponds to the local temperature; in the case of zero solid diffusion (Scheil model), this effective solidus concentration is some weighed value between the local equilibrium solidus concentrations and its solidus concentration recorded from previous time instants.

The detailed double diffusive convection patterns induced by thermal and solutal gradients are captured by the current simulation for the solidification process of NH_4Cl–H_2O mixture. Phenomena of compositional stratification and convection cell generation in a sequential fashion are also revealed. While comparisons with experimental observations show qualitative agreement, further efforts addressing such issues as the incorporation of microscopic complexities into the macroscopic equations are important for achieving accurate numerical predictions.

CHAPTER 7
CONCLUSIONS

7.1 Summary of the Current Work

In this study, both modeling and simulation have been conducted for the single crystal growth of NiAl and CdTe in the vertical Bridgman system. The many physical complexities presented in this system, including all three heat transfer modes of conduction, convection and radiation, phase change, and variable materials properties, and geometrical complexities of the entire system consisting of the enclosure wall, encapsulated gas and the ampoule, have been considered. Accordingly, a two–level simulation has been performed to simultaneously achieve accuracy as well as computational economy. At the global level, the entire system consisting of the enclosure, the ampoule support and the ampoule is modeled. However, it is desirable to improve the grid resolution within the ampoule to capture the detailed characteristics of the melt/crystal interface. Thus, a refined ampoule simulation was performed using the solution from the global simulation as the boundary condition, enabling an accurate treatment of solidification dynamics within the ampoule, and heat transfer through the crystal.

To validate the current model, we have conducted the coordinated computations and experiments for the vertical Bridgman growth of NiAl crystal. Satisfactory agreement of the temperature profiles along the NiAl centerline and the ampoule outer wall was obtained between the experimental measurements and the numerical predictions, which indicates that the current model is accurate. Furthermore, detailed analysis of thermal conditions in the vertical Bridgman growth system for the NiAl single crystal reveals that the current design is reasonable, evidenced by the interface shape and the temperature gradient across the

interface. Variations in processing parameters have also been explored for process improvement. For example, we have shown that coating the ampoule outer wall with a high emissivity material, or decreasing the ampoule wall thickness, will both lead to an improvement of the interface conditions. We have also found in this study that the melt/solid interface temperature of NiAl at stoichiometric composition is around 1716 C, which is about 70 C higher than the melting temperature reported in the literature. Because the high melting temperature of NiAl is one of its strongest attributes, the accurate definition of the melting temperature is important and is worthy of more effort in the future.

In addition, we have also simulated the vertical Bridgman growth of CdTe crystal with two ampoule configurations, namely, flat base and semi–spherical base. It is found that both the flat base and the semi–spherical base configurations produce slightly concave solid–melt interface which is apparently undesirable for growing high quality CdTe crystal. The curvature of the melt/crystal interface seems to depend strongly on the variations in thermal conductivities between melt and crystal and also the sharpness of the thermal profile along the ampoule wall.

In the aspect of modeling and simulation of alloy solidification, the macroscopic transport equations are systematically derived upon the microscopic continuum equations via a volume averaging approach. These equations can be applied to solve variety of multi–phase problems including alloy solidification, in which the couped effects of fluid flow, heat transfer as well as species transport are present. In this effort, the formulation of microscopic deviation terms, which arise from the derivation procedure and have been neglected in the literature, have been specifically addressed via an analogous formulation of turbulent eddy viscosity. By the current mathematical formulations of macroscopic transport equations, the coupling between complex morphologies at the microscope and transport phenomena at the macroscope can be accomplished via appropriate constructions of effective coefficients of diffusivity and microscopic deviation terms.

These formulation derived have then been applied to the simulation of columnar

solidification of binary NH_4Cl–H_2O mixture. A convenient form of solute transport equation has been developed for the easy update of fluid fraction for any types of solute diffusion model in the solid or in the liquid at the microscope. The current numerical simulation can reveal the detailed double diffusive convection pattern induced by thermal and solutal gradients and capture such phenomena as compositional stratification and convection cell generation in a sequential fashion.

7.2 Future Work

Modeling of solidification is still a young area and quantitative simulation of practical solidification processes has just begun. There are many issues which await to be resolved in this interdisciplinary area. For example, radiation effect is an important heat transfer mode in any crystal growth devices. Sometimes it causes the strong radiation–melt interaction. However, most of the numerical modeling reported in the literature neglects this effect. In the current effort, we take into account of the effect by only employing a simple approximation of heat flux between the vertical heater and the ampoule outer wall. While this is reasonable for the NiAl system because the alumina ampoule is not transparent, but might cause inaccuracy for the CdTe system, in which the quartz ampoule wall is transparent and radiation heat might penetrate into the melt to influence the interface behavior there. There are also other situations when participating media of radiation are present, including such effects as emitting, absorbing and scattering radiation. So development of more comprehensive radiation model is necessary for the quantitative simulation of the heat transfer process in crystal growth devices.

In addition, convection effect, including its transition to turbulence, although is widely accepted as important in the material processing, is still not studied extensively up to date. Sources that cause convection effect in a crystal growth device are many. For example, the buoyancy–driven convection caused by solute and temperature dependence of the density, surface–tension gradients along melt/fluid menisci, forced convection introduced by the

motion of solid surfaces, crucible and crystal rotation, etc. The need for full numerical solutions that account for all these effects is clear. In the present, the thermal and solutal induced convection effects are considered only in the laminar regime. There are, however, in practice a lot of situations when the convection during solidification turns into turbulence depending on the properties of materials, processing conditions and design scales of materials processing devices. So numerical implementation of turbulent modeling is another area of concern in this field.

Finally, it is realized that the ultimate goal of modeling and simulation of solidification process is to connect the macroscopic processing conditions to the microscopic formations of microstructure for a purpose of manipulating material properties. However, at present, this linkage is quite incomplete although attention has been drawn. To circumvent this problem, an accurate and efficient micro–macroscopic modeling is essential. Future developments in the area of micro–macroscopic modeling of solidification should be made through a systematic comparison and coordinated corporation between numerical modeling and experimental work. While modeling of certain solidification process and phenomena on a single scale has matured to a considerable level of sophistication, the new challenge in the solidification modeling research is to concern with the development of coupling among disparate scales. Hence, there are still many research and development challenges to be met in the field of micro–macroscopic modeling of solidification.

REFERENCES

Beckermann C. and Viskanta R. (1993), "Mathematical Modeling of Transport Phenomena during Alloy Solidification," *Appl. Mech. Rev.*, **46**(1), 1–27.

Bennon W.D. and Incropera F. P. (1987a), "A Continuum Model for Momentum, Heat and Species Transport in Binary Solid–Liquid Phase Change Systems — I. Model Formulation," *Int. J. Heat Mass Transfer*, **30**(10), 2161–2170.

Bennon W.D. and Incropera F.P. (1987b), "A Continuum Model for Momentum, Heat and Species Transport in Binary Solid–Liquid Phase Change Systems—II. Application to Solidification in a Rectangular Cavity," *Int. J. Heat Mass Transfer*, **30**(10), 2171–2187.

Bird R.B., Steward W.E. and Lightfoot E.N. (1960), *Transport Phenomena*, John Wiley, New York, NY.

Bhat M.S., Poirier D.R. and Heinrich J.C. (1995a), "Permeability for Cross Flow through Columnar–Dendritic Alloys," *Metall. Trans. B*, **26B**, 1049–1056.

Bhat M.S., Poirier D.R. and Heinrich J.C. (1995b), "A Permeability Length Scale for Cross Flow through Model Structures, *Metall. Trans. B*, **26B**, 1091–1092.

Braaten M.E. and Shyy W. (1986), "A Study of Recirculating Flow Computation using Body–Fitted Coordinates: Consistency Aspects and Mesh Skewness," *Numer. Heat Transfer*, **9**, 559 – 574.

Brown R.A. (1988), "Theory of Transport Processes in Single Crystal Growth from the Melt," *A.I.Ch.E. J.*, **34**, 881–911.

Brunet P., Katty A., Schneider D., Tromson–Carli A. and Triboulet R. (1993), "Horizontal Bridgman Growth of Large High Quality $Cd_{1-y}Zn_yTe$ crystals," *Mat. Sci. Engng.*, **B16**, 44–47.

Chalmers B. (1964), *Principles of Solidification*, John Wiley & Sons, New York.

Christenson M.S. and Incropera F.P. (1989a), "Solidification of an Aqueous Ammonium Chloride Solution in a Rectangular Cavity—I. Experimental Study," *Int. J. Heat Mass Transfer*, **32**(1), 47–68.

Christenson M.S., Bennon W.D. and Incropera F.P. (1989b), "Solidification of an Aqueous Ammonium Chloride Solution in a Rectangular Cavity—II. Comparison of Predicted and Measured Results," *Int. J. Heat Mass Transfer*, **32**(1), 69–79.

Crank J. (1984), *Free and Moving Boundary Problem*, Oxford University Press, Oxford, U.K.

Darolia R. (1991), "NiAl Alloys for High–Temperature Structural Applications," *JOM* **March**, 44–49.

Drew D.A. (1983), "Mathematical Modeling of Two–Phase Flow," *Ann. Rev. Fluid Mech.*, 1983, **15**, 261–291.

Flood S.C. and Hunt J.D. (1987), "Columnar and Equiaxed Growth," *J. Crystal Growth*, **82**, 543–551.

Ganesan S. and Poirier D.R. (1990), "Conservation of Mass and Momentum for the Flow of Interdendritic Liquid during Solidification," *Metall. Trans. B*, **21B**, 173–181.

Germano M. (1992), "Turbulence: the Filtering Approach," *J. Fluid Mech.*, **238**, 325–336.

Ghaddar C.K. (1995), "On the Permeability of Unidirectional Fibrous Media: A Parallel Computational Approach," *Phys. Fluids*, **7**(11), 2563–2586.

Gray W.G. (1975), "A Derivation of the Equations for Multi–Phase Transport," *Chem. Engng Sci.*, **30**, 229–233.

Gray W.G. (1983), "Brief Communication: Local Volume Averaging of Multiphase Systems Using a Non–constant Averaging Volume," *Int. J. Multiphase Flow*, **9**(6), 755–761.

Howes F.A. and Whitaker S. (1985), "The Spatial Averaging Theorem Revisited," *Chem. Engng. Sci.*, **40**, 1387–1392.

Hung C. I., Shyy W. and Ouyang H. (1995), "Transient Natural Convection and Conjugate Heat Transfer in a Crystal Growth Device," *Int. J. Heat Mass Transf*, **38**(4), 701–712.

Hupper H.E. (1990), "The Fluid Mechanics of Solidification," *J. Fluid Mechanics*, **212**, 209–240.

Koai K., Sonnenberg K. and Wenzl H. (1994), "Influence of Crucible Support and Radial Heating on the Interface Shape during Vertical Bridgman GaAs Growth," *J. Crystal Growth*, **137**, 59–63.

Kurz W. and Fisher D.J. (1989), *Fundamentals of Solidification*, Trans. Tech. SA, Switzerland.

Langer J.S. (1980), "Instabilities and Pattern Formation in Crystal Growth," *Review of Modern Phys.*, **52**, 1–28.

Lesieur M. (1993), "Advance and State of the Art on Large–Eddy Simulations," in *Refined Flow Modeling and Turbulence Measurements*, Proceeding of the 5th International Symposium, Paris, Sept. 7–10.

Levit V.I., Bul I.A., Hu J. and Kaufman M.J. (1996), "High Tensile Elongation of β–NiAl Single Crystals at 293 K," Submitted to *Scripta Metall. Mater.*, 1996.

Malvern L.E. (1969), *Introduction to the Mechanics of a Continuous Medium*, Prentice–Hall, Englewood Cliffs, New Jersey.

Moin P., Squires K., Cabot W., Lee S. (1991), "A Dynamic Subgrid–Scale Model for Compressible Turbulence and Scalar Transport," *Phys. Fluids*, **A3**(11).

Ni J. and Beckermann C. (1991), "A Volume–Averaged Two–Phase Model for Transport Phenomena during Solidification," *Metall. Trans. B*, **22B**, 349–361.

Nishimura T., Imoto T. and Miyashita H. (1994), "Occurrence and Development of Double–Diffusive Convection during Solidification of a Binary System," *Int. J. Heat Mass Transfer*, **37**(10), 1455–1464.

Noebe R.D., Bowman R.R. and Nathal M.V. (1993), "Physical and Mechanical Properties of the B2 Compound NiAl," *Int. Mat. Rev.*, **38**(4), 193–232.

Ocboa–Tapia J.A. and Whitaker S. (1995a), "Momentum Transfer at the Boundary Between a Porous Medium and a Homogeneous Fluid—I. Theoretical Development," *Int. J. Heat Mass Transfer*, **38**(14), 2635–2646.

Ochoa–Tapia J.A. and Whitaker S. (1995b), "Momentum Transfer at the Boundary Between a Porous Medium and a Homogeneous Fluid—II. Theoretical Development," *Int. J. Heat Mass Transfer*, **38**(14), 2647–2655.

Parfeniuk C., Weinberg F., Samarasekera I.V., Schvezov C. and Li L. (1992), "Measured Crystal Resolved Shear Stress and Calculated Temperature and Stress Fields during Growth of CdZnTe," *J. Crystal Growth*, **119**, 261–270.

Patankar S.V. (1980), *Numerical Heat Transfer and Fluid Flow*, Hemisphere, Washington, D.C.

Perry R.H., Green D.W. and Maloney J.O. (1984), *Perry's Chemical Engineerings' Handbook (6th edn)*, McGraw–Hill, New York.

Petrushevskii M.S., Levin E.S. and Gel'd P.V. (1971), "Viscosity and Interatomic Interaction Energy in Nickel–Aluminium Melts," *Russian J. Phy. Chem.*, **45**, 1719–1721.

Pfeiffer M. and Mühlberg M. (1992), "Interface Sbape Observation and Calculation in Crystal Growth of CdTe by the Vertical Bridgman Method," *J. Crystal Growth*, **118**, 269–276.

Poirier D.R. and Nandapurkar P. (1988), "Enthalpies of a Binary Alloy during Solidification," *Metall. Trans A*, **19A**, 3057–3061.

Poirier D.R., Nandapurkar P. and Ganesan S. (1991), "The Energy and Solute Conservation Equations for dendritic Solidification," *Metall. Trans B*, **22B**, 889–900.

Prakash C. and Voller V.R. (1989), "On the Numerical Solution of Continuum Mixture Model Equations describing Binary Solid–Liquid Phase Change," *Numer. Heat Transfer Part B*, **15**, 171–189.

Prescott P.J. and Incropera F.P. (1994), "Convective Transport Phenomena and Macrosegregation of a Binary Metal Alloy: I — Numerical predictions," *J. Heat Transfer*, **116**, 735–741.

Rappaz M. (1989), "Modeling of Microstructure Formation in Solidification Processes," *Int. Mater. Rev.*, **34**, 93–123.

Rudolph P. and Mühlberg M. (1993), "Basic Problems of Vertical Bridgman growth of CdTe," *Mat. Sci. Engng.*, **B16**, 8–16.

Sen S. and Stefanescu D.M. (1991), "Melting and Casting Processes for High–Temperature Intermetallics," *JOM*, **May**, 30–32.

Sen S., Konkel W.H., Tighe S.J., Bland L.G., Sharma S.R. and Taylor R.E. (1988), "Crystal Growth of Large–Area Single–Crystal CdTe and CdZnTe by the Computer–Controlled Vertical Modified–Bridgman Process," *J. Crystal Growth*, **86**, 111–117.

Schneider M.C. and Beckermann C. (1995), "Formation of Macrosegregation by Multicomponent Thermosolutal Convection during the Solidification of Steel," *Metall. Trans. A*, **26A**, 2373–2388.

Shyy W. (1994), *Computational Modeling for Fluid Flow and Interfacial Transport*, Elsevier, Amsterdam, The Netherlands.

Shyy W., Tong S.S. and Correa S.M. (1985), "Numerical Recirculating Flow Calculation using a Body–Fitted Coordinate System," *Numer. Heat Transf.*, **8**, 99 – 113.

Shyy W. and Chen M.–H. (1990), "Steady–State Natural Convection with Phase Change," *Int. J. Heat Mass Transf.*, **33**, 2545–2563.

Shyy W. and Burke J. (1994), "A Study of Iterative Characteristics of Convective–Diffusive and Conjugate Heat Transfer Problems," *Numer. Heat Transf.*, **26**B, 21–37.

Shyy W., Udaykumar H.S., Rao M.M. and Smith R.W. (1996a), *Computational Fluid Dynamics with Moving Boundaries*, Taylor and Francis, Washington, DC.

Shyy W., Liu J. and Ouyang H. (1996b), "Multi–Resolution Computations for Fluid Flow and Heat/Mass Transfer," Accepted for publication in *Advances in Numerical Heat Transfer.*

Siegel R. and Howell J.R. (1981), *Thermal Radiation Heat Transfer*, Hemisphere, Washington, D.C.

Slattery J.C. (1967), "Flow of Viscoelastic Fluids Through Porous Media," *A.I.Ch.E.*, **13**, 1066–1071.

Speich G.R. and Fisher R.M. (1966), "Recrystallization of a Rapidly Heated 31/4% Silicon Steel, Recrystallization," in *Grain Growth and Textures*, ASM, Metal Park OH, 563–598.

Takasugi T., Watanabe S. and Hanada S. (1992), "The Temperature and Orientation Dependence of Tensile Deformation and Fracture in NiAl Single Crystals," *Mat. Sci. Eng.*, **149**, 183–193.

Vedula K., Pathare V., Aslandis I. and Titran R. (1985), "Alloys Based on NiAl for High Temperature Applications," *Mat. Res. Soc. Symp. Proc.*, **39**, 411–421.

Viskanta R. (1990), "Mathematical Modeling of Transport Processes during Solidification of Binary Systems," *JSME Int. J.*, **33**(3), 409–423.

Voller V. (1985), "Implicit Finite–Difference Solutions of the Enthalpy Formulation of Stefan Problems," *IMA J.*, **5**, 201–214.

Voller V.R. and Prakash C. (1987), "A Fixed Grid Numerical Modelling Methodology for Convection–diffusion Mushy Region Phase–Change Problems," *Int. J. Heat. Mass. Transf.*, **30**(8), 1709–1719.

Voller V.R., Brent A.D. and Prakash C. (1989), "The Modelling of Heat, Mass and Solute Transport in Solidification Systems," *Int. J. Heat. Mass. Transf*, **32**(9), 1719–1731.

Voller V.R. and Peng S. (1994), "An Enthalpy Formulation Based on an Arbitrarily Deforming Mesh for Solution of the Stefan Problem," *Computational Mechanics*, **14**, 492–502.

Walston W.S. and Darolia R. (1995), "Effect of Alloying on Physical Properties of NiAl," *MRS Symp. Proc.*, **28**, 237–242.

Whitaker S. (1967), "Diffusion and Dispersion in Porous Media," *A.I.Ch.E.*, **13**, 420–427.

Zanio K. (1978), "Cadmium Telluride, in *Semiconductors and Semimetals*, **13**, Willardson, R. K and Beer, A. C. (eds.), Academic Press, New York.

BIOGRAPHICAL SKETCH

Hong Ouyang was born in the east corner of northern China, where it snows for half the year. Her curiosity in math and physics during her high school years drove her to step into the gate of Beijing University of Aeronautics and Astronautics (BUAA) in 1984 and dive into the field of Aerodynamics. During her senior year, her advisor handed her a thick FORTRAN program for the computation of flowfield around subsonic airfoils. From then, she started her endeavor in the so–called CFD area. She finished her B.S. as a distinguished graduate in 1988 and continued on to get her M.S. in Computational Mechanics in 1991. She came to the U.S. in August 1992. Since then she has been pursuing ber Ph.D. degree, specializing in the area of computational modeling and analysis of transport phenomena with an emphasis on materials solidification, in the Department of Aerospace Engineering, Mechanics and Engineering Science at the University of Florida,

I certify that I have read this study and that in my opinion it conforms to acceptable standards of scholarly presentation and is fully adequate, in scope and quality, as a dissertation for the degree of Doctor of Philosophy.

Wei Shyy, Chairperson
Professor of Aerospace Engineering, Mechanics and Engineering Science

I certify that I have read this study and that in my opinion it conforms to acceptable standards of scholarly presentation and is fully adequate, in scope and quality, as a dissertation for the degree of Doctor of Philosophy.

Ulrich H. Kurzweg
Professor of Aerospace Engineering, Mechanics and Engineering Science

I certify that I have read this study and that in my opinion it conforms to acceptable standards of scholarly presentation and is fully adequate, in scope and quality, as a dissertation for the degree of Doctor of Philosophy.

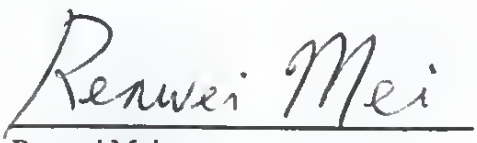

Renwei Mei
Associate Professor of Aerospace Engineering, Mechanics and Engineering Science

I certify that I have read this study and that in my opinion it conforms to acceptable standards of scholarly presentation and is fully adequate, in scope and quality, as a dissertation for the degree of Doctor of Philosophy.

John Abbitt
Assistant Professor of Aerospace Engineering, Mechanics and Engineering Science

I certify that I have read this study and that in my opinion it conforms to acceptable standards of scholarly presentation and is fully adequate, in scope and quality, as a dissertation for the degree of Doctor of Philosophy.

Michael Kaufman
Professor of Materials Science and Engineering

This dissertation was submitted to the Graduate Faculty of the College of Engineering and to the Graduate School and was accepted as partial fulfillment of the requirements for the degree of Doctor of Philosophy.

May 1996

for Winfred M. Phillips
Dean, College of Engineering

Karen A. Holbrook
Dean, Graduate School

LD
1780
1996
.095

UNIVERSITY OF FLORIDA
3 1262 08554 9193